Impedance Spectroscopy of Diamond Films

Haitao Ye

This thesis submitted for the degree of Doctor of Philosophy

Department of Electronic and Electrical Engineering

University College London

University of London

2004

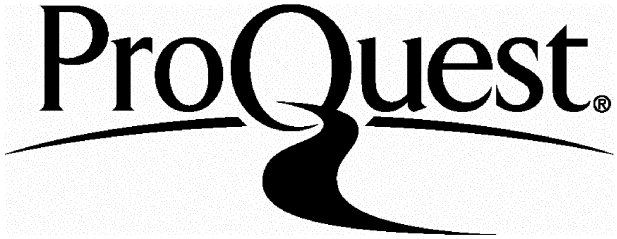

The greatest real thrill that life offers is to create, to construct, to develop something useful. Too often we fail to recognize and pay tribute to the creative spirit. It is that spirit that creates our jobs. There has to be this pioneer, the individual who has the courage, the ambition to overcome the obstacles that always develop when one tries to do something worthwhile, especially when it is new and different.

— Alfred P. Sloan, Jr., 1941

==========

Acknowledgement

I would like to acknowledge the department of Electronic and Electrical Engineering (5A ranking in this subject in the UK) of UCL for the award of an EPSRC departmental research studentship and the CVCP Committee for the award of an Overseas Research Student (ORS) scholarship. I am also indebted to the KC Wong Education Foundation and King's College London, for a kindly financial support. Without these awards, it would not be possible for me to pursue this degree.

Institute of Physics (IOP), Institute of Materials, Minerals and Mining (IOM^3), Society of Chemical Industry (SCI), EPSRC Diamond Research Network and UCL Graduate School are also thanked for providing me numerous travel awards to attend international conferences overseas.

I would like to express my deepest gratitude to my research supervisor, Dr Richard B. Jackman for his invaluable guidance, support and encouragement throughout the project. The UCL diamond group, according to seniority, Dr Olivier Gaudin, Dr Stuart Lansley, Dr Oliver Williams, Mr Damianos Troupis, and the newly joined Stephane Curat are appreciated for valuable discussion during this PhD. I would also like to thank the clean room staff, Vic Law and Kelvin Lee for their advice on the installation of AsTeX kits, device fabrication, and numerous clean room processing. Professor Jeffery Harris is thanked for valuable discussions on physical mechanisms for ultrananocrystalline diamond films (UNCD).

Professor Alan Atkinson and Dr Rob Rudkin from Materials Department at Imperial College London are thanked for accessing their brilliant impedance kit. Dr Neal Skipper from Physics Department, Dr Steve Firth from Chemistry Department and Dr Kelvin Reeves from Institute of Archaeology at UCL are thanked for accessing their XRD, Raman and SEM facilities and useful

discussions on the results. Dr Dieter M. Gruen from Argonne National Laboratory (USA) and Dr Etienne Gheeraert from Grenoble (France) are thanked for providing UNCD films and boron-doped single crystalline diamond films, respectively. Dr Haixue Yan from Queen Mary University of London is thanked for numerous discussions on the dielectric relaxation of materials.

Professor Peter Hing in NTU (Singapore) is appreciated for helping me to settle down when I just came to London in 2000. Mr Adrian Li Mow Ching, the very first friend I met in London is thanked for numerous exercises on table tennis, badminton and swimming. The flatmates, Dr Hu Zhang and Mr Xiuyan Sun are thanked for their support, help and warm company during my first and second year, respectively. Mr Gianluca Di Federico and Mr Massiminias Nori, in Manor House are thanked for numerous house parties and delicious Italian pasta, which make life lovely, beautiful and exciting when we were flatmates in the third and fourth year. The Kims, a Korean family, is also thanked for hosting several Christmas parties and gatherings on the nice Bournemouth beach.

Managing Chinese Students and Scholars Society is really a part of my PhD. Being the Chairman of Chinese Students and Scholars Association at both University College London and University of London Union for two years, I have been encouraged by the officials from the Education Section of Chinese Embassy in London, Mr Wang Yongda, and Mr Zhang Shaohua, and Mr Yang Zhongbo, Ms Guo XiaoJuan, and Ms Angela Jeffs from University of London Union for their dedication to support and help all of the Chinese students whenever needed. I am also indebted to Ministry of Education of China for a National Award for Excellent Chinese Students Overseas in 2003.

UCL PPMS staff, Dr Paul Walker, Ms Margot Lindsay, and Ms Valerie Crees, are acknowledged for providing the exciting experience in Hillingdon Outdoors Activity Centre. It is somehow the first time for me to sleep in the tent, and paddle on the risky raft. I could not pass the accredited ECDL test smoothly without the help and instruction from Miss Michelle Sinclair, IT training officer in UCL.

And in China, special gratitude is due to my parents, sister, and others for their consistent and endless encouragement and support throughout this PhD.

Ye Haitao
April 2004
London

Abstract

Research in the area of CVD diamond thin films has increased significantly during the last decades. The remarkable properties of diamond including its extreme hardness, low coefficient of friction, chemical inertness, high thermal conductivity, transparency and semiconducting properties make it attractive for a number of applications, among which electronic devices is one of the key areas. A detailed knowledge of electrical properties of diamond films is therefore critical.

This thesis describes spectroscopic impedance studies of CVD diamond films. Impedance spectroscopy is a powerful technique for investigating the electrical properties of polycrystalline materials, being capable of isolating conduction processes within the grain, grain boundary and electrode regions. Thus it can be used for researching methods for reducing problems within diamond technology that are associated with grain boundaries and poor metallic contacts.

Systematic investigations have been carried out on single crystalline, microcrystalline and nanocrystalline diamond films. The influence of film quality variations, such as those found when hot filament CVD grown diamond films are compared to microwave plasma enhanced CVD grown diamond has also been studied. Grain size effects on the dielectric properties of diamond films are discussed in detail. Impedance values and associated equivalent capacitance values enable the conduction paths within the material to be attributed to either grain interiors or grain boundaries. Combined with insight gained from scanning electron microscope images, x-ray diffraction patterns and Raman spectroscopy, a full analysis of all the impedance measurements made are summarized in this thesis. Also reported is the first demonstration of impedance measurements on ultrananocrystalline diamond films. Possible physical mechanisms responsible to the observed phenomena are presented.

Table of Contents

Relevant Publication

1. Ye HT, Jackman RB and Hing P, Spectroscopic impedance studies on nanocrystalline diamond films, *Journal of Applied Physics* **94** (2003) 7878-7882.

2. Ye HT, Gaudin O, Jackman RB, Muret P and Gheeraert E, Impedance spectroscopy on Boron doped single crystalline diamond films, *physica status solidi (a)* **199** (2003) 92-96.

3. Lansley SP, Gaudin O, Ye HT, McKeag RD, Whitfield MD, Rizvi N and Jackman RB, Imaging deep UV light with diamond-based systems, *Diamond and Related Materials* **11** (2002) 433-436.

4. Ye HT, Williams OA, Jackman RB, Rudkin R and Atkinson A, Electrical conduction of CVD diamond films: temperature dependent impedance measurement, *physica status solidi (a)* **193** (2002) 462-469.

5. Lansley SP, Williams OA, Ye HT, McKeag RD, Whitfield MD, Rizvi N and Jackman RB, 1-D imaging arrays of CVD diamond films, *physica status solidi (a)* **193** (2002) 476-481.

6. Ye HT, Williams OA and Jackman RB, Measurement of Activation Energy for Black Diamond using Impedance Spectroscopy, *International Journal of Modern Physics B* **16** (2002) 4487-4492.

7. Ye HT, Sun C and Hing P, Single semicircular response of dielectric properties of diamond films, *Thin Solid Films* **381** (2001) 52-56.

8. Ye HT, Sun C, Huang H and Hing P, Dielectric transition of nanostructured diamond films, *Applied Physics Letters* **78** (2001) 1826-1828.

Chapter 1 Introduction

The semiconducting properties of natural diamond were discovered as early as the 1950's [Brophy 1955]. Diamonds optical properties and its hardness led it to be prized as a gemstone far before this. Even today, there is still a strong demand for optically flawless diamond for the same reasons. Research in the area of diamond thin film deposition has increased significantly in the last decades. The remarkable properties of diamond, including its extreme hardness, low coefficient of friction, chemical inertness, high thermal conductivity, transparency and semiconducting properties make it attractive for a number of applications. The main objective of this study is to utilize electrochemical impedance spectroscopy (EIS) to investigate the electrical conduction paths within diamond films, since this information is vital if thin film diamond is to be used in electronic applications.

Chapter 2 reviews the field of diamond technology, reporting on structure, growth, properties and applications. An account of the chemical vapour deposition methods of growing diamond is also presented in this chapter. Substrate materials, surface pre-treatments, nucleation enhancement, and deposition conditions are reviewed.

Spectroscopic impedance studies on diamond films form the basis of this thesis; as such the current status, models, and fundamental applications and interpretations related to this technique are crucial to this work. Chapter 3 provides detailed background information based on both theoretical and empirical knowledge in this area. Starting with general concepts of electrochemical impedance, the principle of this technique is presented, followed by the connectivity models. The use of this technique to characterize the grains and grain boundaries contribution are discussed in details. Then the equivalent electrical circuits and formulae for corresponding capacitance are presented in order to compare with real materials system. Finally, from the

microscopic point of view, different mechanisms on dielectric relaxation and polarization are summarized.

Chapter 4 describes the main experimental and characterization techniques employed during the course of the research work reported in this thesis. The principles behind each technique are introduced along with brief background information.

The experimental results commence in chapter 5 with an impedance spectroscopic investigation of boron-doped single crystalline diamond. The activation energy calculated from experimental data is 0.37eV, which is consistent with the theoretical value published of this kind of material. The experimental results build up a better understanding of the boron-doped diamond and positively indicate that impedance spectroscopy is a feasible and useful tool in electrical and dielectric properties for diamond films.

Among the multitude of diamond CVD processes which have been developed for about 20 years, the microwave plasma enhanced CVD process (MPECVD) together with the hot-filament CVD method (HFCVD) has continued to be one of the most used diamond deposition processes. Chapter 6, therefore, compares the impedance properties of diamond films deposited using both MPECVD and HFCVD methods.

A polycrystalline diamond film has a high potential to serve as a dielectric layer and heat spreader to a copper heat sink. This requires enhancing of the thermal performance and lowering of the static dielectric constant in addition to the thermal stability and adequate adhesion between diamond film and substrate. Note that the smaller the grain size, the smoother the surface morphology and the better the adhesion to the substrate for thin film materials. In addition, although diamond films have a good resistance to corrosion from liquids such as boiling KOH, these can permeate the films and attack the underlying material. In order to prevent this, the individual

diamond grain size should be less than 30 nm. Understanding the size effect on the electrical properties, therefore becomes necessary for tailoring this interesting material for a variety of applications. Chapter 7 reports on the grain size effect on the dielectric constant of MPECVD diamond films, and correlates the results to x-ray diffraction (XRD), Raman spectroscopy and scanning electron microscopy (SEM).

Nanocrystalline (NCD) and ultrananocrystalline (UNCD) diamond films have been recognized as presently useful for many applications in fields as diverse as electrochemical electrodes, tribology, cold cathodes, corrosion resistance, and conformal coatings. Chapters 8 and 9 present the spectroscopic impedance studies on NCD and UNCD films, respectively. These two chapters present further evidence for both grain boundaries and grain interior conduction paths. It provides the insights into the electrical conduction mechanisms within NCD and UNCD films, and their relationship with possible physical mechanisms.

Chapter 10 summaries the thesis and present conclusions based on the work achieved at UCL, and also points out the future work. The impact of these results on the potential use of these materials within electronic and dielectric device applications is discussed.

References

Brophy J, J. Phys Rev. **99** (1955) 1336.

Chapter 2

Structure, Growth, Properties and Applications

2.1 Introduction

The remarkable properties of diamond, including its extreme hardness, low coefficient of friction, chemical inertness, high thermal conductivity, transparency and semiconducting properties make it attractive in both academia and industry, as described as the best available material for many potential applications. In a view of a material scientist, the structure, process, properties, and applications of any existing substance are closely correlated and can be tuned accordingly. This chapter will present a general review on the above-mentioned four fundamental factors in diamond research community.

2.2 Crystal Structure

Diamond has a face-centered cube lattice with eight atoms per unit cell. For diamond, the measured cubic edge length is 3.567 Å at 0°C. With its four-fold symmetric tetrahedral (sp^3) bonds, the diamond structure is isotropic and more compact than that of graphite as shown in figure 2.1. However, the graphite has an sp^2 anisotropic structure and a wide interlayer spacing. The crystal structure of graphite consists of layers in which the carbon atoms are arranged in an open network. Consequently diamond has higher density than graphite (3.515 g/cm^3 vs. 2.26 g/cm^3, respectively) [Dresselhaus and Kalish 1992]. Diamond appears in several crystal forms with symmetric space structures, which include the tetrahedron, cube, octahedron, dodecahedron, and others which are more complicated combinations to each other. There are three major orientations of diamond: the (100) cubic, the (110) dodecahedral and the (111) octahedral plane. Both cubic and octahedral surfaces are predominant alone or in combination to form crystals under high pressure. In CVD diamond, the (111) octahedral and the (100) cubic surfaces predominate and cubo-octahedral crystals combining both of these surfaces are commonly found. Twinning occurs frequently on the (111) surface.

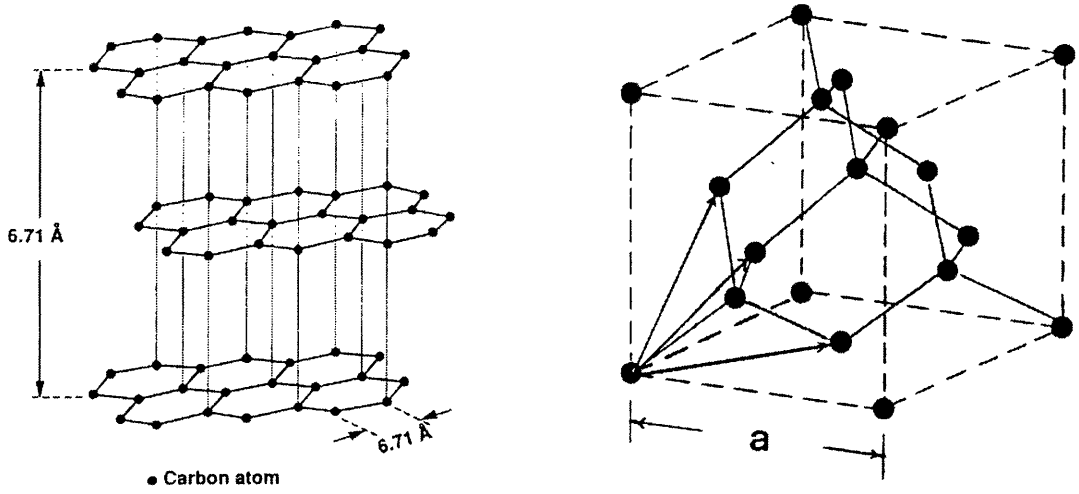

Figure 2.1 Two main structural types of crystalline carbon: graphite (left) and diamond (right) (Dresselhaus and Kalish 1992)

2.3 Classification of Diamond

Diamonds have been historically classified into four categories according to their optical absorption properties, which are determined by impurities of nitrogen, boron and hydrogen related defects as listed in table 2.1.

Type I comprises the diamond, in which nitrogen defects dominate optical and paramagnetic absorption. **Type Ia** diamonds exhibit strong absorption in the infrared, which is dominated by non-paramagnetic aggregates of nitrogen. Most of the natural diamonds belong to this group. **Type Ib** diamonds contains paramagnetic active nitrogen as substitutional impurities. While the type Ib diamonds are rarely formed in nature, most synthetic diamonds belong to this group.

Type II comprises the diamonds showing no optical and paramagnetic absorption due to the nitrogen related defects. Diamonds with the highest purity are **type IIa**, which do not show optical absorption due to boron and hydrogen impurities, either. Therefore **type IIa** diamonds exhibit the intrinsic

semiconducting properties with a wide band gap of 5.47 eV. **Type IIb** diamonds are naturally boron doped, and show p-type conductivity due to an acceptor level introduced by the substitutional boron located at 0.35~0.38 eV above the valence band.

Type	Ia	Ib	IIa	IIb
Abundance (%)	98	1-2	very rare	Extremely rare
Nitrogen Content (%)	Up to 0.1 (platelets) or up to 5000 ppm	Up to 0.2 (paramagnetic) or synthetic up to 500 ppm	<5ppm or practically zero	Essentially zero
Nitrogen Content (cm^{-3})	10^{19}-10^{21}	-	10^{18}	-
Optical Transparency (nm)	>320	>320	>225	Bluish to blue (boron)
Thermal Conductivity (W/cm K)	9	9	26-32	26
Electrical Resistivity (Ω cm)	$>10^{16}$	$>10^{16}$	$>10^{16}$	10-1000 (p-type) or up to 10 ppm boron
Dislocation Content	Low High mobility	-	High, $>10^{5}$ low mobility	-
Hardness	Possibly not as hard as IIa	-	Possibly harder than Ia	-

Table 2.1 Classification of single crystal natural diamond [Kiflawi and Lawson 2001]

2.4 Growth Techniques

During the past decades, a large number of new methods were developed to deposit diamond films. In general, diamond thin films can be formed using CVD reaction arising from two basic activation methods shown in table 2.2.

(1) Activation by high temperatures (TACVD = Thermally Activated Chemical Vapor Deposition), including hot-filament/hot surfaces, laser heating, arc discharge and arc plasma jet as well as chemically induced hot gas flames.

(2) Activation by electric or electromagnetic gas discharge (PACVD = Plasma Activated Chemical Vapor Deposition), including microwave and radio-frequency gas discharge, DC and AC glow discharges, as well as plasma jet induced by RF, microwave, DC, etc.

(3) Combination of the above methods, for example, hot-filament + microwave, hot-filament + DC discharge and hot filament + Bias electric potential, etc. has also been developed [Patterson et al 1991].

Microwave plasma for diamond deposition was first reported in 1983. This technique along with the "hot-filament' method brought diamond thin films much closer to an industrially applicable technology. Magnetized and electron cyclotron resonance (ECR) microwave plasmas were also used for diamond growth [Yuasa et al 1991].

The present status of diamond CVD is summarized in table 2.2. It illustrates that a variety of different methods are capable of depositing high quality coatings on to various non-diamond substrates. Some of these methods like microwave plasma CVD or DC jet CVD are already well established. However, which method to choose will depend primarily on the specific application. If a contamination-free, uniform coating on medium size substrate is required at

fairly low equipment costs, then the microwave plasma CVD is probably a good choice. Such units also have the advantage of stability over extended periods of usage and the deposition process can be automated. For bulk material, DC arc discharge or jets seems to be most promising. The state-of-art of other methods is presently not viable enough within an industrial environment.

Methods	Details	Year of publication
Thermal CVD	Thermal decomposition	1956, 1962
	Chemical transport reaction	1981,1991
	Hot filament technique	1982, 1985
	Oxy-acetylene torch	1988,1991
	Halogen assisted CVD	1956,1991
DC plasma CVD	Low pressure DC plasma	1987,1989
	Medium pressure DC plasma	1987,1990
	Hollow cathode discharge	1988
	DC arc plasmas and plasma jets	1989,1988
RF plasma CVD	Low pressure RF glow discharge	1985,1989
	Thermal RF plasma CVD	1987,1991
Microwave plasma CVD	915 MHz plasma	1988
	2.45 GHz low pressure plasma	1983,1986
	2.45 GHz thermal plasma	1989
	2.45 GHz magnetized plasma	1987,1989
	8.2 GHz plasma	1989
Other methods	C implantation + laser treatment	1991,1992
	Laser conversion of carbon	1989

Table 2.2 Methods for synthesizing diamond at low pressures and low temperatures [Liu and Dandy 1995]

2.5 Nucleation Mechanism

It is increasingly evident that further technological developments in CVD of diamond films require a detailed understanding and an effective control of the fundamental phenomena associated with diamond nucleation and growth. This is particularly true in challenging areas such as precision engineering where ultrathin single crystal growth is needed. An example of this is low temperature deposition coating on optical and plastic materials for microelectronics and data storage. These phenomena, especially the nucleation process, critically determine the film properties, morphology, homogeneity and defect formation.

Diamond nucleation seems to be hampered only if the carbon is too rapidly removed by diffusion or chemical reaction with a particular substrate. The carbon atoms arriving from the gas phase at the substrate surface must exceed a certain minimum concentration at the solid/gas interface in order to reach and exceed the critical nucleus size. Nucleation is randomly distributed. Their number per unit surface area depends on the balance between the flux of incoming carbon atoms arriving at the substrate surface and the carbon diffusion rate into the substrate. The carbon bulk diffusion into the substrate controls when the necessary minimum carbon concentration for nucleation can be reached. The carbon surface diffusion determines the distance between a nucleus and its immediate neighbors [Ascarelli and Fontana 1993].

In the diamond CVD process, gaseous reactants, typically methane in hydrogen, flow into the reactor and the hot filament or plasma initiates gaseous reactions. The reactants, products, and reactive species are transported in the reactor by diffusion and convection. On the surface, adsorption, diffusion, and reaction of various species occur leading to the nucleation of diamond particles (or sp^3), suppression of graphite (or sp^2) carbon, and ultimately the growth of a

continuous diamond film. This is a complex process with many variations, and in which many specific mechanisms are involved.

2.5.1 Gas-phase Nucleation

Homogeneous nucleation in the gas phase and its contribution to different deposition processes are poorly understood. However, there is evidence that, at least in some cases, diamond can be nucleated homogeneously in the gas phase. Matsumoto and Matsui [1983] suggested that hydrocarbon cage molecules such as adamantine, bicyclooctane, texacyclopentadecane and dodecahedron are possible embryos for homogeneous nucleation of diamond. However, thermodynamic equilibrium calculations revealed that such low-molecular-weight hydrocarbons were not stable at high temperatures (over 600°C) in the harsh environment associated with diamond CVD [Seino and Nagai 1993].

A limited number of experiments have been conducted to examine homogeneous nucleation of diamond in the gas phase at atmospheric and sub-atmospheric pressures [Singh and Vellaikal 1993]. The number of diamond particles collected from the gas phase is very small compared with typical nucleation densities observed on different substrate surfaces. Therefore, the homogeneous nucleation mechanism cannot account for the large variation of nucleation densities observed on different substrate materials. The nuclei formed in the gas phase may reach the growing surface and increase the surface nucleation density. However, whether and how the diamond particles formed in the gas phase could serve as seeds on the substrate surface for subsequent growth of diamond film is still not clear.

2.5.2 *Surface Nucleation*

It is reported that diamond has the highest surface energies among any known materials. A conventional growth process in the CVD of polycrystalline diamond films typically shows several distinguishable stages [Liu and Dandy 1995]: (a) incubation period; (b) 3-D surface nucleation; (c) termination of nucleation and 3-D growth of nuclei to grains; (d) faceting and coalescence of individual grains and formation of continuous film; and (e) growth of continuous film. Two criteria must be satisfied for 'spontaneous' (non-epitaxial) surface nucleation: (a) carbon saturation of the substrate surface and (b) the presence of high-energy sites (unsaturated valences).

Diamond nucleation on non-diamond substrates is generally supposed to occur mostly on an intermediate layer of diamond-like amorphous carbon, metal carbides or graphite formed at the substrate surface owing to chemical interactions between the activated gaseous species and the surface during the incubation period [Liu and Dandy 1995]. Furthermore, such intermediate layers provide nucleation sites for diamond crystallite growth. And they enhance diamond nucleation density on non-diamond substrates and offer an opportunity for controlling the morphology, orientation and texture of diamond films. The thickness of inter-layers ranges from several angstroms, to nanometers, up to even a few micrometers. The representative nucleation mechanisms proposed in published literature are summarized in figure 2.2 [Liu and Dandy 1995].

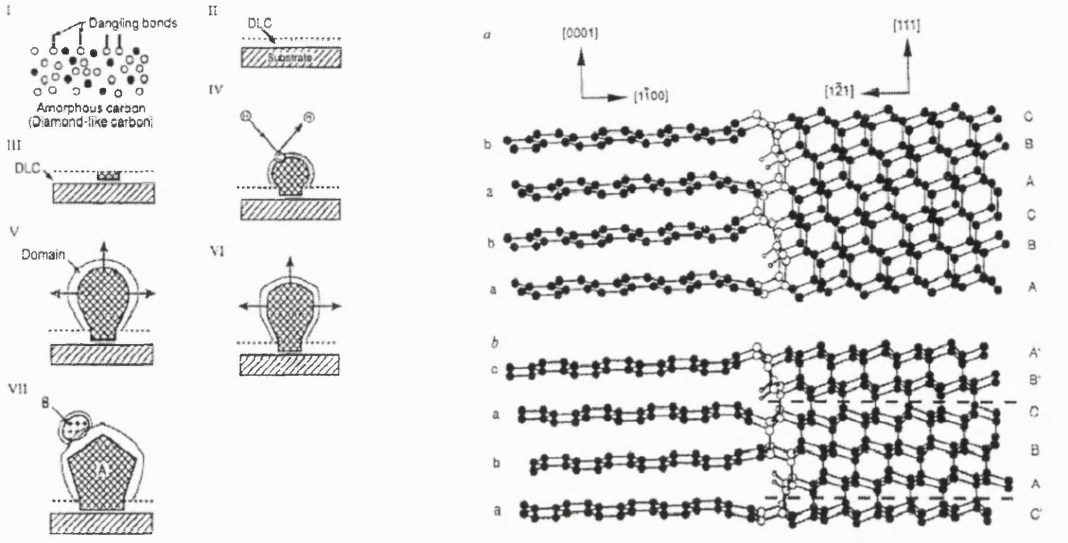

(a) (b)

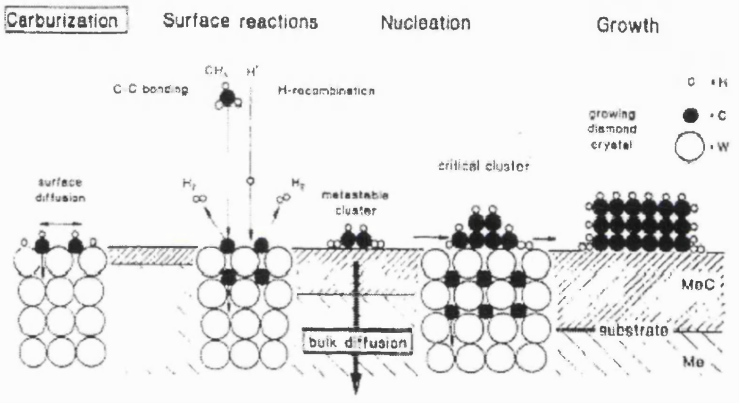

(c)

Figure 2.2 Summary of nucleation mechanisms thought to account for nucleation of diamond on most substrate: (a) On a DLC interlayer: (I) formation of carbide clusters, bonding change from sp^1 to sp^2; (II) sp^2 converts to sp^3, (III) amorphouse phase crystallises; (IV-VI) growth and faceting of diamond crystals; (VII) secondary nucleation and growth. (b) On a graphite interlayer: Condensation of graphite followed by hydrogenation of the {1 $\bar{1}$ 00} prism planes along edges of graphite particles; diamond nucleation at emerging stacking fault - almost perfect interface. Upper: cubic diamond on perfect hexagonal graphite, lower: twinned diamond nucleus adjoining a graphite stacking fault. Twin boundaries: dash lines, H-atoms: small open circles, C-atoms: solid circles. (c) On a carbide interlayer: Carburisation consumes available C to form carbide surface; C surface concentration below diamond nucleation minimum; carbide layer thickness increases; C transport rate decreases, C surface concentration increases; diamond nucleus forms when either surface C concentration reaches critical level or C cluster attains critical size [Liu and Dandy 1995].

Singh [1994] provided direct evidence for the formation of a diamond-like amorphous carbon layer, in which small nanocrystalline diamonds were embedded on copper TEM grids, and large diamond crystallites were observed to grow from these nanocrystallites. It was suggested that the diamond nanocrystallites be formed as a result of direct transformation of the a-C into diamond, with the intermediate layer providing nucleation sites. Figure 2.2 (a) depicts the detailed nucleation mechanism proposed on the basis of the experimental observations.

In step I, carbon clusters are formed on the substrate surface, and a change in the bonding structure from sp^1 to sp^2 takes place. In step II, sp^2-bonded carbon atoms are converted into a relatively stable network of sp^3-bonded carbon. At the same time, etching of unstable phases (sp^1 and sp^2), which is ten times faster than etching of stable phase (sp^3), promotes and stabilizes the sp^3 phase. In step III, a bonding state in the carbon network transits from a disordered domain to diamond. Carbon atoms added into the surface (step IV) diffuse inwards by a solid-state diffusion process. Once a diamond microcrystal reaches a critical size (step V), it will acquire a faceted crystallographic shape characterized by defects (VI). In step VII, secondary nucleation takes place.

Several experiments on Ni, Pt in HFCVD [Belton and Schmieg 1992], on Si [Waite and Shah 1992], and Cu [Ong et al 1992] in MPECVD have provide direct evidence for the formation of graphite on the substrates prior to diamond nucleation. On the basis of these experimental results, Lambracht et al [1993] proposed a detailed nucleation mechanism, as shown schematically in figure 2.2(b). It was suggested that graphite initially condenses on the substrate surface and the $\{1\,\bar{1}\,00\}$ prism planes are subsequently hydrogenated. Diamond nuclei grow preferentially on the prism planes of graphite , with kinetically preferential nucleation at the emerging graphite stacking faults, and with an almost perfect interface between graphite and the diamond nuclei. Etching of graphite occurs simultaneously during diamond nucleation. Atomic hydrogen

terminates the dangling surface bonds and stabilizes sp^3 nuclei with repect to sp^2 nuclei. Lambracht et al [1993] stated this detailed nucleation mechanism is the dominant channel for the spontaneous nucleation of new independent diamond crystals in the absence of pre-existing diamond seeds.

Badzian [1988] suggested that diamond nucleation on Si proceeds by the formation of a β-SiC buffer layer, followed by nucleation on the surface of the silicon carbide. This is supported by many growth experiments performed either on diamond particles/films on Si substrate in HFCVD and MPCVD [Wolter et al 1993], which showed that the Si surface was indeed transformed to SiC leading to diamond growth with diamond nucleation occurring on a SiC intermediate layer.

A recent AFM study [George et al 1994] provided further evidence for the formation of SiC. The formation of a Mo carbide layer in the initial stage of diamond film deposition was reported in d.c. arc discharge CVD [Smolin et al 1993] and MPCVD [Meilunas et al 1989]. The growth rate of SiC was much lower than that of Mo_2C. Diamond nanocrystallites were observed after 1 min, and no further carbide layer growth was detected once the interface was covered with diamond. Wolter et al [1995] conducted systematic studies of diamond growth on carbide-forming refractory metals, and observed that diamond nucleation occurred only after the formation of a thin carbide layer. Lux and Haubner [1991] subsequently proposed a model to elucidate the mechanism governing the nucleation process on a carbide-forming substrate as shown in figure 2.2 (c). It was suggested that carbon dissolved into the substrate initially, resulting in the formation of a stable carbide. Diamond nucleation is believed to occur on the carbide layer when the carbon concentration on the surface reaches its saturation value.

Lux and Haubner [1991] also compared the time evolution of diamond nucleation densities on Ti, Hf, Nb, Ta, Mo and W, and found that the difference in the nucleation densities was related to the diffusion of carbon in the

respective substrates. The incubation period for nucleation is the shortest on metal that can most rapidly achieve a super-saturation of carbon on the surfaces.

2.6 Growth of Diamond

The growth of the nuclei first leads to the formation of individual, rapidly growing crystals [Angus et al 1991, Belton and Schmieg 1990]. The nuclei form either single or polycrystals exhibit re-entrant corners, growth spirals and growth steps for easy atomic attachment in order to avoid the need of surface nucleation. Once a population of such individual crystals has started to grow and the optimal nucleation density in accordance with the surface diffusion rate has established the minimum distances between the next neighbors, no further individual nuclei are formed. It has been shown that during the early growth stages small crystals can be dissolved again if the bulk diffusion rate of carbon into the substrate is high enough [Liu and Dandy 1995]. The density of the nuclei is never so high that a layer can form directly. The individual crystals grow in all directions until they touch and form the layer. The growth rates of individual crystal diameters are of course much higher than the increase in layer thickness. The total weight gain per unit surface and time becomes, however, higher once the layer is formed [Wild et al 1993]. The most important deposition parameters responsible for the quality of the diamond films are discussed below.

2.6.1 *Substrate Materials*

Substrate materials may be classified into three major groups in terms of carbon/substrate interactions, as listed in table 2.3. Diamond surfaces or particles provide the best nucleation potential [Komori et al 1993]. Nucleation on cubic BN readily occurs. Nucleation rates on stable carbide-forming substrates (Si, Mo and W) are one to two orders of magnitude higher than on non-carbide-forming substrates (Cu and Au). Among carbide-forming substrates (Si, Mo, Al, Ni and Ti), the nucleation density on Mo is about one order of magnitude higher than on all other substrates under the same deposition conditions [Akatsuka et al 1991]. Nucleation rates are several times higher on polycrystalline substrates than on single crystal substrates of the same material after identical surface pretreatment. Refractory metal carbides (TaC, WC and Mo_2C) and some covalent carbides (SiC and B_4C) have a positive effect on nucleation, while the effect of ionic carbides (Al_4C_3 and liquid salts) on nucleation needs yet to be known. Nucleation occurs readily on substrates forming amorphous diamond-like carbon (mostly Mo and Si) without any scratch pretreatment.

Table 2.3 Classification of substrate materials [Fabisiak et al 1993]

Little or no solubility or reaction	Diamond, graphite, carbons, Cu, Ag, Au, Sn, Pb, etc.
C-diffusion	Pt, Pd, Rh, etc.
Carbide formation	
Metallic	Ti, Zr, Hf, V, Nb, Ta, Cr, Mo, W, Fe, Co
Covalent	B, Si, etc.
Ionic	Al, Y, rare earth metals, etc.

2.6.2 *Effect of Hydrogen, Nitrogen, Oxygen and Noble Gas.*

The reaction gas used in low-pressure diamond synthesis methods contains relatively low concentrations of volatile carbon compounds with a high excess of hydrogen. Activation of such a gas mixture is carried out to obtain the highest possible concentration of atomic hydrogen. Atomic hydrogen plays a major role in mediating rates and in maintaining a proper surface for growth. Low molecular weight hydrocarbon species (e.g., CH_3 and C_2H_x) are believed to be responsible for the extension of diamond lattice. A complete understanding of the attachment mechanism, however, has not yet been achieved. A number of hydrogen-carbon compounds have already been used successfully as carbon source. The atomic attachment kinetics at the diamond/gas interface is not fully understood. Several hypothetical models have been proposed [Yugo et al 1991].

The essential features of the synthesis, as characterized by the following two reactions, proceed simultaneously: (1) The decomposition reaction. It consists of a normal pyrolitic hydrocarbon chemical vapor deposition reaction; (2) The etching reaction by the atomic hydrogen. This prevents the formation of all other weakly bonded solid carbon compounds except diamond.

The presence of a small amount of nitrogen in the CH_4/H_2 gas mixture is not harmful. But the presence of both nitrogen and oxygen seems to be detrimental. In this case, due to the gas activation, NO_x compounds can react with the atomic hydrogen and reduce its concentration. Nitrogen as impurity leads to a complete change in the texture and surface morphology [Locher et al 1993]. However, oxygen additions to the gas mixture without nitrogen are probably not harmful at all and can even have positive effects [Chen 1988]. The addition of small amounts of oxygen leads to the formation of transparent diamond crystals due to the reduction of crystal defects [Yugo et al 1991].

Argon or other heavier noble gases can effectively increase the electron density of the plasma that promotes the equilibrium of hydrogen atoms and ions and improves the properties of the deposited films [Shih et al 1992]. Similar to nitrogen and oxygen, these noble gases have significant effects on surface morphology and crystalline structure of diamond films. By adjusting the noble gas/hydrogen ratio in the gas mixture, a continuous transition from micro- to nanocrystallinity is achieved [Gruen 1999].

2.6.3 Surface Pretreatment and Nucleation Enhancement

Diamond nucleation on non-diamond surfaces can be enhanced by surface pretreatments. Surface pretreatment methods include scratching, seeding, electrical biasing, covering/coating, ion implantation, pulse-laser irradiation and carburization. Ultrasonic scratching and biasing have the best efficiency on nucleation enhancement. This is followed by scratching, seeding, covering/coating, and ion implantation. Nucleation on pretreated surfaces is observed to occur primarily on carbide-rich particles or defects such as scratches, grain boundaries, particle boundaries, dislocations, electron bombardment damages, and edges of etch pits/craters [Stoner et al 1992].

Nucleation enhancement by scratching is attributed to: (a) seeding effects [Ihara et al 1994], (b) minimization of interfacial energy on sharp convex surfaces [Dennig and Stevenson 1991], (c) breaking of a number of surface bonds, or the presence of a number of dangling bonds at sharp edges [Kobayashi et al 1992], (d) strain field effects [Lin et al 1992], (e) rapid carbon saturation (fast carbide formation) at sharp edges [Angus et al 1991], and (f) removal of surface oxides [Ascarelli and Fontana 1993]. Another possible operating mechanism for nucleation enhancement by scratching is that it produces non-volatile graphitic particles through local pyrolysis of absorbed hydrocarbons [Lambrecht et al 1993]. These graphitic clusters would be

subsequently hydrogenated in the atomic-hydrogen environment under the typical CVD conditions to form the precursor molecules.

The efficiency of scratching on different substrates decreases from Si to Mo to WC substrates [Yarbrough and Messier 1990]. Abrasive used for scratching pre-treatment includes diamond, oxides, silicides, nitrides, carbides and borides. The effect of abrasives on nucleation enhancement increases in the following order: silicides < SiO_2 < nitride < ZrO_2 < carbides < borides < Al_2O_3 < cBN < diamond [Liu and Dandy 1995]. Nucleation density decreases with increasing particle size of diamond abrasive paste in the polishing pretreatment. Generally, however, the optimum size of abrasive particles depends on pretreatment methods, deposition processes, growth conditions, and the nature of substrate materials.

Dipping, spinning, spraying and electrophoretic seeding have been employed to seed diamond, Si, Al_2O_3, or SiC on various substrates [Valdes et al 1991]. The residual diamond seed particles on the substrate surface are the predominant nucleation sites (or the seed particles themselves are nuclei), and diamond growth then occurs by means of homoepitaxy on these seed particles. Nucleation density is linearly proportional to the diamond seed particle density. It is approximately one-tenth of seed particle density [Ihara et al 1994].

Biasing a substrate can help to reduce and suppress oxide formation on the substrate surface, remove native oxides and overcome the energy barrier for the formation of stable diamond nuclei by more effectively activating the substrate surface and/or increasing the flux and mobility of atoms [Stoner et al 1992]. In d.c. MPCVD and HFCVD, positive substrate biasing is effectively employed to increase nucleation of diamond, while in MPCVD both positive and negative biasing can enhance diamond nucleation.

Nucleation enhancement has also been achieved by covering the substrate surface with graphite fibers/clusters or films, and coating substrate surface with thin films of metals (Fe, Ti, Mo, Ni), DLC, BN, SiC etc [Yehoda et al

1992]. The efficiency of the overlaid materials on nucleation enhancement decreases in the orders of C70, a-C, DLC, graphite fiber, graphite films, Fe, Cu, Ti, Ni, Mo, to Nb. The thickness of the overlayer ranges from a few nanometers to about 1 mm. Nucleation is attributed to the physical and chemical effects associated with changes to the substrate surface (the overlayer promotes carbon saturation at the substrate surface, and provide high-energy sites or nucleation centers), and changes in the gas chemistry in the immediate vicinity of the substrate surface.

The ion-implantation method has been used to modify the surface energy and surface structure of substrates in order to enhance diamond nucleation [Sood et al 1992]. Implantation of C^+ on Cu and As^+ on Si enhances diamond nucleation, while Ar^+ implantation on Si decreases nucleation density [Kobayashi et al 1993]. The lattice damages (strain, amorphous disorder and twinning) created by ion implantation are deemed to be responsible for nucleation enhancement. The strain is probably the primary physical reason for diamond nucleation enhancement on ion-implanted substrate.

Pulse-laser irradiation of thin buffer layer of a-C, WC, or cubic BN deposited on substrates (Cu, stainless steel, Si) leads to significant enhancement of both nucleation and adhesion of diamond films on substrates. It is speculated that the irradiation converts a portion of the a-C on the surface into diamond, or results in the formation of a reaction product that facilitates diamond nucleation. Carburization of substrates (Mo, W, Si, Fe/Si) also leads to nucleation enhancement owing to the formation of carbides and the saturation of carbon at the substrate surface.

Scratching and seeding are simple and effective method for diamond nucleation enhancement, although, they can cause surface damage and contamination. These pretreatment methods can be easily applied to substrates of complex geometry and shape. They are also compatible with many applications requiring extremely smooth, clean surfaces, such as diamond films

for electronic devices, optical window materials and smooth wear-resistant coatings. As an alternative, biasing or covering/coating substrate surface can yield high nucleation densities comparable to, or even better than those achieved by seeding or scratching, without significantly damaging the surfaces.

2.6.4 Deposition Conditions.

Deposition conditions such as substrate temperature, gas pressure, gas composition and gas activation critically influence nucleation density and rate. It has been noted that ideal deposition conditions for growth may not be optimal for nucleation. For example, in-situ surface analyses and microstructure characterization of the diamond nucleation process on negatively biased Si substrates [Stoner et al 1992] revealed that biasing could enhance nucleation significantly, but produces a much poorer quality diamond film if the biasing continued during the whole period of growth. Similarly, the optimal values of gas pressure and substrate temperature for growth are not identical to those for nucleation.

The overall dependence of nucleation density on substrate temperature is speculated to be caused by the change in the adsorption state and surface diffusion length of growth precursors. The precursors are adsorbed on the substrate mainly by physical adsorption below 900°C, and predominantly by chemical adsorption above this temperature, resulting in an abrupt increase in the diffusion length of the precursors around 900°C. As a result, the capture rate of the precursors (sticking probability) on the substrate surface, and hence the nucleation rate and density, drastically increase when the substrate temperature approaches 860°C [Hayashi et al 1992].

The effect of the filament temperature in HFCVD on nucleation is similar to that of the substrate temperature, i.e., with increasing filament temperature, nucleation density initially increases, reaches a maximum at 2100°C and

decreases thereafter [Park and Lee 1993]. The drop-off for T > 2100°C is explained by the observation that the etching of nucleation sites is enhanced with increasing filament temperature [Kim et al 1991].

In d.c. CVD [Hibino and Hayashi 1992], a nucleation density of 6×10^9 cm^{-2} was achieved on untreated substrates by increasing the discharge current to 1 A and the cathode temperature to 1400°C. It has also been suggested that diamond nucleation be enhanced by using high power densities, such as in plasma jet, or d.c. plasma discharge CVD, in which H_2 and CH_4 dissociation is promoted.

Low gas pressures (about 5 Torr) [Kim et al 1993], high CH_4 concentration, and high gas flow rates lead to high nucleation densities. The pressure dependence of nucleation density is explained [Silva et al 1996] by the competition effect between β-SiC formation, which increases the diamond nucleation density, and atomic-hydrogen etching, which decreases the number of nucleation sites. A high CH_4 concentration can promote carburization of the substrate surface and accelerate carbon saturation at the substrate surface [Bou et al 1992], while a high gas flow rate may increase the mass transfer of gas species to substrate surface. Consequently, diamond nucleation density can be enhanced [Ohtake and Yoshikawa 1993].

The addition of oxygen in gas mixture can accelerate the saturation of carbon on the substrate surface, reduce the incubation period, and promote a much faster diamond nucleation and growth than with oxygen-less plasmas [Shah and Waite 1992]. The presence of oxygen allows low substrate temperatures, preserves a good film quality at high CH_4 concentrations, and suppresses eventual surface contamination by Si [Bou et al 1992]. However, the addition of oxygen is also reported to suppress diamond nucleation by etching nucleation sites (graphite) on Ni and Pt substrate [Belton and Schmieg 1992].

The microwave power density for MPCVD process is another important

parameter that controls the H-atom concentration, in volume and at the interface [Liu and Dandy 1995]. It plays a crucial role on the quality and growth rate and determines the morphology and the texture of the films.

2.7 Properties of Diamond

Properties	CVD diamond	Natural diamond	Si	GaAs	SiC	cBN
Density (g cm^{-3})	2.8-3.51	3.567	2.42	5.32	3.16	3.48
Thermal Capacity at 27°C (J $mol^{-1}K^{-1}$)	6.12	6.195				
Standard entropy at 27°C (J mol^{-1})		2.428				
Effective Debye temperature at 0-827°C (K)		1860 ± 10				
Thermal conductivity at 25°C (W m^{-1} K^{-1})	2100	2200	230	50	320	1300
Thermal expansion coefficient at 25-200°C ($\times 10^{-6}$ $°C^{-1}$)	~2.0	0.8-1.2				
Band gap (eV)	~5.45	5.45	1.11	1.43	2.23	~ 7.5
Electrical resistivity (Ω cm)	10^{12}-10^{16}	10^{16}				
Dielectric constant at 45 MHz-20 GHz	5.6	5.7	11.7	10.9	9.7	7.1
Dielectric strength (V cm^{-1})	10^6	10^6				
Loss tangent at 45 MHz-20 GHz	<0.0001	-				
Saturated electron velocity ($\times 10^7$ cm s^{-1})	2.7	2.7				
Young's modulus (GPa) *	820-900 (0-800°C)	910-1250				
Compression strength (GPa)		8.68-16.53				
Poisson's ratio		0.10-0.16				
Vicker's hardness (GPa)	50-100	57-104				
Index of refraction at 10 μm	2.34-2.42	2.40				

Young's modulus = 895 {1-1.04×10^{-4}(T-20)} (GPa), where T is in °C)

Table 2.4 Properties of CVD diamond and single-crystal diamond [Piersonm 1993].

The most commonly known physical properties of diamond is that it is the hardest known material due to its rigid three-dimensional lattice. Diamond exhibits very high values of electrical breakdown field and intrinsic resistivity.

The low relative dielectric permittivity and possible negative electron affinity of diamond also stand out among other semiconducting materials. Selected other properties for both CVD diamond and natural diamond are summarized in table 2.4, along with comparisons with other materials.

2.8 Applications of Diamond

The microstructure, mechanical and electrical properties of diamond films offer many opportunities for applications in areas such as tribology, electro-emitting cold cathodes, microelectromechanical systems (MEMS), surface acoustic wave devices (SAW), electrochemical electrodes, and conformal coatings. A brief discussion of results obtained in some of these fields follows.

2.8.1 Mechanical Applications

The high hardness and abrasion resistance, along with high thermal conductivity and low coefficient of friction, of diamond have resulted in it finding extensive use in a wide variety of abrasive or cutting applications ranging from the rough cutting of stone and concrete to ultra-precision machining of electronic ceramics. The majority of diamond used for these applications is synthesized using HPHT growth techniques, and the size of diamond grit used depends on the application type:

(1) Rough applications, such as cutting, sawing, mining etc., use a girt size of about 3000 - 6500 μm;

(2) Precision applications, such as grinding, require 50 - 500 μm grit size

(3) Ultra-precision applications, such as fine grinding, lapping and polishing, use grits from 10 nm to 80 μm.

Previous research has demonstrated that the frictional behavior of diamond and diamond-like carbon films is governed by a combination of physical, chemical, and mechanical interactions at their sliding interfaces

[Hayward 1991]. The amount of friction resulting from a sliding contact can be divided into two major components: mechanical ploughing and physical/chemical attraction or adhesion [Bowden and Tabor 1986]. Rough diamond films were shown to cause ploughing, hence higher friction [Hayward 1992]. Apparently sharp asperity tips of rough diamond films can penetrate the softer counterfaces, giving rise to higher friction and wear. However, for smooth and polished diamond films or cleaved natural diamonds, the ploughing component of friction is thought to be minimal, and the amount of friction is then largely controlled by the extent of adhesive interaction across the sliding contact interfaces [Hayward 1992, Pepper 1982]. Results of sliding friction studies on nanocrystalline diamond films have been encouraging [Erdemir et al 1996, Zuiker et al 1995]. In air, long duration tests against Si_3N_4 balls give friction coefficients in the range 0.1–0.15 and wear rates of the diamond films of 3×10^{-7}/nm. These wear rates appear to reflect initial wear asperites. After wear track smoothing, wear rates become essentially immeasurable. In recent work, nanocrystalline diamond-coated SiC seal rings rotating at 3600 rpm have been tested at 100 psi water pressure. Because of a substantial reduction in torque and an increase in wear life, such coated seals could be a significant advance over the current state of the art in liquid pump seals. Nanocrystalline diamond film coatings have also been applied to seals using a dc-biased substrate and an oxyacetylene torch [Hogmark et al 1996, Hollman et al 1998].

2.8.2 Thermal Applications

As integrated circuit clock speeds and power densities increase and package footprints decrease the heat generated increases. Over the past decade the computing power has increased by five orders of magnitude [Windischmann 2001] and therefore thermal management has become an important consideration. A heat spreader attached to the integrated circuit can lower the operating temperature of the chip. Diamond is the most attractive candidate for this application because of its extremely high thermal

conductivity, at up to five times greater than that of copper. The advantages of CVD diamond over natural or high pressure diamond include the ability to achieve the desired thermal conductivity simply by tuning the fraction of hydrocarbon in the fuel gas supply and the ability to cover large areas of both planar and three-dimensional objects [Berman 1979]. Other benefits of CVD diamond include a thermal coefficient of expansion similar to silicon and gallium arsenide, low density and high electrical resistivity. The dramatic decrease in cost of CVD diamond over the past decade, from about USD 5000 per square centimeter to around USD 5 per square centimeter, has helped the case of diamond over other possible materials. Diamond heat spreaders have also proved beneficial for use with laser diode arrays.

2.8.3 Electronic Applications

One of the main areas of electronic applications for which diamond has been studied is that of solid state detectors, both for electromagnetic radiation, particularly UV and X-ray wavelengths, and particle radiations [Jackman 1998]. UV photodetectors fabricated at UCL have been one of the first commercially available electronic applications of diamond [Whitfield et al 1996]. Successful operations of CVD diamond based photodiodes and 1-dimentional imaging arrays have also demonstrated at UCL [Lansley 2001].

Remarkable electron emission with turn-on fields of ~1V/μm and current densities of 4×10^{-4} amps/cm^2 at 4V/μm has been achieved using nanocrystalline diamond films [McCauley et al 1998, Krauss et al 1998]. These results plotted according to the Fowler-Nordheim equation lead to an enhancement factor β of 5300, assuming the diamond band gap value of 5.5 eV as the work function of the material. For these nanocrystalline diamond films, as well as for electron-emitting DLC films, the mechanism of electron emission is a subject of intense current interest.

A recent model proposed by Robertson [1999] attempts to describe field

emission from DLC as the result of a non-uniform image dipole distribution associated with adsorbed hydrogen covering most of the surface, except for a few very small surface defects of unspecified origin. Because hydrogen is an electropositive adsorbate on carbon, hydrogen termination of the surface results in a dipole layer with the positive end pointing into the vacuum, and an induced accumulation of negative image charge just below the surface. At sites that are denuded of hydrogen, the neighboring image charge results in an enhanced electric field and a focusing mechanism for electrons ejected from the surface. The π-bonded grain boundaries in the phase-pure nanocrystalline films may give rise to the hydrogen-depleted surface sites required by Robertson's model, in addition to providing a conduction path for electron emission and replenishment.

2.8.4 Electrochemical Applications

The unique bulk and surface properties of diamond make it extremely attractive for applications in electroanalysis and electrochemical synthesis that could include sensor electrodes for in vitro or in vivo biomedical applications and sensors for long-term environmental studies, or use in molten salts or in highly radioactive environments. Diamond electrodes may find uses in chemically aggressive environments, for instance electrosynthesis of fluorinated compounds, anodic destruction of organic wastes, ozone synthesis, or molten-salt processes [Ferreira et al 2002]. Reactions at unusually high cathodic potentials, for example reduction of active metals, may be performed on diamond.

However, much still needs to be learned about electrochemistry on diamond electrodes before their potential can be fully realized [Swain et al 1998]. Diamond is an insulator with a band gap of 5.5 eV. Doping with boron to some deep levels will cause overlap of wave functions on neighboring acceptor centers. An impurity band develops imparting semiconductivity and even metallic conductivity on diamond. Recent experiments on nanocrystalline

diamond electrodes gave results that are quite similar to those obtained with conventionally grown but boron-doped electrodes [Gruen et al 1997]. The advantages of nanocrystalline films in this context would appear to be the fact that boron doping is not required and that corrosion protection of the underlying substrate can be achieved at considerably lower diamond film thicknesses.

2.8.5 Optical Applications

The broadband optical transparency of diamond, covering the near-UV, visible, near and far IR region, except for minor intrinsic absorption bands arising from two-phonon, 1332-2664 cm^{-1}, and three phonon, 2665-3994 cm^{-1}, makes it a suitable candidate for optical windows; the transmission spectrum of a high quality CVD diamond window (thickness 150 μm) is already reproducible [Wild and Koidl 2001]. Because of its excellent mechanical properties, diamond would be the material of choice for many MEMS applications, particularly those requiring the production of torque. Again, diamond's chemical inertness makes it ideally suitable as a corrosion protection material, e.g. to reduce turn-on voltages of field emitter arrays, conformal diamond coatings are required. In all these applications, films composed of micron-sized crystallites are inappropriate. Conformal coatings have already been successfully demonstrated using a proprietary nucleation procedure [Rotter 1998].

2.8.6 Summary

As potential applications of CVD diamond are continuously discovered, it may be expected that the ultimate economic impact of this emerging technology on the defense, space and commercial areas will outstrip that of high-temperature superconductors with more immediate applications. Possible large areas for the utilization of diamond thin films are listed in table 2.5.

Function	Field of application	Feature	Impact to industries
High Temperature semi-conductor	♦ Automobile & aircraft engines ♦ Household appliances	Heat resistant	♦ High reliability above 100°C
High frequency power transistor	♦ Microwave wireless LAN ♦ High speed transistor ♦ High speed data processing ♦ Non-contact admission	High breakdown field, High carrier mobility, High saturation velocity	♦ Efficient traffic &admission ♦ GHz band microwave amplification
High voltage transistor	♦ Electric power control	High breakdown field	♦ Smaller equipment
Electron emission	♦ Flat panel display	Negative electron affinity	♦ Displays of low energy consumption
Light emission	♦ Light emission and laser of blue & UV ♦ White luminescence ♦ Light source for printer	Wide band gap	♦ Ultra capacity photo recording, light source for medical inspection ♦ Large-size display ♦ Compact printer
Radiation sensing	♦ Digital X-ray image recording ♦ Nuclear reactor control	Radiation hard	♦ Medical application of X-ray ♦ Maintenance of nuclear power plant
Light detection	♦ Fire flame detection ♦ UV monitoring	Wide band gap	♦ Detection of accidents ♦ Environment measurement
Pressure sensing	♦ High sensitive distortion/pressure sensor at high temperature	High piezoresistivity, heat resistant	♦ High sensitivity monitoring
Temperature measurement	♦ High sensitive radiation detector	Wide band gap	♦ Optimal combustion control of automobile engines ♦ Maintenance of nuclear plant
Magnetic field measurement	♦ Magnetic sensing in harsh environment	Magnetoresistance effect	♦ Optimal control and detection of abnormal condition of rotating machines
x-ray window	♦ x-ray lithography mask	High transparency	♦ Submicron LSI fabrication
IR window	♦ IR window	High transparency	♦ environment measurement
Thermal propagation	♦ Heat sink	High thermal conductivity	♦ High reliable microwave module

Table 2.5 Industrial application of CVD diamond films [Kaufmann 1995, http://www.kobelco.co.jp/showroom/np0802e/np08021e.htm]

2.9 References

Akatsuka F and Shimura F, in Applications of Diamond Films and Related Materials, eds. Tzeng Y, Yoshikawa M, Murakawa M and Feldman A, Elsevier, Amsterdam (1991).

Ascarelli P and Fontana S, Appl. Surf. Sci. **64** (1993) 307.

Augus JC, Wang Y and Sunkara M, Ann. Rev. Mater. Sci. **21** (1991) 221.

Badzian AR and Badzian T, Surf. Coat. Technol. **36** (1988) 283.

Belton DN and Schmieg SJ, Surf. Sci. **233** (1990) 131.

Belton DN and Schmieg SJ, Thin Solid Films **212** (1992) 68.

Berman R, in The Properties of Diamond, ed. Field JE, Academic Press, London (1979).

Bou P, Vandenbulcke L, Herbin R and Hillion F, J. Mater. Res. **7** (1992) 150.

Bowden FP and Tabor D, Friction and Lubrication of Solids, Oxford University Press, Oxford (1986).

Chen CF, 1st Int. Conf. Diamond Sci. and Technol, Oct. 24-26, Tokyo (1988) 118.

Dennig PA and Stevenson DA, Appl. Phys. Lett. **60** (1991) 1562.

Dresselhaus MS and Kalish R, Ion Implantation in Diamond, Graphite and Related Materials, Springer-Verlag, Berlin (1992).

Erdemir A, Bindal C, Fenske GR, Zuiker C, Krauss A and Gruen D, Diamond Rel. Mater. **5** (1996) 923.

Field JE, The Properties of Diamond, Academic Press, London (1979).

Konov VI, Pimenov SM, Erdemir A, Halter M, Fenske GR, Krauss A and Gruen DM, Surf. Coat. Technol. **94/95** (1997) 537.

Fabisiak K, Maar-Stumm M and Blank E, Diamond Rel. Mater. **2** (1993) 722.

Ferreira NG, Silva LLG and Corat EJ, Diamond and Related Materials **11** (2002) 657.

Goerge MA, Burger A, Collins WE, Davidson JL, Barners AV and Tolk NH, J. Appl. Phys. **76** (1994) 4099.

Gruen DM, Annu. Rev. Mater. Sci. **29** (1999) 211.

Gruen DM, Krauss AR, Zhou D, McCauley TG and Corrigan TD, in Chemical Vapor Deposition, eds. MD Allendorf and C Bernard, The Electrochem. Soc., Pennington (1997).

Hayashi Y, Drawl W and Messier R, Jpn. J. Appl. Phys. **31** (1992) L193

Hayward IP, Surf. Coat. Technol. **49** (1991) 554.

Hayward IP, Singer IL and Seitzman LE, Wear **157** (1992) 215.

Hibino Y and Hayashi Y, Surf. Coat. Technol. **54-55** (1992) 365.

Hogmark S, Hollman P, Alahelisten A and Hedenqvist P, Wear **200** (1996) 225.

Hollman P, W¨anstrand O, Hogmark S, Diamond Rel. Mater. **7** (1998)1471.

Ihara M, Komiyama H and Okubo T, Appl. Phys. Lett. **65** (1994) 1192.

Jackman RB, in Low-Pressure Synthetic Diamond Manufacturing and Applications, eds. Dischler B and Wild C, Springer-Verlag, Berlin (1998).

Jansen F, Machonkin MA and Kuhman DE, J. Vac. Sci. Technol. A8 (1990) 3785.

Kaufmann H, Surf. Coat. Technol. **74-75** (1995) 23.

Kiflawi I and Lawson SC, in Properties, Growth and Applications of Diamond, eds. Nazaré MH and Neves AJ, INSPEC, The Institute of Electrical Engineers, London, UK (2001).

Kim D, Lee H and Lee J, J. Mater. Sci. **28** (1993) 6704.

Kim JW, Baik YJ and Eun KY, in Tzeng Y, Yoshikara M, Murakara M and Feidman A (eds.) Applications of Diamond Films and Related Materials, Elsevier, Amsterdam (1991).

Kobayashi K, Kumagai M, Karasawa S, Watanabe T and Togashi F, J. Cryst. Growth **128** (1993) 408.

Kobayashi K, Mutsukura N and Machi Y, Mater. Manufact. Proc. **7** (1992) 395.

Komori M, Maki T, Kim T, Hou G, Sakaguchi Y, Sakuta K and Kobayashi T, Appl. Phys. Lett. **62** (1993) 582.

Krauss AR, Gruen DM, Zhou D, McCauley TG, Qin LC, et al, Mater.Res. Soc. Symp. Proc. **495** (1998) 299.

Lambrecht WRL, Lee CH, Segall B, Angus JC, Li Z and Sunkara M, Nature **364**

(1993) 607.

Lansley SP, PhD Thesis, University College London, 2001.

Lin SJ, Lee SL, Hwang J, Chang CS and Wen HY, Appl. Phys. Lett. **60** (1992) 1559.

Liu H, Dandy DS, Diamond Rel. Mater. **4** (1995) 1173.

Locher R, Wild C, Muller-Serbert W, Kohl R and Koidl P, Diamond Rel. Mater. **2** (1993) 1248.

Lux B and Haubner R, in Diamond and Diamond-like Films and Coatings, eds. Clausing RE, Horton LL, Augus JC and Koidl P, Plenum Press, New York (1991).

McCauley TG, Corrigan TD, Krauss AR and Auciello O, Mater. Res. Soc. Symp. Proc. **498** (1998) 227.

Matsumoto S and Matsui Y, J. Mater. Sci. **18** (1983) 1785.

Meilunas R, Wong MS, Sheng KC, Chang RPH and Vanduyne RP, Appl. Phys. Lett. **54** (1989) 2204.

National Materials Advisory Board, Status and Applications of Diamond and Diamond-like Materials: an Emerging Technology, NMAB-445, National Academy Press, Washington, D. C. (1990).

Ohtake N and Yoshikawa M, Jpn. J. Appl. Phys. **32** (5A) (1993) 2067.

Ong TP, Xiong F, Chang RPH and White CW, Appl. Phys. Lett. **60** (1992) 2083.

Ong TP, Xiong F, Chang RPH and White CW, J. Mater. Res. **7** (1992) 2429.

Park S and Lee J, J. Mater. Sci. **28** (1993) 1799.

Patterson DE, Bai BJ, Chu CJ, Hauge RH and Margrave JL, in New Diamond Science and Technology, eds. Messier RF, Glass JT, Butler JE & Roy R, Materials Research Society, Pittsburgh (1991).

Pepper SV, J. Vac. Sci. Technol. **20** (1982) 643.

Piersonm HO, Handbook of Carbon, Graphite, Diamond and Fullerenes, Noyes, Park Ridge, NJ (1993).

Prelas MA, Popovici G and Bigelow LK, Handbook of Industrial Diamonds and Diamond Films, Marcel Dekker, Inc., New York (1998).

Robertson J, personal communications (1999).

Rotter S, Isr. J. Chem. **38** (1998) 135.

Seino Y and Nagai S, J. Mater. Sci. Lett. **12** (1993) 324.

Shah SI and Waite MM, Appl. Phys. Lett. **61** (1992) 3113.

Shih HC, Sung CP and Wan WL, Surf. Coat. Technol. **54-55** (1992) 380.

Silva F, Gicquel A, Tardieu A, Cledat P and Chauveau TH, Diamond Rel. Mater. **5** (1996) 338.

Singh J and Vellaikal M, J. Appl. Phys. **73** (1993) 2831.

Singh. J, J. Mater. Sci. **29** (1994) 2761.

Smolin AA, Pimenov SM, Ralchenov VG, Kononenko TK and Loubnin EN, Diamond Films Technol. **3** (1993) 1.

Sood DK, Drawl WR and Messier R, Surf. Coat. Technol. **51** (1992) 307.

Stoner BR, Williams BE, Wolter SD, Nishimura K and Glass JT, J. Mater. Res. **7** (1992) 1.

Stoner BR, Ma GHM, Wolter SD and Glass JT, Phys. Rev. **B45** (1992) 11067.

Swain GM, Anderson AB and Angus J, MRS Bull. **23** (1998) 56.

Lambrecht WRL, Lee CH, Segall B, Angus JC, Li Z and Sunkara M, Nature **364** (1993) 607.

Waite MM and Shah SI, Appl. Phys Lett. **60** (1992) 2344.

Whitfield MD, Chan SSM and Jackman RB, Appl. Phys. Lett. **68** (1996) 290.

Wild C and Koidl P, in Properties, Growth and Applications of Diamond, eds. Nazaré MH and Neves AJ, INSPEC, The Institute of Electrical Engineers, London, UK (2001).

Wild C, Koidl P, Muller-serbert W, Walcher H, Kohl R, Herres N, Locher R, Samlenski R and Brenn R, Diamond Rel. Mater. **2** (1993) 158.

Windischmann H, CVD Diamond for Thermal Management, in Propeties, Growth and Applications of Diamond, ed. Nazaré MH and Neves AJ, INSPEC, The Institute of Electrical Engineers, London, UK (2001)

Wolter SD and Glass JT, Bias induced diamond nucleation studies on refractory

metal substrates, J. Appl. Phys. **77** (1995) 5119.

Wolter SD, Stoner BR, Glass JT, Ellis PJ, Buhaenko DS, Jenkins CE and Southworth P, Appl. Phys. Lett. **62** (1993) 1215.

Yarbrough WA, in Applications of Diamond Films and Related Materials, eds. Tzeng Y, Yoshikawa M, Murakawa M and Feldman A, Elsevier, Amsterdam (1991).

Yarbrough WA and Messier R, Science **247** (1990) 688.

Yehoda JE, Fuentes RI, Tsang JC, Whitehair SJ, Guarnieire CR and Cuomo JJ, Appl. Phys. Lett. **60** (1992) 2865.

Yuasa M, Kawarada H, Wei J, Ma J, Suzuki J, Okada S and Hiraki A, Surf. Coat. Technol. **49** (1991) 374.

Yugo S, Kanai T, Kimura T and Muto T, Appl. Phys. Lett. **58** (1991) 1036.

Zuiker C, Krauss AR, Gruen DM, Pan X, and Li JC, Csencsits R, Erdemir A, Bindal C and Fenske G, Thin Solid Films **270** (1995) 154.

Chapter 3

Impedance Theory

3.1 Introduction

Impedance spectroscopy is a powerful technique to characterize the electrical properties of materials and their interfaces with electrically conducting electrodes. The technique may be used to investigate the dynamics of bound or mobile charges in bulk or interface regions of any kind of ionic solids, or liquid materials, semiconductors, mixed ionic-electronic materials and insulators (dielectrics). The technique measures the impedance as a function of frequency automatically in the range of 1 mHz to 10 MHz and is easily interfaced to the computer. The technique has been comprehensively reviewed in a recent book [Macdonald 1987].

The complex impedance measurements are capable of separating the various contributions such as bulk, grain boundary and electrode, to total conductivity. Hence this technique is able to extract the data which allow these phenomena to be isolated. Spectroscopic impedance studies on diamond films form the basis of this thesis; as such the current status, models, and fundamental applications and interpretations related to this technique are crucial to the thesis. This chapter provides detailed background information based on both theoretical and empirical knowledge in this area.

Starting with general concepts of electrochemical impedance, the principle of this technique is presented. The utilization of this technique to characterize the grains and grain boundaries contribution are discussed in details. The equivalent electrical circuits are presented in order to compare with real materials system. Next, formulae for the capacitance of one-layer and two-layer dielectrics models, with either in-plane or cross-section electrode configuration are presented as references for the following chapters. Finally, from the microscopic point of view, different mechanisms on dielectric relaxation and polarization are summarized.

3.2 Impedance Principle

Electrochemical impedance is the frequency-dependent complex valued proportionality factor which is a ratio between the applied potential and current signal. For the sake of simplicity, the impedance plots for the resistor-capacitor (*R*-*C*) in parallel with a series resistor network (see figure 3.1 a), will be considered in some detail. The reason for choosing this circuit is because many of the electrochemical systems encountered in practice are actually modelled using this network [Macdonald 1987].

The term resistance and impedance both imply an obstruction to current or electron flow. When dealing with a direct current (DC), only resistors provide this effect. However, for the case of an alternating current (AC), circuit elements such as capacitors and inductors can also influence the electron flow. These elements can affect not only the magnitude of an AC wave form, but also its time-dependent characteristics or phase. In DC theory, where the frequency equals 0 Hz, a resistance is defined by the Ohm's Law:

$$E=IR \qquad (3.1)$$

E= applied potential

I= resulting current

R= resistance

For an AC current, where the frequency exceeds zero, this is represented by

$$E=IZ \qquad \text{Ohm's Law with frequency } >0 \qquad (3.2)$$

E= applied potential

I= resulting current

Z= impedance, the AC equivalent of resistance

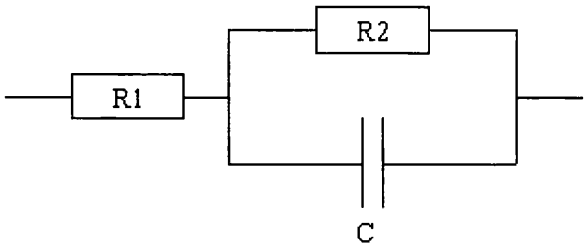

(a)

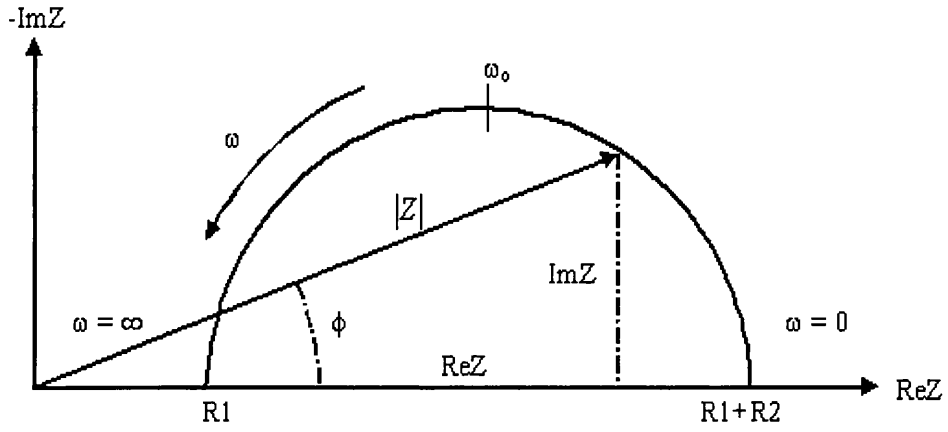

(b)

High frequency: $Z'' \Rightarrow 0$, $Z' \Rightarrow R_1$

Low frequency: $Z'' \Rightarrow 0$, $Z' \Rightarrow R_1+R_2$

Figure 3.1 Equivalent circuit and AC impedance plots of an electrochemical cell with one time constant: (a)Equivalent circuit, (b)Cole-Cole plot in the complex plane, $\omega_b=1/(R_2C)$.

The mathematical contribution of the plot (figure 3.1 a) is based on a vector diagram, corresponding to a sine wave *E* and a sine wave *I*. This is because sine wave analysis is the most appropriate for electrochemical impedance studies to date. The current sine wave can be described by the following equation:

$$I = A \sin(\omega t+\phi) \quad (3.3)$$

$$\omega = 2\pi f \quad (3.4)$$

A= maximum amplitude

ω=frequency in radians/sec

f= frequency in Hz

ϕ= phase shift in radians

The impedance $Z(\omega)$ is a complex number which can be represented either in polar co-ordinates or in Cartesian co-ordinates:

$$Z(\omega) = |Z|e^{j\phi} \tag{3.5}$$

$$Z(\omega) = ReZ + j\,ImZ \tag{3.6}$$

where ReZ and ImZ are the real part and the imaginary part of the impedance, respectively. The relationships between theses quantities are:

$$|Z|^2 = (\mathrm{Re}\,Z)^2 + (\mathrm{Im}\,Z)^2 \tag{3.7}$$

$$\phi = Arc\ tan\ \frac{\mathrm{Im}\,Z}{\mathrm{Re}\,Z} \tag{3.8}$$

$$\mathrm{Re}\,Z = |Z|\cos\phi \tag{3.9}$$

$$\mathrm{Im}\,Z = |Z|\sin\phi \tag{3.10}$$

In figure 3.1 (a) the equivalent circuit of an electrochemical interface is depicted, its impedance is :

$$Z(\omega) = \frac{E}{I} = R_1 + \frac{1}{\frac{1}{R_2} + jC\omega} = R_1 + \frac{R_2}{1+\omega^2C^2R_2^{\,2}} - \frac{j\omega CR_2^{\,2}}{1+\omega^2C^2R_2^{\,2}} \tag{3.11}$$

E is the voltage

I is the current

R_1 and R_2 are the resistance values of the equivalent circuit

C is the capacitance value of the equivalent circuit

Furthermore,

$$|Z(\omega)| = \sqrt{(R_1 + \frac{R_2}{1+\omega^2 C^2 R_2^{\ 2}})^2 + (\frac{\omega C^2 R_2^{\ 2}}{1+\omega^2 C^2 R_2^{\ 2}})^2} \qquad (3.12)$$

when ω tends to zero, $|Z(\omega)|$ equals to R_1+R_2

when ω tends to infinite, $|Z(\omega)|$ equals to R_1

Note that the difference between the two limits is R_2. Therefore, the high frequency intercept determines R_1 (the series resistance), whereas the low frequency intercept yields the sum of R_1+R_2. In simple terms, this means that at high frequencies, the capacitor conducts the current easily. Consequently the impedance is solely due to the resistance R_1; whereas at low frequencies, the current flow via the capacitor is impeded. The current therefore flows through R_1 and R_2, and the impedance is given by the sum of the two resistors. At intermediate frequencies, the impedance takes a value somewhere between R_1 and R_1+R_2 and thus has both real and imaginary components. This gives rise to the Cole-Cole plot semicircular shape, which corresponds to the equation as follows:

$$\left[Z'-(R_1 + \frac{R_2}{2})\right]^2 + Z''^2 = (\frac{R_2}{2})^2 \qquad (3.13)$$

It has been shown that equation (3.13) is analogous to the equation of a circle, with a radius of $\frac{R_2}{2}$ and a centre at $(R_1 + \frac{R_2}{2}, 0)$. In all the materials studied, ω, R_1 and R_2 are greater than zero, thus resulting in a semicircle on the axis when plotted as function of frequency. $Z(\omega)$ is plotted in figure 3.1 (b) in terms of a Cole-Cole plot in the complex plane with the negative imaginary parts above the real axis, as is usually used in electrochemistry.

At the peak of the semicircle, the following condition is obtained:

$$\omega_{max} R_2 C = 1 \tag{3.14}$$

and hence

$$C = \frac{1}{2\pi f_{max} R_2} \tag{3.15}$$

where the equation (3.4) has been used. Knowing the value of R_2 and the frequency f_{max}, the value of the capacitance can be determined. It is possible to obtain all the three parameters (R_1, R_2 and C) from the Cole-Cole plot as shown in figure 3.1 (b), provided a sufficient frequency range is investigated.

The application of impedance spectroscopy to the characterization of polycrystalline materials started after Bauerle [1969] showed that for Zirconia with platinum electrodes the individual polarizations of grain interiors, grain boundaries, and electrodes could be resolved in the admittance plane. He presented an equivalent circuit for his results, which have now proven to be typical of most of solid electrolytes. In such a circuit, the individual elements correspond to grain interiors, grain boundaries, and electrode connected in series. However, estimation of the circuit parameters was made complicated by Bauerle's choice of the admittance plane. Many subsequent researchers have therefore preferred to work in the impedance plane, i.e. Cole-Cole plot, where a more direct relationship exists between the spectrum and the circuit [Armstrong et al 1974, Schouler et al 1981]. The level of agreement between experiment and simulation is quite satisfactory for the grain interior and grain boundary arcs both in terms of shape and distribution of frequencies on the arcs, therefore supporting the view that equivalent circuits are a meaningful way of representing the data.

Measurement of the electrical conductivity for polycrystalline materials using impedance spectroscopy provides information related to the electrical behaviour of the grain interiors, the grain boundary regions and electrode. This is illustrated in figure 3.2 (a), which contains the equivalent circuit for the electrical response of a polycrystalline material. The simple *R*-*C* parallel circuit in which three components are connected in series is often used to study the AC impedance behaviour of materials. This circuit has a direct relationship to the complex impedance plot (figure 3.2 (b)) in which Z'', the imaginary part of the complex impedance, is plotted against Z', the real part, for a wide range of frequencies (typically 10^{-1}-10^{7} Hz). The frequency increases as shown by the arrow in figure 3.2 (b). The highest frequency is located at the origin. The resistances R_{gi}, R_{gb} and R_e corresponding to the grain interior, grain boundary and electrode, respectively, can be obtained from the intersections on the real axis of the corresponding semicircular arc. Comparing with the other two, R_e can normally be ignored except for the case of imperfect ohmic contacts which cause interfacial contact resistance. The capacitances C_{gi}, C_{gb} and C_e corresponding to the grain interior, grain boundary and electrode, respectively, can be obtained from equation (3.15) [Hench and West, 1989].

The relationship between microstructural models and circuits shows its real merit when used to correlate the equivalent circuit parameters of a material with changes in the external conditions or the microstructure of the material. For example, in ceramics, where it is possible to resolve the resistances due to the grain interiors and the grain boundaries, it has facilitated the study of some important processes; namely sintering, grain growth and solid state precipitation. In diamond it can facilitate the investigation of nucleation, growth, doping process, grain boundary deterioration and nanocrystallization.

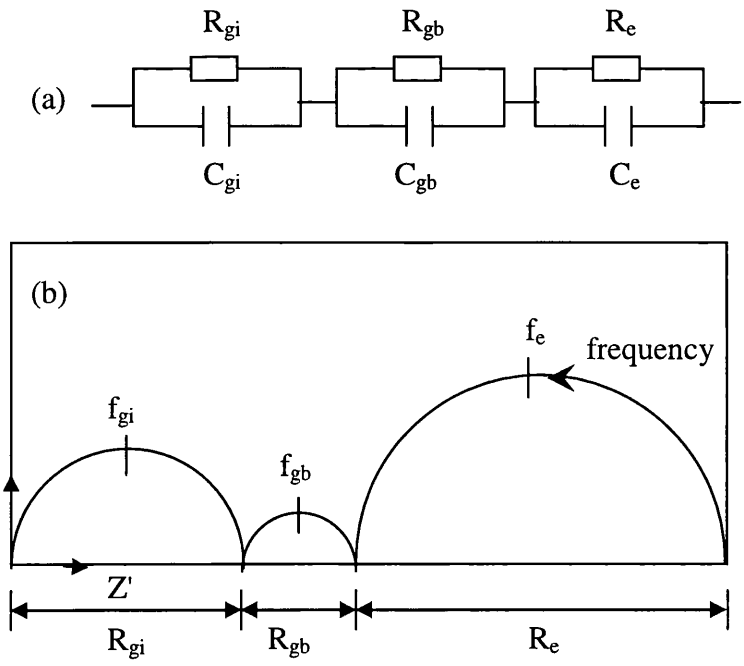

Figure 3.2 (a) An equivalent circuit representing a polycrystalline material. (b) An idealized complex impedance plot for a polycrystalline material showing contributions from the grain interiors (gi), grain boundaries (gb) and electrode interface (e). Note: Ce>>Cgb>>Cgi.

3.3 Conductivity Models

The impedance plots of polycrystalline materials can be related to their microstructure by means of physical models of the grain interior, grain boundary and the electrode behaviour. Three physical models used to describe the electronic materials are reviewed in details with their respective circuit equivalents [Khan 1990].

The early model used to describe the properties of two phase mixture is the series layer model. The model describes that the two phases are assumed to be stacked in layers parallel to the measuring electrodes, with total thickness of each phase made proportional to volume fractions X_1 and X_2. This model shows a linear mixing rule for the complex resistivity (ρ). The complex resistivity is the sum of the individual phase resistivity (ρ_1 and ρ_2):

$$\rho = X_1\rho_1 + X_2\,\rho_2 \qquad (3.16)$$

In the parallel circuit model the two phases are assumed to be stacked across the electrodes. For this model, the complex conductivity (σ) rather than resistivity follows a linear mixing rule:

$$\sigma = X_1\sigma_1 + X_2\sigma_2 \qquad (3.17)$$

The widely used physical model is a more realistic one, which treats the microstructure as an array of cubic shaped grains with flat grain boundaries of finite thickness as shown in figure 3.3 [Tuller 2000].

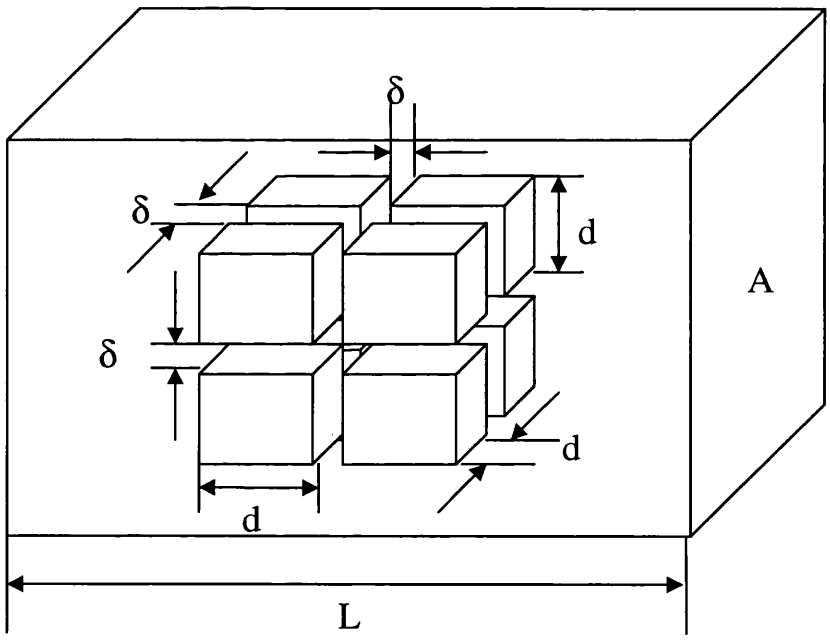

Figure 3.3 Brick layer model of idealized polycrystalline structure in which grains of dimensions d^3 are separated by grain boundaries of width δ [Maier 1995].

The volume fraction of grain boundaries is $3\delta/d$ (δ is grain boundary thickness and d is grain size) [Khan 1990]. The current flow is assumed to be one dimensional and the current path at the corners of the grains is neglected. In this case the two paths available to the current are either through the grains and across the grain boundary, or along grain boundaries, as depicted in figure 3.3. Depending on the relative magnitudes of grain and grain boundary conductivity one of the two paths may dominate. This model has been applied to many material systems and according to this model the bulk resistivity and the grain boundary resistivity may have different response [Tuller 2000].

In the brick layer model, the grain interior response will be displaced from the grain boundary response depending on the relaxation rate of charged species within each region. It is normal to compare the relaxation rates of different processes in terms of rate constant or relaxation time (τ), this can be defined as:

$$\tau=RC \tag{3.18}$$

In terms of grain interior rate constant, τ_{gi} can be expressed as follows:

$$R_{gi}=\frac{L}{A\sigma_{gi}} \tag{3.19}$$

$$C_{gi}=\frac{A\varepsilon_o\varepsilon_{gi}}{L} \tag{3.20}$$

Therefore;

$$\tau_{gi}=\frac{\varepsilon_o\varepsilon_{gi}}{\sigma_{gi}} \tag{3.21}$$

where L is the sample length, A is the cross sectional area, ε_o is the permittivity of free space ($8.854\text{x}10^{-12}$ F/m), and σ_{gi} and ε_{gi} are the electrical conductivity and relative dielectric constant of the grain interior respectively.

The grain boundary relaxation time constant τ_{gb} can be expressed as follows [Maier 1995];

$$R_{gb} = \frac{L}{A\sigma_{sgb}}\frac{\delta}{d} \tag{3.22}$$

$$C_{gb} = \frac{A\varepsilon_o\varepsilon_{gb}}{L}\frac{d}{\delta} \tag{3.23}$$

Therefore;

$$\tau_{gb} = \frac{\varepsilon_o\varepsilon_{gb}}{\sigma_{sgb}} \tag{3.24}$$

where d is the grain size, δ is the grain boundary width, and σ_{sgb} and ε_{gb} are the specific electrical conductivity and relative dielectric constant of the grain boundary, respectively. The resistance of the grain boundary is normally associated with the presence of a second phase or a constriction resistance, which can also result in a space charge region at the grain boundary. The capacitance of this region is thus associated with the polarization at the interface.

By applying the brick layer model and classic identification criteria comprehensively discussed in the literature [Macdonald 1987, Van Dijk and Burggraaf 1981, Verkerk et al 1982, Godickemeier 1994, Fleig 2000, M'Peko et al 2002], bulk (at high frequencies) and grain boundary (at low frequencies) contributions to the total materials' impedance were in each case distinguished. This can be explained by the different relaxation rate of charged species within each region or the different RC relaxation time of the elements. The defects, non-diamond phases and impurities are believed to be accumulated preferentially within the grain boundaries than grain lattices [Nistor et al 1997]. The grain boundaries may induce dipole movements which respond to an applied field with a delay [Daniel 1967]. Thus the grain boundary contributions with a long relaxation time usually happen in the low frequencies and the grain bulk contributions with a short relaxation time in the high frequencies. In most cases, the sufficient difference in the capacitance of the RC equivalent circuit

rather than the resistance results in the two semicircles separated on the complex Cole-Cole plane. [Hodge 1975].

The capacitance values of the grain boundary and grain interior are reported in the order of 10^{-9} F and 10^{-12} F respectively for many polycrystalline material systems, for example, zirconia [Khan 1990], bismuch titanate [Huanosta et al 1991], ferroelectrics [Kumar and Ye 2001], and polycrystalline diamond [Garcia et al 1997].

One may ask why different materials show the similar capacitance values (10^{-9} F for grain boundaries and 10^{-12} F for the grain interiors) when analyzed in the Cole-Cole plot. The reason for this may be explained from the definition of the capacitance value itself as shown in equation (3.20) and (3.23). The theoretical capacitance value associated with grain interiors has been defined in equation (3.20). In practice, all the geometric parameters in this equation are not infinite in order to facilitate to carry out these experiments on a research laboratory basis. Thus these geometric parameters normally have their expected magnitude order. L is the sample length within the order of millimetre (mm). A is the cross sectional area within the order of 10 millimetre square (10 mm^2). ε_o is the permittivity of free space (8.854×10^{-12} F/m). ε_{gi} is the relative dielectric constant of the grain interior of the sample. For high purity diamond, the dielectric constant is reported around 5.7. [Davis 1993]. Thus the formula (3.20) indicates that the grain interior capacitance from diamond is estimated around 0.5 pF.

The same A and L values can be applied to the grain boundary capacitance in equation (2.23). In addition, the grain boundary induced dipole polarization may cause the dielectric constant (ε_{gb}) to be slightly higher than that of grain bulk (ε_{gi}), but probably on the same magnitude order as grain bulk [Daniel 1967]. Furthermore, the grain size of a typical polycrystalline material is usually on the order of micrometers (μm), where the effective grain boundary width is expected to be on the order of nanometres (nm) [Aoki et al 1996]. Thus

the estimated grain boundary capacitance for a polycrystalline diamond is around 0.5 nF.

To gain further insight into these quantitative estimations, the ratio of the grain interior capacitance and grain boundary capacitance may be considered as follows:

$$\frac{C_{gi}}{C_{gb}} \approx \frac{\delta}{d} \tag{3.25}$$

The equation (3.25) indicates that the ratio of the grain capacitance and grain boundary capacitance is proportional to the ratio of the grain boundary width (δ) and grain size (d). In other words, the difference between the grain interior capacitance and grain boundary capacitance mainly originates from the geometric effect of the sample. This effect may be controlled by the following factors such as grain size, anisotropy, and porosity [Macdonald 1987]. The typical geometric characteristic within a polycrystalline material leads to the grain boundary capacitance is normally two or three orders of magnitude higher than the grain interior capacitance.

The above discussion gives an explanation on the origin of the classic procedures and identification criteria for the grain boundary and grain bulk contributions in an ideal condition. In practise, it is difficult to calculate the theoretical capacitance of grain interior and grain boundaries for diamond. This is because the in-plane electrode measurement makes it unlikely to define the specific length and area of each sample. Cross-section electrode measurements make the geometric parameters solved easily, but most of impedance data can not be detected across the samples due to extremely high resistance in diamond. So the conduction path identification criteria used in this thesis are emphasized on practical and empirical interpretations of materials based on the brick layer model discussed here.

3.4 Equivalent Circuits

This section presents impedance characterization on real electronic circuits made of resistors and capacitors rather than materials. Two types of circuits (*R-C* parallel and double *R-C* parallel in series) have been studied. The impedance spectroscopy obtained from electronic circuits is analogous to that obtained from materials. Thus impedance properties of materials can be represented by the relevant circuits, namely, equivalent circuits.

3.4.1 Resistor and Capacitor in Parallel

Figure 3.4 shows the impedance data for the circuit that has both a resistive and a capacitive component connected in parallel. The Cole-Cole plot is presented in a complex plane, where the negative values of the imaginary part (*-Im Z*) on the *y* axis are versus the real part (*Re Z*) on the *x* axis. Each data point corresponds to a different frequency. When represented in the Cole-Cole plot, the impedance spectra lead to a succession of semicircles. The resistor represents either ionic or electric conduction mechanism, whilst the capacitor represents the polarizability of the material.

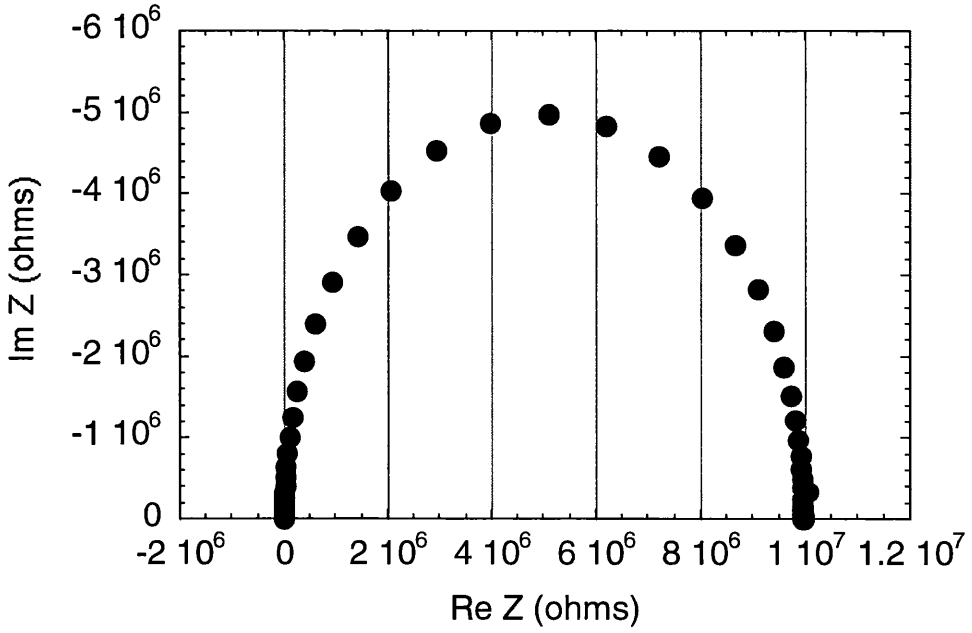

Figure 3.4 *R-C* in parallel

The complex impedance Z^* measured by impedance spectroscopy can be expressed as a function of the resistance R and capacitance C, as follows:

$$Z^* = Z'-jZ'' \tag{3.26}$$

$$Z' = \frac{R}{1+\omega^2 R^2 C^2} \tag{3.27}$$

$$Z'' = \frac{\omega R^2 C}{1+\omega^2 R^2 C^2} \tag{3.28}$$

$$(Z'-\frac{R}{2})^2 + Z''^2 = (\frac{R}{2})^2 \tag{3.29}$$

Here, Z' and Z'' represent the real and imaginary parts of the impedance, respectively, and ω is the angular frequency. When plotted for different frequencies in a complex plane, equation (3.29) takes the form of a semicircle. In this case, the second intercept of the semicircle with the real axis is the bulk resistance (R) of the sample. This equivalent circuit can be used to represent the properties of both single crystalline diamond films and polycrystalline diamond films with one dominating conduction path. Table 3.1 compares the AC impedance for basic circuit elements, such as resistor (R), capacitor (C) and inductor (L). These are the basis of the AC electronic circuits.

Table 3.1 AC impedances for circuit elements, namely, resistor (R), capacitor (C) and inductor (L).

Circuit Element	*AC Impedance Equation*	
Resistor (R)	$z = R + 0j$	$j = \sqrt{-1}$
Capacitor (C)	$z = 0 - \frac{j}{\omega C}$	$\omega = 2\pi f$
Inductor (L)	$z = 0 + j\omega L$	$\omega = 2\pi f$

3.4.2 *Double Resistor and Capacitor Parallel in Series*

Figure 3.5 shows the impedance spectrum for the double resistor and capacitor parallel in series. The circuit has a direct relationship to the Cole-Cole plot. The highest frequency is located at the origin. The resistances R_1 and R_2 can be obtained from the diameters of the semicircular in this plot. Here the resistor R represents either an ionic or an electronic conduction mechanism, while the capacitor C represents the polarizability of the diamond. The symbols R_1, R_2, C_1, and C_2 have the same meanings as before for two-layer dielectrics.

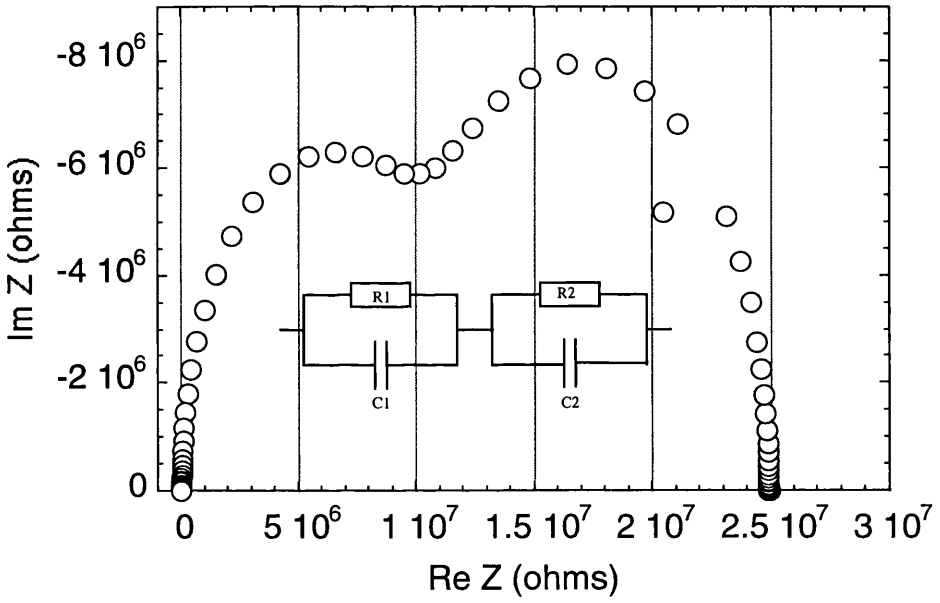

Figure 3.5 Double *R-C* Parallel in Series

The measured complex impedance Z can be expressed as a function of R_1, R_2, C_1 and C_2 in the following way:

$$Z^* = Z' - j\,Z'' \tag{3.30}$$

$$Z' = \frac{R_1}{1+\omega^2 R_1^{\,2} C_1^{\,2}} + \frac{R_2}{1+\omega^2 R_2^{\,2} C_2^{\,2}} \tag{3.31}$$

$$Z'' = \frac{\omega R_1^{\,2} C_1}{1+\omega^2 R_1^{\,2} C_1^{\,2}} + \frac{\omega R_2^{\,2} C_2}{1+\omega^2 R_2^{\,2} C_2^{\,2}} \tag{3.32}$$

where Z' and Z'' represent the real and imaginary portions of the impedance, respectively, and ω is the angular frequency. When plotted in a complex plane, Z'' versus Z' takes the form of two semicircles. In such a representation, a two-layer contribution is easily identified. Note that critical to the identification of each single resistor and capacitor in parallel is the simulated capacitance value for each semicircle. This model is well suited to simulate the resistance and capacitance associated with the grain boundary and grain interior.

3.5 Formulae for the Capacitance

It is known that the electrical contribution from grains, grain boundaries and/or electrodes for a certain polycrystalline material system can be extracted and separated. As such the simulated capacitance value obtained in each Cole-Cole plot plays a crucial role in assigning the origin of each semicircle response. Therefore, understanding and calculating the dielectric parameters especially the capacitance value become essential. This section describes the formulae for the capacitance in both one-layer and two-layer dielectrics.

3.5.1 One-layer Model

When a voltage is applied to a parallel-plate capacitor in vacuum, the capacitor will store charge. In the presence of a dielectric, an additional phenomenon happens within the dielectric, which allows the capacitor to store more charge.

For an empty plate capacitor, the capacitance in the electrostatic system is given by:

$$C_0 = \frac{area}{4\pi d} \tag{3.33}$$

where d is the distance between plates.

$$C = 4\pi\varepsilon_0 C_0 \tag{3.34}$$

Note that these formulae neglect the fringing of the field at the edges of the capacitor plates. When a capacitor is filled with a dielectric, its static capacitance is given by:

$$C = 4\pi\varepsilon_0\varepsilon_s C_0 \tag{3.35}$$

Here again, fringe fields have been neglected.

The capacitance under dynamic conditions may be expressed in terms of $\varepsilon^*(\omega)$.

The complex capacitance thus becomes:

$$C^*(\omega) = 4\pi\varepsilon_0 C_0 \varepsilon^*(\omega). \tag{3.36}$$

Alternating current measurements give the impedance $Z^*(\omega)$ of the capacitor containing the dielectric, which is related to the complex capacitance by

$$Z^*(\omega) = \frac{1}{i\omega C^*(\omega)} \tag{3.37}$$

The impedance can be represented by an equivalent circuit. For a given frequency ω an impedance can be represented by a large number of possible equivalent circuits, the simplest of which are the parallel and the series circuit.

Table 3.2 Characteristics of R-C circuits in series and in parallel at a given frequency, respectively.

Circuit	R_s and C_s in series	R_p and C_p in parallel
$Z^*(\omega)$	$R_s - \frac{i}{\omega C_s}$	$\frac{R_p}{1+i\omega C_p R_p}$
$\lvert Z(\omega)\rvert$	$\frac{1}{\omega C_s}\sqrt{1+\omega^2 C_s{}^2 R_s{}^2}$	$\frac{R_p}{\sqrt{1+\omega^2 C_p{}^2 R_p{}^2}}$
$C^*(\omega)=\frac{1}{i\omega Z^*(\omega)}$	$\frac{C_s}{1+i\omega C_s R_s}$	$C_p - \frac{i}{\omega R_p}$
$\tan\delta$	$\omega C_s R_s$	$\frac{1}{\omega C_p R_p}$
τ	$C_s R_s$	$\frac{1}{\omega^2 C_p R_p}$

Table 3.2 compares the characteristics of these circuits for a given ω. If the same dielectric is represented in one case by the parallel circuit and in the other case by the series circuit, then:

$$\tan\delta = \frac{1}{\omega C_p R_p} = \omega C_s R_s \qquad (3.38)$$

while the values of the equivalent series and parallel components are related by

$$\frac{C_p}{C_s} = \frac{1}{1+\tan^2\delta} \qquad (3.39)$$

and

$$\frac{R_p}{R_s} = \frac{1+\tan^2\delta}{\tan^2\delta} \qquad (3.40)$$

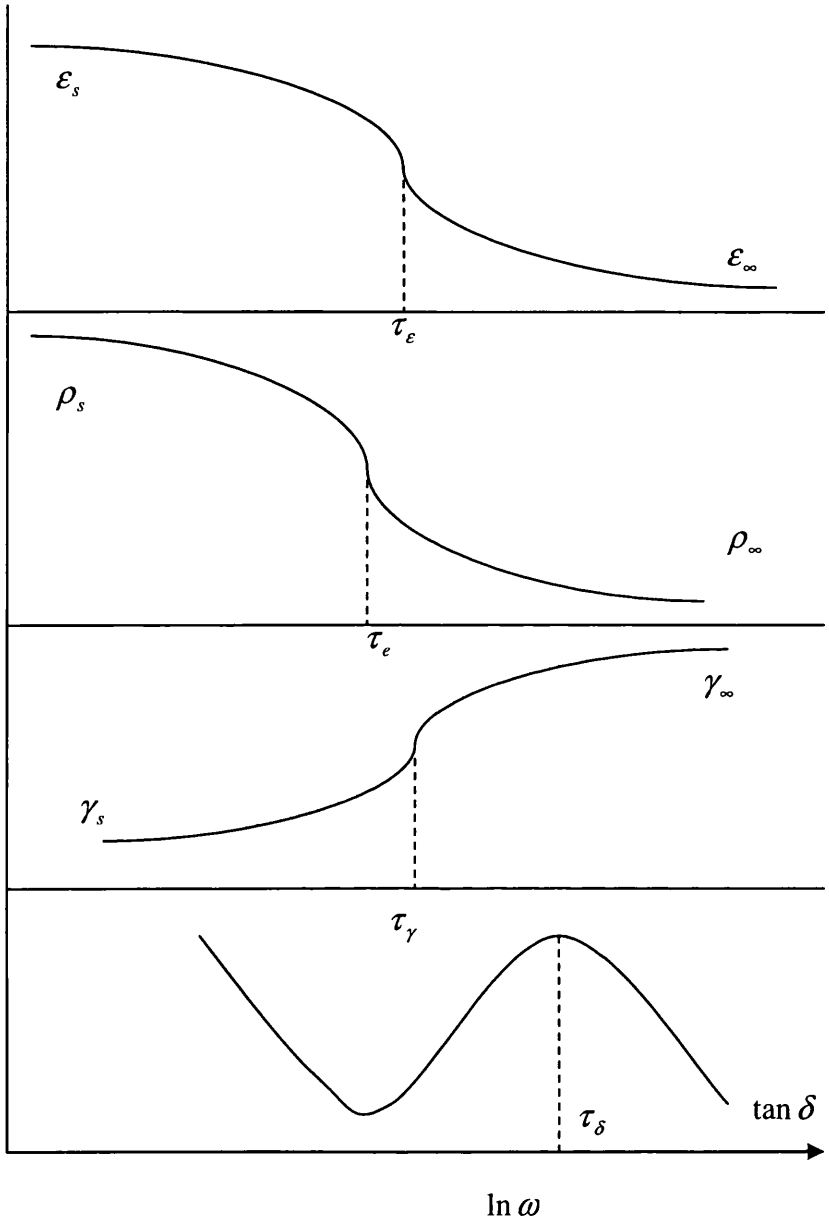

Figure 3.6 Examples of calculated curves give the dependence of permittivity (ε), conductivity (γ), resistivity (ρ), and dielectric loss ($\tan\delta$) on $\ln\omega$ in the one-layer dielectrics model.

In the parallel representation it is convenient to work with the resistivity of a material which is measured as the resistance between electrodes applied to opposite faces of a cube of unit edge. A capacitor of these dimensions has in the electrostatic system a capacitance C_0 equal $1/4\pi$ centimetres, so that equation (3.37) gives

$$\varepsilon^*(\omega) = \frac{1}{\varepsilon_0} C^*(\omega) \qquad (3.41)$$

or, in the parallel representation,

$$\varepsilon^*(\omega) = \frac{1}{\varepsilon_0}(C_p(\omega) - \frac{i}{\omega R_p(\omega)}) = \frac{1}{\varepsilon_0}(C_p(\omega) - \frac{i}{\omega}\gamma(\omega)) \qquad (3.42)$$

where $\gamma(\omega)$ is the conductivity, C_p is the capacitance, and $\varepsilon^*(\omega)$ is in e.s.u.

Frequency dependence of permittivity (ε), conductivity (γ), resistivity (ρ), and dielectric loss ($\tan\delta$) in the one-layer dielectrics model is shown in Figure 3.6. From the position of the curves along the frequency axis, the relevant dielectric relaxation times may be derived.

3.5.2 *Cross-section two-layer model*

Apart from the simple R-C circuits described above, the most useful equivalent circuits are that of the two-layer model. Figure 3.7 shows the electrode configuration of cross-section measurements of the two-layer model. The two-layer model represents two layers of dielectric of thicknesses d_1 and d_2, static dielectric constants ε_1 and ε_2, and direct conductivities γ_1 and γ_2.

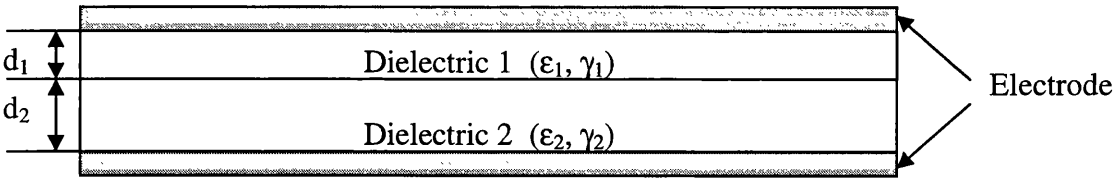

Figure 3.7 Electrode configuration of cross-section measurement of two-layer dielectrics model.

Volger [1960] evaluates the frequency dependent behaviour of this model in terms of the following formulae:

$$\varepsilon'(\omega) = \frac{\varepsilon_s + \varepsilon_\infty \tau_\varepsilon{}^2 \omega^2}{1 + \tau_\varepsilon{}^2 \omega^2} \tag{3.43}$$

$$\gamma'(\omega) = \frac{\gamma_s + \gamma_\infty \tau_\gamma{}^2 \omega^2}{1 + \tau_\gamma{}^2 \omega^2} \tag{3.44}$$

$$\rho'(\omega) = \frac{\rho_s + \rho_\infty \tau_\rho{}^2 \omega^2}{1 + \tau_\rho{}^2 \omega^2} \tag{3.45}$$

$$\tan\delta = \frac{\gamma_\infty}{\varepsilon_0 \omega \varepsilon_\infty} \frac{(\frac{\varepsilon_\infty \gamma_s}{\varepsilon_s \gamma_\infty}) + \tau_\delta{}^2 \omega^2}{1 + \tau_\delta{}^2 \omega^2} \tag{3.46}$$

with

$$\tau_\varepsilon = \tau_\gamma = \varepsilon_0 \frac{\varepsilon_s - \varepsilon_\infty}{\gamma_\infty - \gamma_s} = \varepsilon_0 \frac{\varepsilon_1 d_2 + \varepsilon_2 d_1}{\gamma_1 d_2 + \gamma_2 d_1} \tag{3.47}$$

$$\tau_\rho = \left(\frac{\gamma_\infty}{\gamma_s}\right)^{1/2} \cdot \tau_\varepsilon \tag{3.48}$$

$$\tau_\delta = \left(\frac{\varepsilon_\infty}{\varepsilon_s}\right)^{1/2} \cdot \tau_\varepsilon \tag{3.49}$$

$$\varepsilon_s = \frac{(d_1 + d_2)}{(\frac{d_1}{\gamma_1} + \frac{d_2}{\gamma_2})^2} \cdot \left(\frac{d_1 \varepsilon_1}{\gamma_1{}^2} + \frac{d_2 \varepsilon_2}{\gamma_2{}^2}\right) \tag{3.50}$$

$$\varepsilon_\infty = \frac{d_1 + d_2}{\frac{d_1}{\varepsilon_1} + \frac{d_2}{\varepsilon_2}} \tag{3.51}$$

$$\gamma_s = \frac{d_1 + d_2}{\frac{d_1}{\gamma_1} + \frac{d_2}{\gamma_2}} \tag{3.52}$$

$$\gamma_\infty = \frac{(d_1 + d_2)}{(\frac{d_1}{\varepsilon_1} + \frac{d_2}{\varepsilon_2})^2} \cdot \left(\frac{d_1 \gamma_1}{\varepsilon_1{}^2} + \frac{d_2 \gamma_2}{\varepsilon_2{}^2}\right) \tag{3.53}$$

Equations (3.50) to (3.53) give the static and high frequency values for the composite dielectric, while the meaning of the three relaxation times is clearly shown.

3.5.3 *In-plane two-layer model*

Figure 3.8 illustrates the electrode configuration of in-plane measurement of the two-layer dielectrics model. Formulae for the in-plane capacitance of the two-layer structure are shown below:

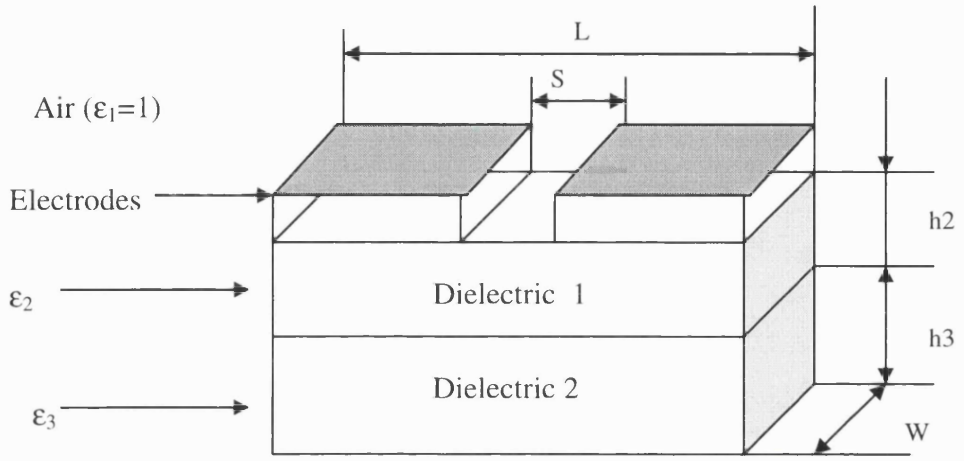

Figure 3.8 Electrode configuration of in-plane measurement of two-layer dielectrics model.

The total capacitance of the multi-layer capacitor is calculated as the sum of partial capacitances

$$C = C_1 + C_2 + C_3 \tag{3.54}$$

where C_1, C_2 and C_3 are the capacitances of air, dielectric 1 and dielectric 2, respectively [Vendik et al 1999 and 2000]. More complicated formulae corresponding to n parallel circuits have been given by Volger (1960).

$$C_1 = w\varepsilon_0 \frac{2}{\pi} \ln(\frac{4L}{S}) \tag{3.55}$$

$$C_2 = \frac{w\varepsilon_0(\varepsilon_2 - \varepsilon_3)}{s/h2 + (4/\pi)\ln 2} \tag{3.56}$$

$$C_3 = w\varepsilon_0(\varepsilon_3 - 1)\frac{1}{\pi}\ln(16\frac{h2+h3}{\pi s}) \tag{3.57}$$

3.6 Polarization Mechanisms

The dielectric properties can vary widely between solids. They are a function of temperature, frequency of applied field, humidity, crystal structure and other external factors. High-purity intrinsic diamond will not conduct electricity and as such is of critical importance as a capacitive element in electronic applications and as an insulator. In contrast to electrical conductivity, which involves long-range motion of charge carriers, the dielectric response results from the short-range motion of carriers under the influence of an external applied electric field. An application of an electric field to any solid will result in a separation of its positive and negative charges. This process of separation of charges is called polarization, which is defined as the finite displacement of bound charges of a dielectric in response to an applied electric field, and the orientation of their molecular dipoles if the latter exist. This section represents the most important polarization mechanisms from the microscopic point of view.

3.6.1 Electronic Polarization

Electronic polarization as shown in figure 3.9 occurs when the electron cloud is displaced relative to the nucleus it is surrounding. It is operative at most frequencies and drops off only at very high frequencies ($\approx 10^{15}$ Hz). Since all solids consist of a nucleus surrounded by electrons, electronic polarization occurs in all solids, liquids, and gases. Furthermore, since it does not involve hopping of ions or atoms between crystal lattice, it is insensitive to temperature. Electronic polarization exhibits a resonance when the frequency of the applied field is comparable to the natural frequency of vibration of the electronic cloud.

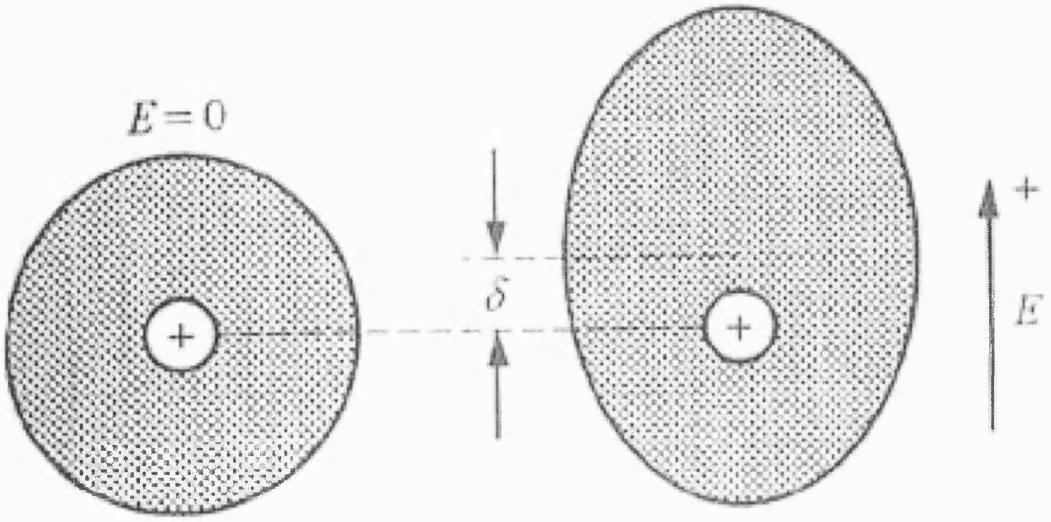

(a) (b)

Figure 3.9 Electronic polarization of the atomic cloud surrounding a nucleus. (a) At equilibrium in the absence of an external electric field, (b) In the presence of an external electric field [Hench and West 1989].

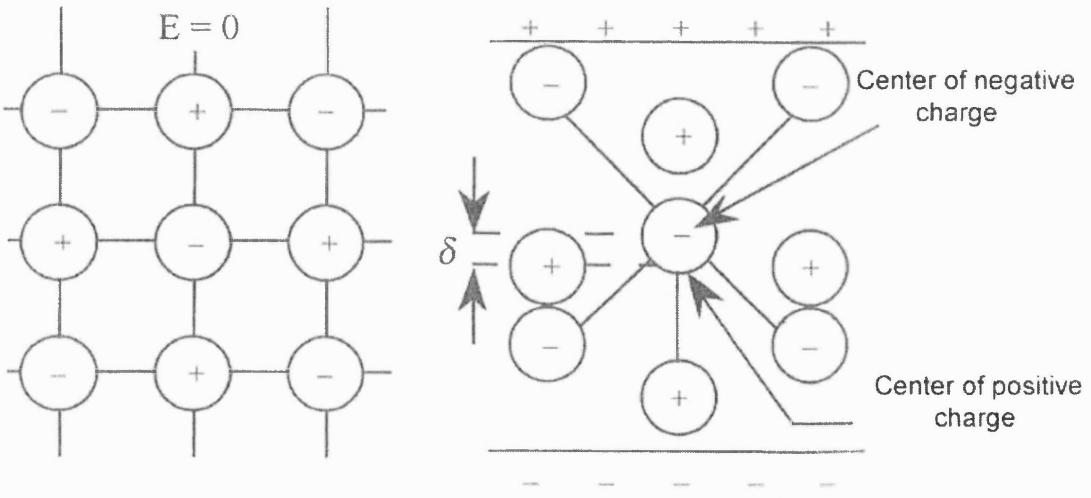

Figure 3.10 Ionic polarization (a) Ion positions at equilibrium: (b) Upon the application of an electric field, the centre of negative charge is no longer coincident with the centre of positive charge, i.e., polarization occurs [Hench and West 1989].

3.6.2 *Ionic Polarization*

Electron clouds are not the only species that can respond to an applied electric field. Ionic charges in a solid can respond equally well and can significantly contribute to the dielectric constant. Ionic polarization is defined as the displacement of positive and negative ions toward the negative and positive electrodes, respectively, as shown in Figure 3.10. Ionic resonance normally occurs in the infrared frequency range (10^{12}-10^{13} Hz).

3.6.3 *Dipolar Polarization*

In contrast to electronic polarization and ionic polarization, which occur at high frequencies (>10^{10} Hz), dipolar polarization occurs at lower frequencies (≈10^{9} Hz) and is thus important because it can greatly affect the capacitive and insulating properties of materials in low-frequency applications. Dipolar polarization is the preferential occupation of equivalent lattice sites as a result of the applied fields biasing one site over the other. The situation is depicted schematically in figure 3.11., where an ion is localized in a deep energy well, but within which two equivalent sites, labelled A and B in figure 3.11 (b), exist. The sites are separated from each other by a distance λ_s and an energy barrier ΔH_m. In the absence of an electric field as in figure 3.11 (a), each site has an equal probability of being occupied and there is no net polarization. However, in the presence of an electric field, the two sites are no longer equivalent, and then the electric field will bias the B sites, resulting in a net polarization.

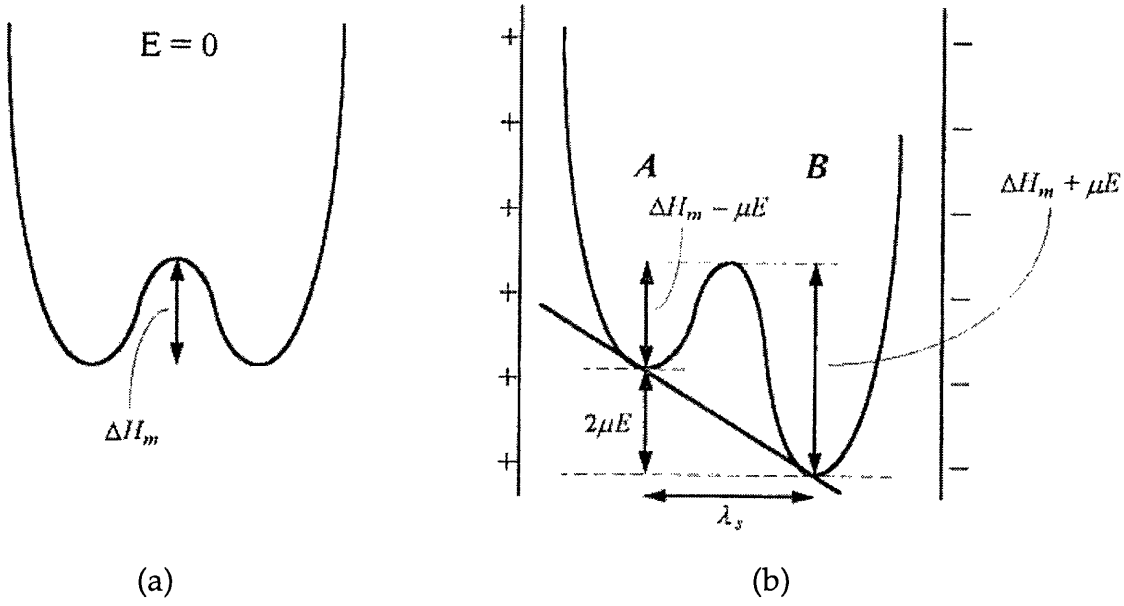

Figure 3.11 Dipolar polarization; (a) energy versus distance diagram in the absence of applied field; the two sites are equally populated. (b) The application of an external electrical field will bias one site relative to the other [Hench and West 1989].

3.6.4 Space Charge Polarization

When two dissimilar phases come into contact with each other, or the sample is coated with a certain electrode, an electrified interface may result. This so-called double layer acts as a capacitor with properties and responses different from those of the bulk material. The behaviour and interpretation of interfacial phenomena are quite complex.

From the above sections, it is clear that the dielectric response is a complex function of frequency, temperature, and type of solid. Under dc conditions, all mechanisms may operate. The dielectric constant is maximum and is given by the sum of the dielectric constant corresponding to each mechanism. However, under a.c. conditions, as the frequency increases, some mechanisms will be unable to follow the field variation and will therefore drop off, as shown in figure 3.12. At very high frequencies, none of the mechanisms

is capable of following the variation of the field, and the relative dielectric constant approaches 1.0. Temperature will strongly influence the polarization mechanisms that depend on long-range ionic displacement such as dipolar polarization. Ionic polarization is not strongly affected by temperature since long-range mobility of the ions is not required for it to be operative.

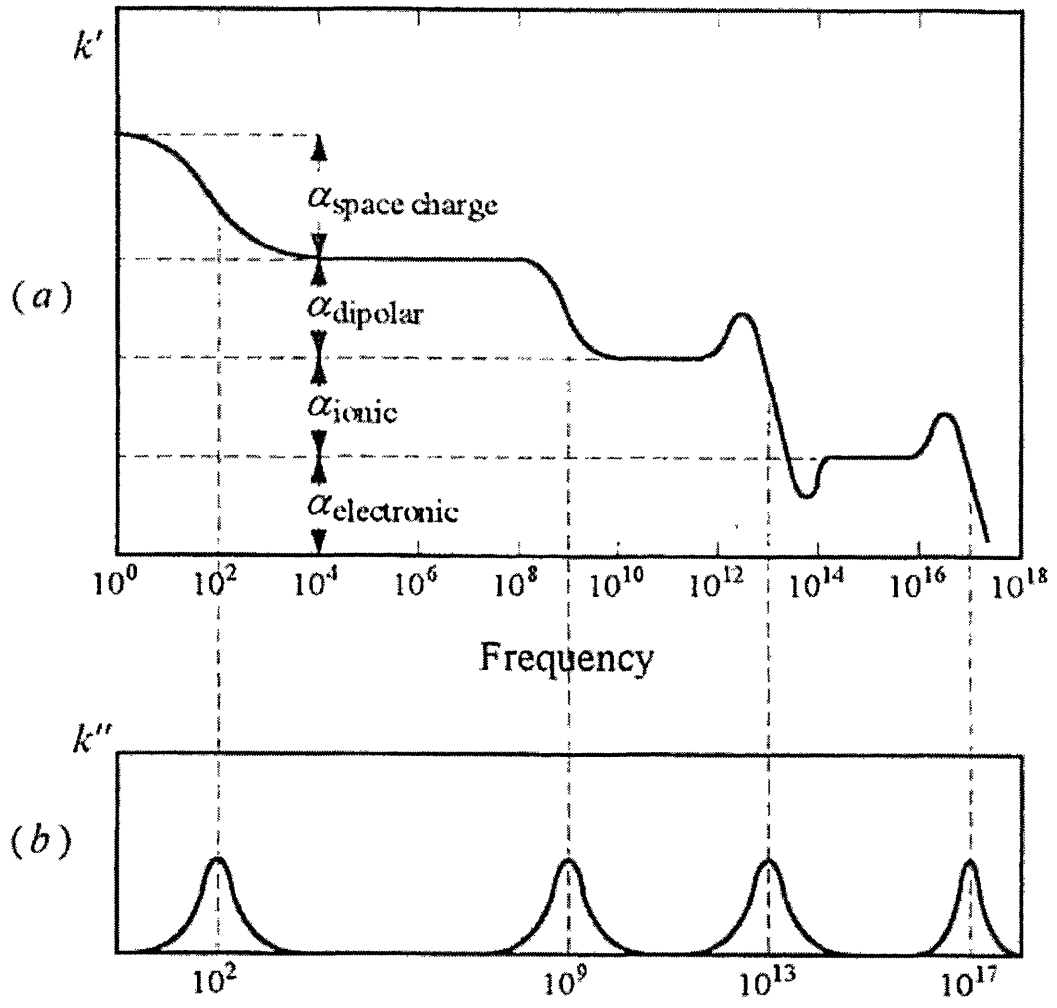

Figure 3.12 Frequency dependence of (a) relative dielectric constant and (b) dielectric loss [Hench and West 1989].

3.7 References

Aoki M, Chiang YM, Kosacki I, Lee LJ, Tuller J and Liu YP, J. Am. Ceram. Soc. **79** (1996) 1169.

Barsoum MW, Fundamentals of Ceramics, Institute of Physics Publishing Ltd, Bristol and Philadelphia (2003).

Bauerle JE, J. Phy. Chem. Solids **30** (1969) 2657.

Daniel Vera V, Dielectric Relaxation, Academic Press, London (1967).

Fleig J, Solid Status Ionics **131** (2000) 117.

Gabrielli C., Identification of Electrochemical Processes by Frequency Response Analysis, personal communications.

Garcia I, Olias JS, Rueda FA and Vazquez AJ, Diamond and Related Materials **6** (1997) 1210.

Godickemeier M, Michel B, Orliukas A, Bohac P, Sasaki K, Gauckler L, Heinrich H, Schwander P, Kostorz G, Hofmann H and Frei O, J. Mater. Res. **9** (1994) 1228.

Hench LL and West JK, Principles of Electronic Ceramics, Wiley, New York (1989).

Huanosta A, Alvarez-Fregoso O and Amano E, Journal of Applied Physics **69** (1991) 404.

Hodge IM, Ingram MD and West AR, J. Electroanal. Chem. **58** (1975) 429.

Khan N, PhD Thesis, University of London (1990).

Kumar MM and Ye ZG, Journal of Applied Physics **90** (2001) 934.

Macdonald JR, Impedance Spectroscopy, Wiley, New York (1987).

Maier J, Prog. Solid St. Chem. **23** (1995) 171.

M'Peko JC, Spavieri DL and de Souza MF, Appl. Phys. Lett. **81** (2002) 2827.

M'Peko JC, Appl. Phys. Lett. **77** (2000) 735.

Nistor LC, Landuyt JV, Ralchenko VG, Obraztsova ED and Smolin AA, Diamond and Related Materials **6** (1997) 159.

Tuller HL, Solid State Ionics **131** (2000) 143.

Van Dijk T and Burggraaf AJ, Phys. Status Solidi A **63** (1981) 229.

Vendik IB, Vendik OG, Deleniv AN, Kondratiev VV, Goubina MN and Kholodniak DV, IEEE Trans. On Microwave Theory and Tech. **48** (2000) 1247.

Vendik OG, Zubko SP and Nikolski MA, Technical Physics **44** (1999) 349.

Verkerk M, Middlehuis BJ and Burggraaf AJ, Solid State Ionics **6** (1982) 159.

Volger J, Prog. Semicond. **4** (1960) 209.

Yoder MN, in Diamond Films and Coatings, eds. David RF, Noyes Publications, New Jersey (1993) 13.

Chapter 4

Experimental and Characterization Techniques

4.1 Introduction

This chapter describes the main experimental and characterization techniques employed during the course of the research work reported in this thesis. Each technique reported here is introduced together with brief background information. The general principles are described and where appropriate schematics of simplified arrangements are given together with a discussion of the applications to the field of diamond electronics research; additional details of actual experimental set-ups are given in the experimental sections of the following chapters.

4.2 Microwave Plasma Enhanced CVD

The AsTex Microwave plasma enhanced chemical vapour deposition system (MPECVD) in the Electronic Engineering Department was used as the reactor for diamond growth. The MPECVD system was first demonstrated to grow polycrystalline diamond films on non-diamond substrates by a research group at Japan's NIRIM [Kamo et al 1983]. The Japanese were influenced by Soviet reports that atomic hydrogen was necessary to nucleate diamond films on non-diamond substrate [Spitsyn et al 1981]. Since previous work had indicated that microwave plasmas could dissociate diatomic molecules into atomic species, it was quickly adapted for diamond growth. In the microwave plasma, the high oscillating frequency of microwave (2.45 GHz) causes the fast oscillation of electrons and their collision with gas atoms. Thus, high fractions of gas excitation, dissociation and ionization are achieved. For the purpose of diamond deposition, microwave plasma excitation of H_2 generates super-saturation of atomic hydrogen whose role has been discussed in chapter 3.

A general MPECVD system consists of a gas mixing/admittance system, a microwave power generator/ delivery system, growth chamber, and pumping system. Typically deposition pressures are in the range of 10-80 Torr with a substrate temperature of 600-1000 °C. The substrates in MPECVD system are often immersed in the plasma, the so called "immersed mode",

which allows heating by both the plasma and microwave radiation. However, external substrate heaters are now commonly encountered, which allows the plasma and substrate parameters (such as microwave power and substrate temperature) to be effectively decoupled, facilitating parametric studies. With an external heater, the substrates can be placed outside of the luminous region of the plasma while still maintaining an appropriate growth temperature [Bachman et al 1988]. Diamond deposition has now been achieved with this "downstream mode" or more appropriate termed "remote plasma mode".

The schematic diagram of the microwave plasma enhanced CVD reactor system was shown in figure 4.1. The microwave chamber is constructed of a stainless steel base plate and a quartz bell jar. The output frequency is 2.45 GHz, and the maximum output power is 3 kW. The bottom plate was used to tune the chamber to obtain a plasma ball during growth. A substrate heater is inserted into the graphite holder to provide the desired temperature. Chamber pressure, as measured by a mercury manometer, can be adjusted by using an exhaust needle valve. A four channel mass flow controller is used to set the flow rates of all the reacting gases. Microwave power passes through a quartz window into a cylindrical cavity, which is the MPECVD process chamber. Location of the luminous plasma ball is controlled by cavity tuning as well as the pressure, power, and gas phase composition of the plasma. During each run, a plasma ball is made to form above the substrate holder by tuning the chamber height. The vertical position of the plate changes cavity tuning and affects the position and intensity of the luminous plasma ball. The luminous ball contracts in size as the chamber pressure increases and increases in diameter as the applied microwave power is increased. At that time, only the strongest center of the plasma ball is visible. The microwave plasma also generates intense ultraviolet radiation, which may affect diamond deposition.

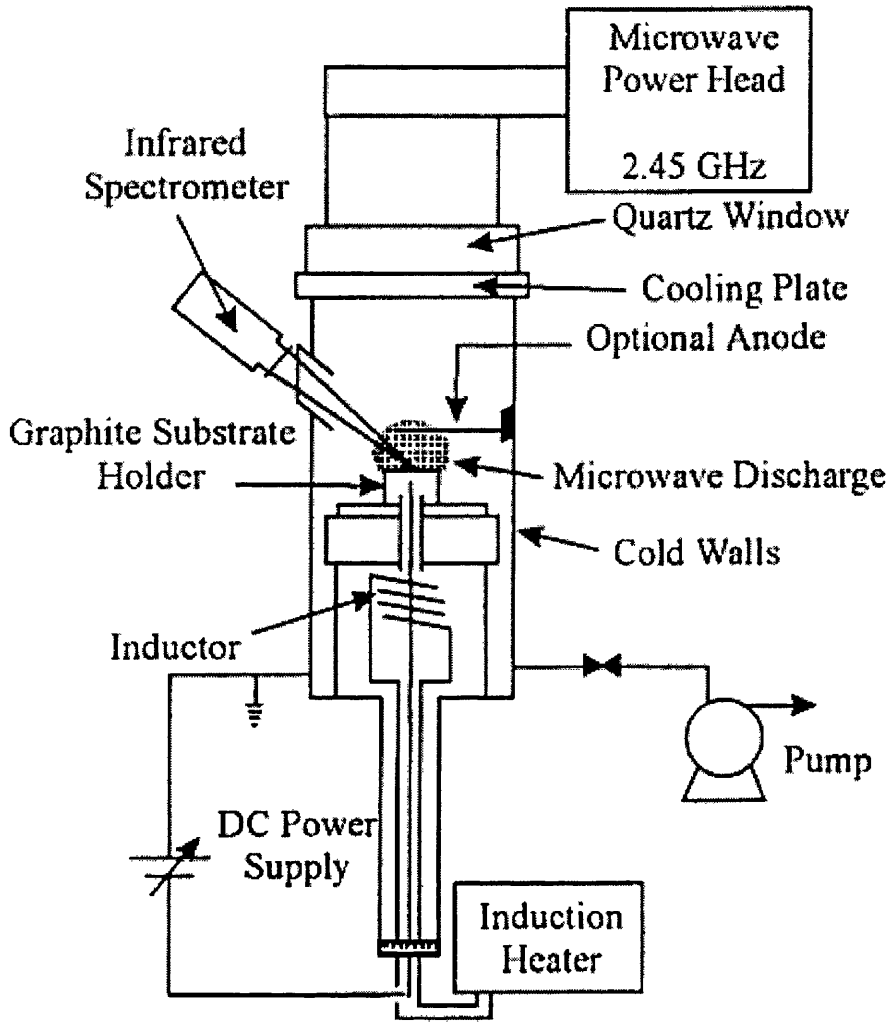

Figure 4.1 Microwave plasma enhanced chemical vapor deposition system.

4.3 Scanning Electron Microscope

Scanning electron microscope (SEM) located in the Institute of Archaeology at UCL is utilized for characterizing the diamond films' surface morphology throughout the project. This instrument is easier to use with the progress of electronics and introduction of new techniques. It is a technique available to examine thin film surfaces with sub-micron size features. It operates by scanning a focused electron beam over a surface and sensing the secondary electrons emission to determine the resolution and the brightness. Sample surface topography is magnified into an image on a cathode-ray tube.

SEM has many advantages over traditional microscopes, such as its high magnification (normally in the range of 50 - 40,000×), high resolution (10 nm), and the three dimensional appearance of images. In addition, the energy dispersive spectrometer (EDS) mode of operation can perform elemental identification and distribution. Although transmission electron microscopy (TEM) provides higher magnification (normally in the range of 8,000 - 300,000×) than SEM, the sample preparation is much more difficult than in SEM. The sample for TEM must be so thin that it is transparent to electrons, while for SEM, solid bulk samples can be used. A conducting material can be investigated without any preparation. Non-conducting material, such as diamond, need to be pre-coated with a thin layer of conducting material to avoid discharge. Gold and carbon are commonly used as conductive coatings.

4.4 Raman Spectroscopy

Raman Spectroscopy located in the Department of Chemistry at UCL was used to characterize the quality of the films investigated. The principle of Raman spectroscopy is simple. When a beam of monochromatic visible light passes through a crystal, some scattered light is produced with wavelength that is different from that of the incident light. The Raman effect is the shift in the frequency of light scattered from a crystal. The Raman spectrum is the plot of intensity of scattered radiation as a function of the shift between the incident and scattered light. The Raman spectrum is a sensitive indicator of film structural perfection. For the incident light source, a He-Ne (or Ar) ion laser is commonly used. Although X-ray diffraction can identify the crystal phases, it is not sensitive to small amounts of amorphous components within the film. These defects or impurities can drastically affect the thermal and electrical properties of the film. Natural diamond has a characteristic peak located between 1331 to 1336 cm^{-1}, with a bandwidth at half intensity, $\Delta v_{1/2}$, ranging from 1.8 to 3 cm^{-1}. Most reported Raman spectra of CVD diamond films contain a sharp peak between 1332 - 1345 cm^{-1} depending on the order within the

material. The higher this frequency, the greater the distortion from the cubic structure presented in the diamond. A broad band located at 1400-1600 cm^{-1} is often shown in the Raman spectrum of CVD diamond films. Some studies show that the Raman scattering efficiency of crystalline diamond is $4.9\text{-}6.0\times10^{-7}$ cm^{-1} and that of crystalline graphite is $3.0\text{-}4.3 \times 10^{-9}$ cm^{-1}. That is, the Raman scattering efficiency for the sp^2-bonded graphite is more than 100 times greater than that for the sp^3-bonded diamond. Therefore, the presence of the broad band around 1540 cm^{-1} indicates very small quantities of the non-diamond components in the deposited films.

It is well known that the Raman peak is shifted to higher frequency when diamond coating is subjected to compressive stress. The internal stresses in diamond coating can be estimated from the quantity of the diamond Raman line shift, $\Delta\nu$, with the following expressions [Nakamura et al 1997]:

$$\sigma = -2.63 \times 10^{10} \Delta\nu \qquad \text{for (100)} \qquad (4.1)$$

$$\sigma = -1.00 \times 10^{10} \Delta\nu \qquad \text{for (111)} \qquad (4.2)$$

For diamond coating with combination of (100) and (111), by assuming that the ratio of the (100) surface to the (111) surface to be equal in the study, the stress can be obtained by the following equation:

$$\sigma = -1.815 \times 10^{10} \Delta\nu \qquad \text{for combination of (100) and (111)} \qquad (4.3)$$

4.5 X-ray Diffraction

X-ray diffraction (XRD) located in the Department of Physics at UCL is a useful analytical technique to determine the structure and orientation of diamond crystals. In XRD, a fine beam of X-rays (copper $K\alpha$ with wavelength λ = 1.5418 Å) is passed through or reflected from a crystal and gives rise to reversal scattered beams which leave the crystal at various angles. The interference of X-rays scattering from atomic planes of a crystal can be

described by Bragg's equation, $n\lambda=2d\sin(\theta)$, where n relates the order of reflection, λ is the wavelength of the radiation, d is the crystallographic plane spacing, and θ is the diffraction angle. From the peak shown on the XRD pattern, we know the diffraction angle θ, which is used in Bragg's equation to find the d spacing of the crystallographic plane. If the Miller indices {h k l} are known, it is easy to determine the crystal lattice parameter for a cube lattice by using the equation $a = d \times (h^2 + k^2 + L^2)^{1/2}$. The calculated 'a' value for our diamond films is about 3.56 Å.

Grazing Incidence X-ray Diffraction (GIXRD) measurements were carried out using a Philips parallel beam horizontal diffractometer attached to a thin -film system and a Cu-Kα 40KV/30 mA (λ=1.5406 A) radiation beam with a minimal divergence value of 0.03°. By increasing the incidence angle from the critical value of total reflection, 0.25° to a high value of 9°, one can probe the layers of increasing thickness and determine their crystallographic structure by diffracted intensity detection. In this study, GISRD was used to determine the in-depth nature and distribution of different intermediate phases from the diamond film to the titanium substrate.

4.6 Surface Cleaning

The surface cleaning process was developed at UCL in 1994 arising from the UCL/Centronic Ltd Photodetector Project. The initial purpose of the process is to remove any other non-diamond carbon (such as DLC, and graphite) from the surface of the diamond as a barrier to device fabrication. This treatment consists of two processes: (1) a degrease and (2) an acid bath. The material is subjected to a degrease, then an acid bath and another degrease. Both processes are to be carried out in a fume cupboard, with particular attention during the acid bath.

Degrease solvents: 1,1,1-trichloroethane
Acetone
2-propanol (isopropanol, IPA)
De-ionized water (DI)

Degrease procedures:

1) Heat sample in 1,1,1-trichloroethane at 60°C for 5 minutes – do not allow to boil.
2) Transfer sample to acetone at room temperature.
3) Transfer sample to 2-propanol at room temperature.
4) Transfer sample to de-ionized water at room temperature.
5) Blow dry with nitrogen.

When transferring samples between solvents it is important to prevent the solvent on the sample from drying out as residue which is insoluble in the following solvent may be left on the surface. The transferring procedures must be as quick as possible.

Acid bath solvents: Concentrated sulphuric acid (c-H_2SO_4)
Ammonium persulphate ($(NH_4)_2S_2O_8$)
Hydrogen peroxide (H_2O_2)
Ammonium hydroxide (NH_4OH)
De-ionized Water (DI)

Acid bath procedure:

1) Place 6 teaspons of ammonium persulphate in a beaker. Carefully add 30 ml of concentrated sulphuric acid. This will give the ETCH solution.
2) Prepare the RINSE solution consisting of a 1:1 mixture of hydrogen peroxide (10ml) and ammonium hydroxide (10ml).
3) Heat the ETCH solution and add the diamond samples when the

temperature is about 85°C. It may fizz slightly.

4) Continue heating. Above 140°C fumes of SO_3 will be released.
5) Maintain the temperature of the solution at about 200°C for 20 minutes.
6) Allow the solution to cool to about 50°C before carefully transferring the sample from the ETCH solution to the RINSE solution. Pay attention, as there will be some heavy fizzing as the acid is neutralized.
7) Heat the RINSE solution and sample to about 50°C for 10 minutes.
8) Dispose of the ETCH solution by infinite dilution in running water.
9) Transfer sample from the RINSE solution to de-ionized water.
10) Dispose of the RINSE solution by infinite dilution in running water.
11) Remove sample from DI water and blow dry with nitrogen.

The development work of this procedure at UCL included an Auger electron spectroscopy study of various reported treatments [Baral et al 1996], based on a selection of literature [Fang et al 1989, Grot et al 1990, Gildenblat et al 1991, Mori et al 1991, Das et al 1992]. It was concluded that exposing CVD polycrystalline diamond to hydrogen plasma at the termination of the growth run or the use of strongly oxidizing solutions are both capable of removing non-diamond carbon from the surface, but high fluence excimer laser irradiation has the opposite effect. Both the oxidizing solutions considered gave rise to low concentrations of sulphur within the surface region and produced some form of oxide phase, but the sulphuric acid-ammonium persulphate etchant solution gave a carbon KVV Auger electron spectrum which more closely resembled single crystalline diamond. Hence this solution is used here.

4.7 Resistive Deposition of Metal Contacts

Metallization contacts can be deposited via a few techniques namely resistive evaporation, flash evaporation, sputtering and electron evaporation. Resistive evaporation will be described in details in this section as it is the main

method for depositing thin metal film for most of the experimental work in this thesis. This method is the oldest means for depositing thin metal films [Looi 1999]. Evaporation is conducted by passing a current through a high resistance wire, filament or boat. The heat generated by the resistive element is used to melt and vaporize the metal required. The high resistive element is normally made from refractory metals such as tungsten and molybdenum which have very high melting points of 3380°C and 2610°C at atmospheric pressure. It is preferable that the metal sublimes, as this avoids interaction of the metal liquid phase with the filament or heating elements. Some metals (for example: Titanium) form alloys with tungsten at high temperature and this normally leads to the destruction of the filament during evaporation. A high vacuum ($<10^{-6}$ mbar) is necessary to minimize the contamination, prevent the rapid oxidation of the metallic vapour and lower the vaporization temperature. Aluminium, gold, silver, tin, nickel and chromium can be easily deposited in this method. The key advantage of vacuum evaporation is the very high deposition rate achievable so that thick metal films (500nm) can be formed. This method, however, requires line of sight from the source to the target, as a result complex and irregular shape samples may not be uniformly coated.

The resistive evaporation system used for deposition Gold film in this work is an Edwards 306. The base pressure during the evaporation is kept below 10^{-6}mbar. This pressure is achieved by a diffusion pump backed by a rotary pump. Liquid nitrogen cold trap is used in addition to removed unwanted contamination from the diffusion pump and to maintain low pressure during resistive heating itself. Evaporation for Gold is carried out using a molybdenum boat.

4.8 Electrode Preparations and Impedance Spectroscopy

Impedance measurement was conducted to study the dielectric and electric properties of diamond coatings, and hence to determine the quality of the diamond through the change of electric resistivity. One of the most

important steps before the impedance spectroscopy measurements were carried out is to prepare the electrodes for either cross-section or in-plane configurations. Electrodes are normally applied to the sample by painting, vacuum evaporation, or sputtering. Materials for electrodes are usually made of the precious metals silver, gold or platinum. Silver paints are widely used in this thesis for measurements at moderate temperatures (~600°C) and for films with large area. Vacuum evaporated gold electrodes are applied to films at temperatures (~500°C) with a very small area, which is difficult to handle by painting. Platinum painted electrodes are normally used for electronic ceramics at higher temperatures. They require a serious baking in the temperature range 600-1300°C.

Bulk properties such as conductivity are calculated using the length over area l/A of each sample; hence, where possible, samples should be cut so as to have two parallel faces and a well-defined cross section. Silver pastes were used for most of the cross-section measurements to investigate the bulk properties of diamond. Surface electrical conduction properties are characterized using in-plane Au electrode configuration at different shapes, such spaced dots or strips on the same surface layer. For distinguishing grain interior conduction from grain boundary, surface finish is not critical, as this only affects the electrode impedance [Armstrong et al 1973]. If the grain boundary and electrode impedance arcs partly overlap, the resolution can sometimes be improved by surface polishing.

Impedance properties of the films were determined using a Solartron 1260A electrochemical impedance kit together with 1296 Dielectric interface. The Dielectric interface can effectively increase the range of impedance which can be measured. The measurement was made in the frequency range from 0.1 Hz to 10 MHz. The set up parameters are 0.05V of AC amplitude, 1s integration time, and no delay time.

4.9 References

Bachmann PK, Drawl W, Knight D, Weimer R and Messier R, in Diamond and Diamond-like Synthesis, eds. Johnson GH, Badzian AR and Geis MW, MRS, Pittsburg, PA 1988.

Baral B, Chan SSM and Jackman RB, J . Vac. Sci. Technol. **A 14** (1996) 2303.

Das K, Venkatesan V, Miyata K, Dreifus DL and Glass JT, Thin Solid Films **212** (1992) 19.

Fang F, Hewett CA, Fernandes MG and Lau SS, IEEE Transactions on Electron Devices **36** (1989) 1783.

Gildenblat GS, Grot SA and Badzian A, Proceedings of the IEEE **79** (1991) 647.

Grot SA, Gildenblat GS, Hatfield CW, Wronski CR, Badzian AR, Badzian T and Messier R, IEEE Electron Devices Letters **11** (1990) 100.

Kamo M, Sato Y, Matsumoto S and Setaka N, J. Cryst. Growth **62** (1983) 642.

Looi H. J., PhD thesis, University College London, 1999.

Mori Y, Kawarada H and Hiraki A, Appl. Phys. Lett. **58** (1991) 940.

Nakamura Y, Sakagami S and Amamoto Y, Measurement of internal stresses in CVD diamond film, Thin Solid Films **308-309** (1997) 249.

Spitsyn BV, Bouilov LL and Derjaguin BV, J. Cryst. Growth **52** (1981) 219.

Chapter 5

Boron Doped Single Crystalline Diamond

5.1 Introduction

The most effective method of modifying electronic properties of a material is through intentional doping. Boron is known to promote the formation of acceptor states giving rise to p-type conductivity in the diamond films [Mort et al 1989 and 1991, Nishimura et al 1991, Liu et al 1997]. The investigation of boron impurities as a deep acceptor (0.37eV ionization energy) has been extremely fruitful over the last 30 years. Collins et al [1970] determined the activation energy of the p-type behaviour in type IIb diamond based on the model containing both acceptors and donors levels. They measured a mean value of 0.368eV. Lightowlers et al [1976] utilised the I-V and C-V characteristic of a Au Schottky barrier to correlate quantitatively the active carriers in the diamond film to the boron concentration in the film. They concluded that the acceptors responsible were probably substitutional boron. Sandhu et al [1989] reported a sharp optical absorption at 2963 cm^{-1} (0.37eV) in diamond films co-implanted by carbon and boron. Masood et al [1992] reported a simple method of boron doping using a solid boron source and the dopant activation energies in the range of 0.30-0.38 eV.

Malta et al [1993] compared the electronic transport properties in boron-doped homoepitaxial, polycrystalline and natural single crystalline diamond using Hall-effect and resistivity measurements. They proposed that carrier trapping at grain boundaries result in charge build-up that impedes the motion of carriers from one crystallite to the next, thereby decreasing their mobility. If grain size and acceptor concentration are both sufficiently large, the grain boundaries will significantly degrade mobility but have a negligible effect on carrier concentration. The intragranular structural defects commonly exist as stacking faults, twins, and dislocations. They are not expected to dominate over the effect of grain boundaries, however, they may be still contributing to the degradation of mobility. Kalish et al [1994] concluded that graphitization along grain boundaries that one might have expected to happen due to boron implantation and following annealing, does not seem to affect the electrical

properties of the implantation-doped material. In the same year, Werner et al [1994] reported the charge transport in heavily B-doped polycrystalline diamond films. They found the decrease of the activation energy with increasing doping concentration can be explained in terms of impurity conduction. At sufficiently high doping concentrations the impurity band merges with the valence band and metallic conduction occurs. Won et al reported the crystalline quality and phase purity are much better for the boron-doped diamond than for the undoped diamond through cathodoluminescence spectrum. Boron incorporation eliminates the exciton-related emission [Won et al 1996]. Negative electron affinity has been observed in boron doped diamond using scanning filed emission spectroscopy by Wang et al [1996]. They described detailed spatial correlation between filed emission sites, and diamond morphology, surface work function, and diamond quality. Sternschulte et al [1997] observed the bound exciton spectrum and demonstrated the presence of isolated boron on substitutional lattice sites which implies electrical acceptor activity.

Liu et al [1997] reported a very small electron affinity of about 0.025 eV and a work function of 5.165eV for the boron-doped diamond (100) surface from frequency dependence capacitance–voltage spectroscopy measurements. They measured the boron acceptor concentration of ~$10^{17}cm^{-3}$ in diamond using capacitance spectroscopy. They argued that there might be several electronic processes in a material, each with its specific time constant, the time constant connected to the Schottky barrier may overlap with other time constants. It may not be possible to obtain doping concentration just from CV measurement at a single frequency and complex impedance measurement and analysis are necessary. A year after, from the same group Liu et al [1998] reported the activation energy of 0.36eV for boron doped diamond using the flatband capacitance method. Jaeger et al [1998] calculated the internal electrostatic potential distribution and resistivity of boron-doped diamond using a finite element analysis. They found the dominating conduction mechanism shifts from the valence-band conduction at intermediate temperature to the hopping

conduction at low temperatures. Chen et al [1999] correlated the electron field-emission properties of boron-doped diamond with secondary ion mass spectroscopy, infrared absorption and concluded that the solubility limit of boron in diamond is $(B^{+3})_s = 5\times10^{21}$ cm^{-3}, and the largest boron concentration that can be incorporated as substitutional dopants is only one tenth of the solubility limit, $(B^{+3})_d = 5\times10^{20}$ cm^{-3}. The diamond lattices are strongly strained when heavily doped. Krutko et al [2000] produced p-type polycrystalline diamond layers by rapid diffusion of boron. Gevrey et al [2001] used a contactless method to measure the conductivity of boron-doped diamond films at microwave frequencies, which has an advantage to avoid parasitic resistance or grain boundaries although the skin effect has to be considered. Lyman spectra in the infrared, electronic Raman scattering, and cathodoluminescence in the UV have revealed much of the complex electronic structure of this shallow acceptor [Nebel et al 2001]. Nebel et al detected the long living excited states in boron doped diamond in the energy regime 3.2-3.5 eV.

To date, only boron has clearly demonstrated and established itself conclusively to be an active electrically active dopant and a wide range of techniques have been applied to boron-doped diamond to investigate their electrical activation energy and defect levels. However, less work has been found to characterize boron doped diamond films using ac impedance spectroscopy to the best of the author's knowledge. Narducci and Cuomo [1990] investigated the boron diffusivity in diamond single crystals by impedance spectroscopy at a very early stage. They reported that diffusivity of boron in diamond at up to 800°C will not make the thermal drift of impurities a major path to device failure. However, their impedance measurement was only up to 10^5 Hz without temperature dependence, the results presented still did not give full understanding of responsible mechanism behind. Impedance spectroscopy has been widely utilized to study the conduction paths within a range of conducting and less-conducting materials, but its application to diamond films is relatively new [Macdonald 1987, Ye et al 2001 and 2002]. This technique allows the contributions to the overall conductivity from the grains,

grain boundaries and electrodes to be isolated. Thus it can be used as a powerful tool for researching methods to reduce problems within diamond technology that are associated with grain boundaries and poor metallic contacts. In this chapter, initial attention has been paid on boron-doped single crystalline diamond films. This type of diamond has a moderate resistance value and thus is most suitable for impedance measurement. This chapter will build-up more understanding on the boron-doped diamond and will provide evidence that the impedance spectroscopy is a feasible and useful tool in characterising the electrical and dielectric properties of diamond films.

5.2 Experimental Details

Boron-doped single crystalline CVD diamond films grown on Ib substrates were used throughout (CNRS Laboratories, Grenoble, France). The growth process used has been described in details elsewhere [Gheeraert et al 2002]. Titanium and gold electrodes were formed on the surface of its square corners to form a metal contact as shown in figure 5.1. Silver wires were used to bond the devices to the sample holder, which is placed in a vacuum chamber of 10^{-2} Torr.

Room temperature dc current-voltage measurements between two symmetric electrodes across the surface of the diamond films were carried out using HP4145B analyzer. Voltage is set from –10 V to 10 V. DC current-temperature measurements were investigated using Keithley 487 Picoammeter under rough vacuum from -185°C to 256°C. Voltage is set to 50 V as power supply. Impedance measurement of the films was determined using a solartron 1260A electrochemical impedance spectroscopy in the frequency range from 0.1 Hz to 10 MHz, and in the temperature range from -100°C to 300°C. The set up parameters are: 0.05 V of AC amplitude, 1s integration time, and no delay time. The activation energy of Boron doped diamond films can be obtained through both DC current and AC impedance measurements. The objective of this experiment is to see whether the data from both methods are consistent with

each other. If so, it will provide proof of validation and accuracy for AC impedance spectroscopy.

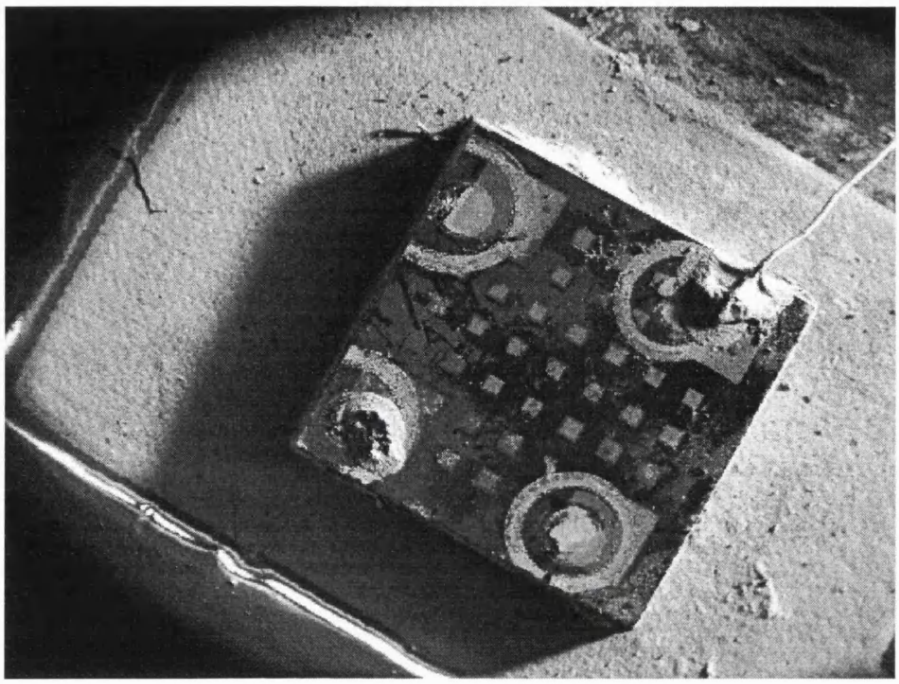

Figure 5.1 SEM photograph of Boron doped single crystalline diamond films with four electrodes (titanium/gold alloy) on the surface of its square corners to form an ohmic contact. Commercial silver wires are used to bond the device to the holder.

5.3 Experimental Results

Figure 5.2 shows room temperature dc current-voltage measurement on the surface of the diamond films in two electrode directions: (a) from up to down and (b) from left to right. Comparing the curves in both directions, figure 5.2 (b) measured from left electrode to right shows nearly a perfect ohmic contact, which has a symmetric and linear characteristic from the negative to positive voltage. It is easily estimated that the room temperature resistance is about 1.1 MΩ. To investigate the dc temperature effect in this electrode direction, the current-temperature (-185°C to 256°C) curves are shown in figure 5.3. It is found that the current increases exponentially with the temperature increasing, which indicates thermally activated conduction process. Linear curve fitting shows the sample has activation energy of 0.36 eV. The result is consistent with

most of the other people reported on boron-doped diamond [Collins et al 1970, Liu et al 1997].

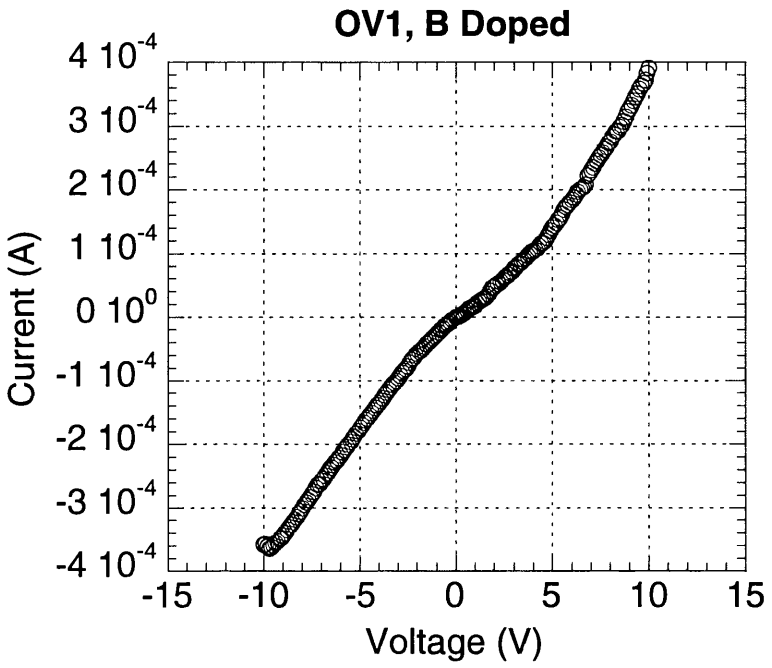

(a)

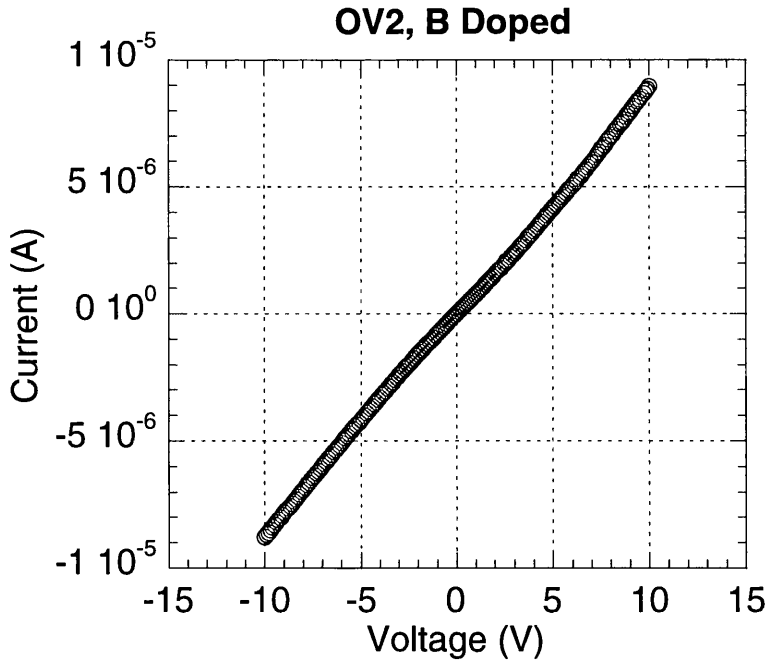

(b)

Figure 5.2 Room temperature Current-Voltage measurements between two symmetric electrodes across the surface of the diamond films.

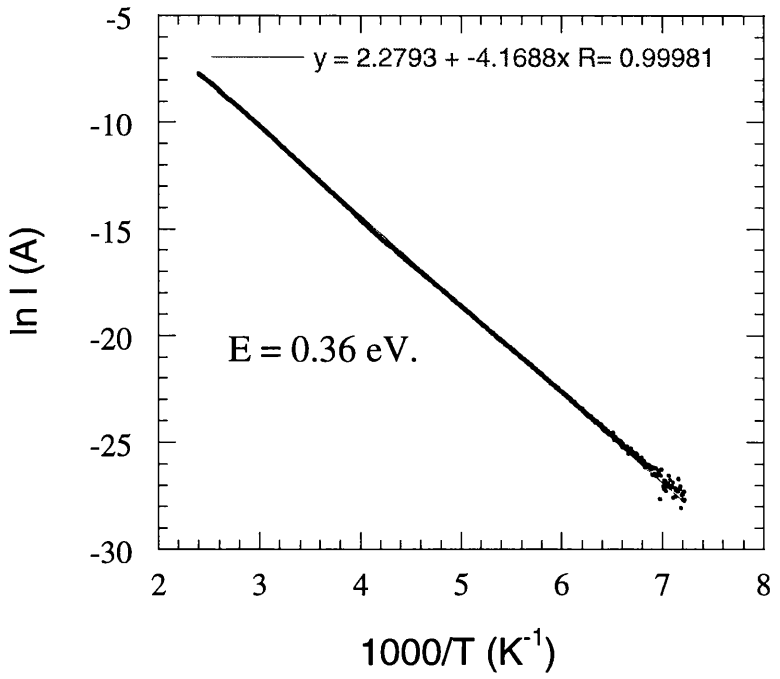

Figure 5.3 DC current – temperature measurement using TSC chamber from –185 to 256°C. Voltage is set to 50 V as power supply. Linear curve fitting from –134 to147°C shows the sample has a DC activation energy of 0.36 eV. OV1 is from up to down, and OV2 is from left to the right as shown in the Figure 5.1.

Simple dc electrical experiments have now been repeated to achieve the activation energy of boron doped diamond, 0.37eV, which is already well-known within diamond community for a number of years. For the first time, we applied impedance spectroscopy to the boron doped single crystalline diamond sample to compare the ac results with dc and to prove if this technique is valid on this type of film. The Cole-Cole plots of boron-doped single crystalline diamond films from -100°C to 300°C are shown in figure 5.4 (a)-(f). Figure 5.4 (a) presents the data measured at –100°C showing the presence of a single semicircular response, with some scatters at the low frequency impedance range (right end). Similar data are shown in figure 5.4 (b)–(f) for the temperature range from -50°C to 300°C. The diameter of the semicircles reduces dramatically with the temperature increasing. Above 100°C as shown in Figure 5.4 (e), the semicircular response at high frequencies cannot reach the origin.

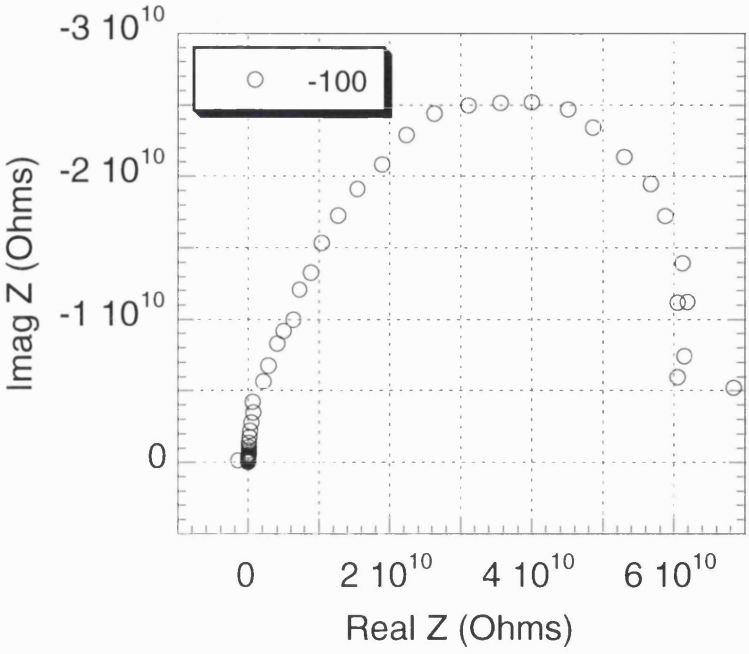

(a) -100°C

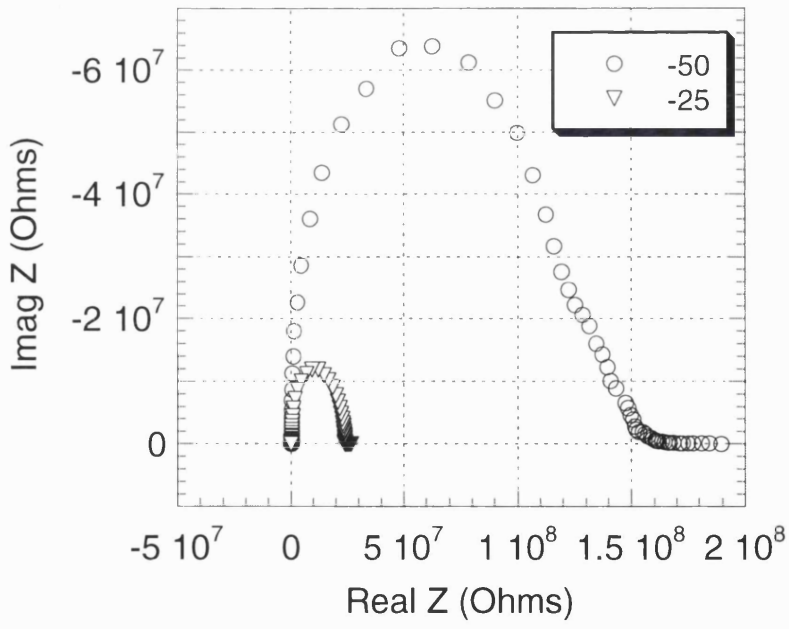

(b) -50 and -25°C

Continued on next page

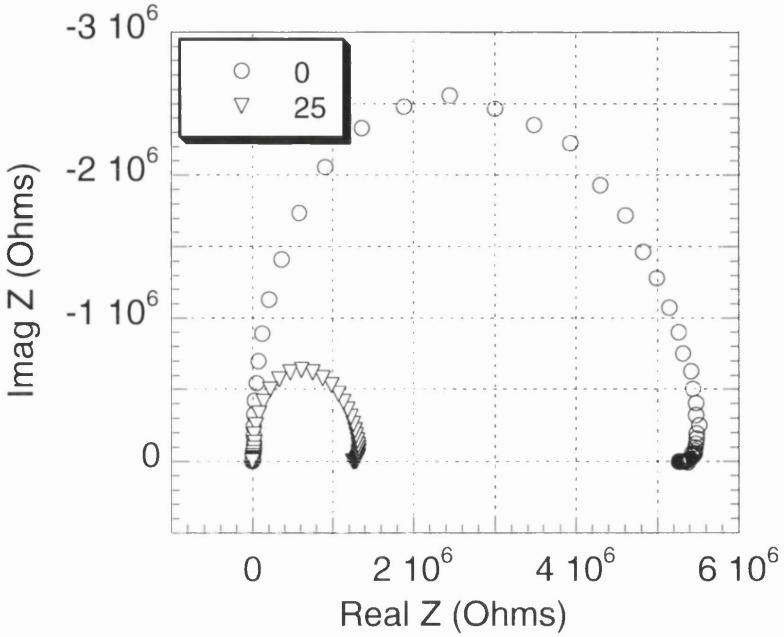

(c) 0 and 25°C

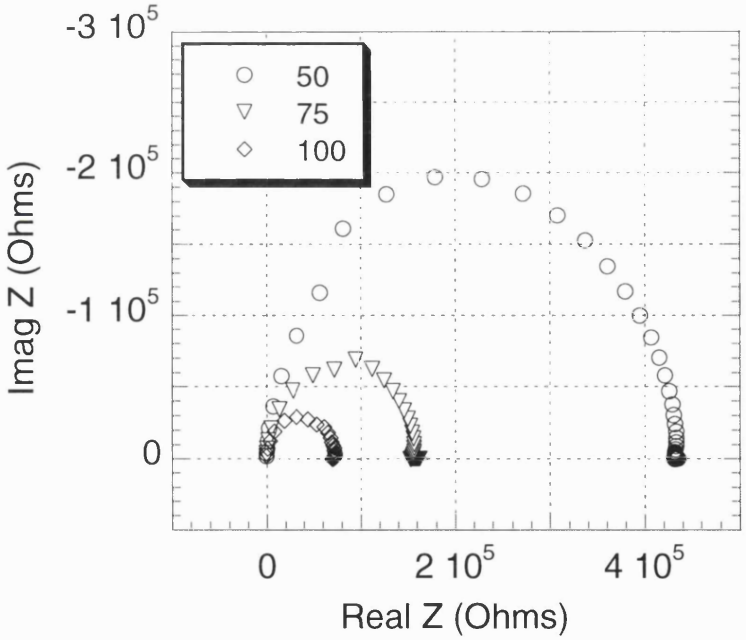

(d) 50 and 100°C

Continued on next page

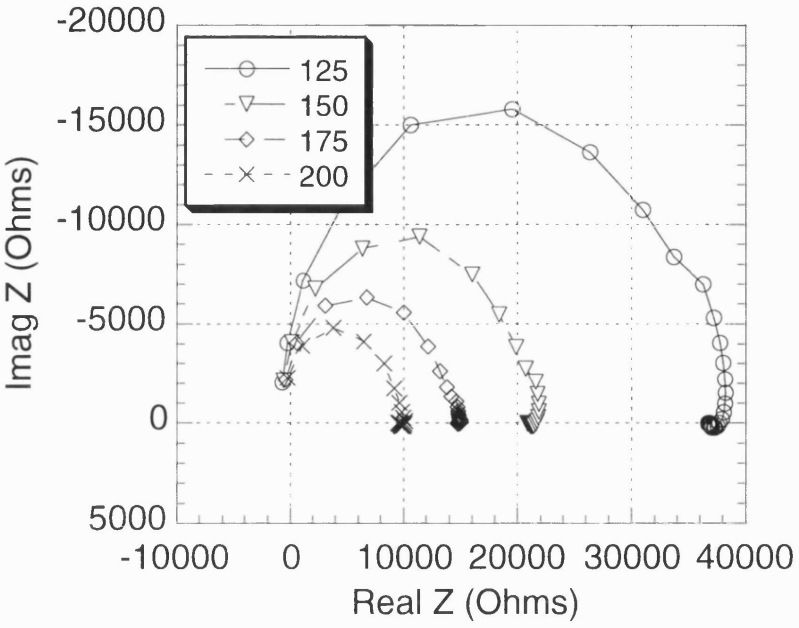

(e) 125 and 200°C

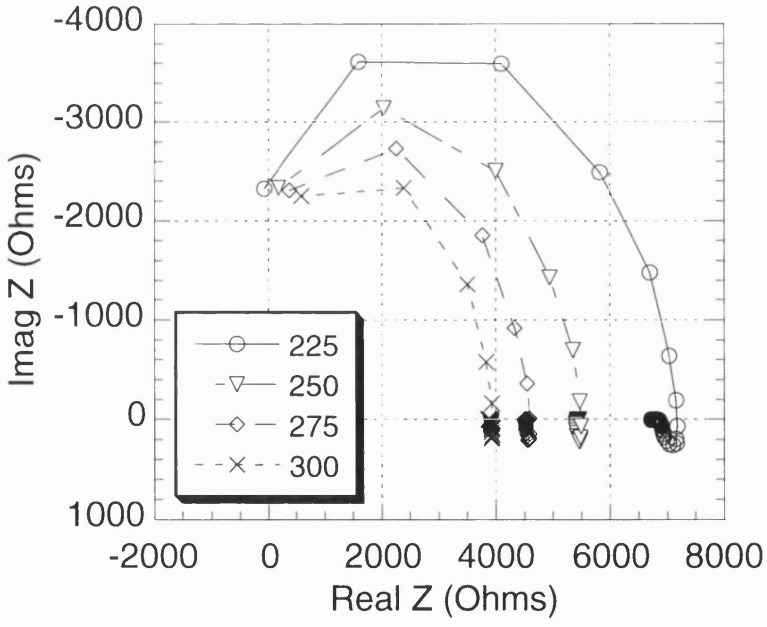

(f) 225 and 300°C

Figure 5.4 AC impedance measurements on boron-doped single crystalline diamond films, from 0.1 Hz to 10 MHz, vacuum pressure: 0.05 mbar, Ac amplitude: 0.1 Volt, from -100°C to 300 °C.

It is found that each Cole-Cole plot shows only one depressed semicircle. The single semicircle indicates that only one primary mechanism exists for the electrical conduction within the diamond film at temperatures below 300°C. The depressed semicircles make their centres on a line below the real axis, which indicates the departure from the ideal Debye behaviour [Macdonald, 1987]. The diameter of each semicircle indicates the electrical resistance of diamond films. With the increase of temperature, the diameter decreases indicating the reduction of the resistance from 70GΩ at –100°C to 5KΩ at 300°C.

5.4 Discussion

A central issue to be addressed is what portion of the equivalent circuit [see figure 3.2 in chapter 3] corresponds to the observed single semicircular response. This interpretation is centred to determine the dominance of impedance from grain interiors or grain boundaries or otherwise injection from the electrodes. For ionic conductors, electrode porosity and polarisation must be considered for the general impedance analysis [Bauerle, 1969]. Whilst for diamond, different electrode configuration effects have been investigated and the results show no significant variation in impedance spectroscopy due to its large resistance discrimination between diamond and electrode. Therefore, the impedance contribution from the electrodes could be ignored in diamond-based high resistive materials.

Critical to the identification of the grain boundary and grain interior contribution is the simulated capacitance value for each semicircle. It has already been established in literature that, the lower frequency dispersion corresponds to the grain boundaries and the higher frequency dispersion corresponds to the grain bulk interior if two semicircles appear, which normally have a capacitance value in the range of nF and pF, respectively [Huanosta et al 1991, Ye et al 2001, M'Peko et al 2002].

The parallel resistance, capacitance, and relaxation frequency in each semicircle has been simulated using Zview software supplied by Solartron Inc. The detailed values are shown in table 5.1. It is obvious that all the capacitance values is in the range of pF. This implies the single semicircular response is from grain interiors, which is expected from a single crystal diamond where no grain boundaries are being involved. Huang et al [1995] reported a very interesting result that boron atoms are desegregated at grain boundaries and are uniformly distributed inside each diamond grain by using Auger and SIMS techniques. Based on their observation, it was suggested that boron dopants make a significant contribution in the conduction path within grain interiors instead of grain boundaries either for polycrystalline diamond films or single crystalline.

Table 5.1 Impedance parameters of boron doped single crystalline diamond.

Temp (°C)	Resistance (Ω)	Capacitance (pF)
-100	7.03e10	1.370
-75	1.66e9	0.506
-50	1.22e8	0.503
-25	24200000	0.491
0	5560000	0.503
25	1360000	0.489
50	435000	0.544
75	161000	0.633
100	74726	0.890
125	39767	1.186
150	22839	1.620
175	16821	1.770
200	11447	2.250
225	8366	2.700
250	6566	3.100
275	5581	3.340
300	4836	3.450

The electrical resistance is plotted against temperature in an Arrhenius plot shown in figure 5.5. Linear curve fitting shows the sample has an activation energy of 0.37eV, which is possibly the data at low carrier concentrations [Nishimura et al 1991]. Comparing activation energy from ac impedance with the one from dc measurements (0.36eV), we can summarize that they are consistent with each other.

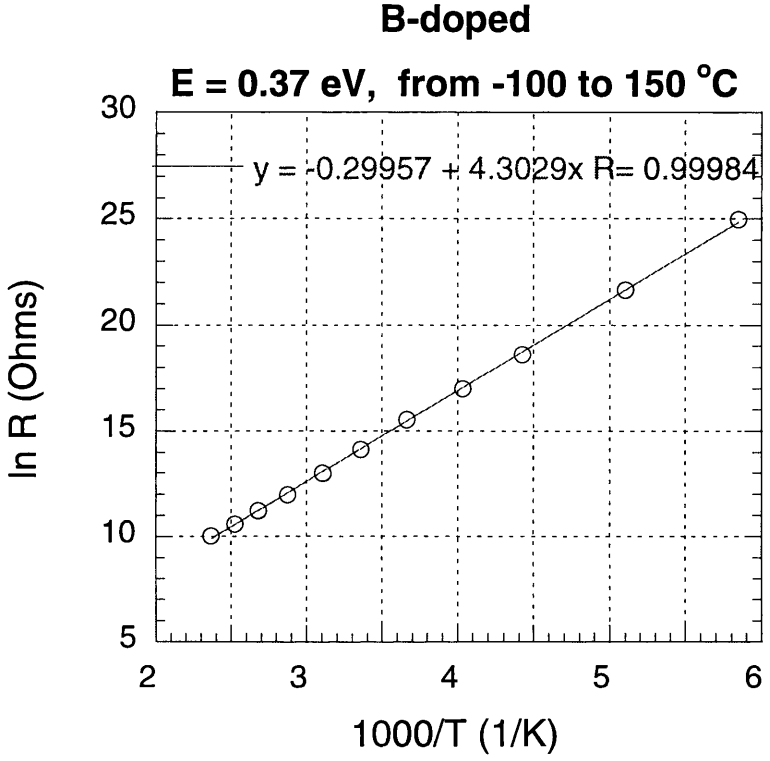

Figure 5.5. Temperature dependence of resistance from the impedance spectroscopy. Linear curve fitting from –100 to 150°C shows the sample has ac activation energy of 0.37 eV, which is consistent with the theoretical value published.

Impedance spectroscopy on boron doped single crystalline diamond has proved to be an effective way to provide electrical information on a microscopic basis. Another advantage is its low amplitude of source voltage, which offers a non-destructive method to characterize the system. Thus it could become an alternating approach to traditional electrical characterization techniques in many other semiconductor materials, correlating electrical with physical properties in both materials science and electronic engineering.

5.5 Conclusions

We report the first measurement of impedance on boron-doped single crystalline diamond films from 0.1Hz to 10MHz with the temperature ranging from –100°C up to 300°C. The equivalent Resistance and Capacitance for the diamond films are estimated from the Cole-Cole plots based on the RC parallel circuit model. It was found that the resistance decreases from 70GΩ at –100°C to 5KΩ at 300°C. The linear curve fitting from –100°C to 150°C shows the sample has an activation energy of 0.37eV, which is consistent with the theoretical value published of this kind of material. The equivalent capacitance is maintained at the level of pF up to 300°C suggesting that no grain boundaries are being involved, as expected from a single crystal diamond. The activation energy deduced from the dc current-temperature curves is 0.36 eV, which is consistent with the data from ac impedance. This chapter builds up more understanding on the boron-doped diamond and proves the impedance spectroscopy is a feasible and useful tool in characterising the electrical and dielectric properties for diamond films.

5.6 References

Bauerle JE, J. Phys. Chem. Solids **30** (1969) 3657.

Chen YH, Hu CT and Lin IN, Appl. Phys. Lett. **75** (1999) 2857.

Collins AT and Williams WS, Solid State Phys. **4** (1970) 1789.

Gevrey F, Gire A, Gaudiot D, Theobald JG, Gheeraert E, Bernard M and Torrealba-Anzola F, J. Appl. Phys. **90** (2001) 4251.

Huang JT, Hu CS, Hwang J, Chang H and Lee LJ, Appl. Phys. Lett. **67** (1995) 2382.

Huanosta A, Alvarez-Fregoso O, Amano E, Tabares-Munoz C, Mendoza-Alvarez ME and Mendoza-Alvarez JG, J. Appl. Phys. **69** (1991) 404.

Jaeger MD, Hyun S, Day AR, Thorpe MF and Golding **B72** (1998) 2445.

Kalish R, Uzan-Saguy C, Samoliloff A, Locher R and Koidl P, Appl. Phys. Lett. **64** (1994) 2532.

Krutko OB, Kosel PB, Wu RLC, Fries-Carr SJ, Heidger S and Weimer J, Appl. Phys. Lett. **76** (2000) 849.

Lightowers EC and Collins AT, J. Phys. D: Appl. Phys. **9** (1976) 951.

Liu K, Chu J, Johnson C and Roth S, J. Appl. Phys. **83** (1998) 4202.

Liu K, Zhang B, Wan M, Chu JH, Johnson C and Roth S, Appl. Phys. Lett. **70** (1997) 2891.

Liu K, Johnston C, Chu JH, Roth S, Zhang B and Wan M, J. Appl. Phys. **82** (1997) 286.

M'Peko JC, Spavieri DL and de Souza MF, Appl. Phys. Lett. **81** (2002) 2827.

Macdonald JR, Impedance Spectroscopy, Wiley, New York (1987).

Malta DM, von Windheim JA and Fox BA, Appl. Phys. Lett. **62** (1993) 2926.

Masood A, Aslam M, Tamor MA and Potter TJ, Appl. Phys. Lett. **61** (1992) 1832.

Mort J, Kuhman D, Machonkin M, Morgan M, Jansen F, Okumura K, LeGrice YM and Nemanich RJ, Appl. Phys. Lett. **55** (1989) 1121.

Mort J, Machonkin M and Okumura K, Appl. Phys. Lett. **58** (1991) 1908.

Narducci D and Cuomo JJ, J. Appl. Phys. **68** (1990) 1184.

Nebel CE, Rohrer E and Stutzmann M, J. Appl. Phys. **89** (2001) 2237.

Nishimura K, Das K and Glass JT, J. Appl. Phys. **69** (1991) 3142.

Sandhu GS, Swanson ML and Chu WK, Appl. Phys. Lett. **55** (1989) 1397.

Sternschulte H, Wahl S, Thonke K, Sauer R, Dalmer M, Ronning C and Hofsass H, Appl. Phys. Lett. **71** (1997) 2668.

Wang WN, Fox NA, Steeds JW, Lin SR and Butler JE, J. Appl. Phys. **80** (1996) 6809.

Werner M, Dorsch O, Baerwind HU, Obermeier E, Haase L, Seifert W,

Ringhandt A, Johnson C, Romani S, Bishop H and Chalker PR, Appl. Phys. Lett. **64** (1994) 595.

Won JH, Hatta A, Yagyu H, Jiang N, Mori Y, Ito T, Sasaki T and Hiraki A, Appl. Phys. Lett. **68** (1996) 2822.

Ye HT, Sun C, Huang H and Hing P, Appl. Phys. Lett. **78** (2001) 1826.

Ye HT, Sun C, Huang H and Hing P, Thin Solid Films **381** (2001) 52.

Ye HT, Williams OA, Jackman RB, Rudkin R and Atkinson A, phys. stat. sol.(a) **193** (2002) 462.

Chapter 6

Influence of Film Quality

6.1 Introduction

For many industrial applications such as cutting tools, optical components and microelectronic devices the control of film structure and morphology is of crucial importance. The crystallite size, orientation and surface roughness have a profound effect on the mechanical, electrical and optical properties of the films deposited. A few research papers on scanning electron microscopy (SEM) analysis of diamond films have related the morphological development to the deposition parameters. Moreover, the polycrystalline morphology has been related to Raman spectroscopy and X-ray diffraction measurements. An excellent review has been given by Zhu et al [1991]. A morphology field map has been presented [Zhu et al 1990] which depicts different zones of surface texture of diamond films as a function of methane concentration in hydrogen and substrate temperature. Tang et al [2003] reported the film of best quality has very smooth crystalline facets free of second nucleation and the full width at half maximum (FWHM) of the diamond Raman peak is 2.2 cm^{-1}, as narrow as that of IIa natural diamond. Larson and Girshick [2003] concluded increasing substrate temperature causes the film morphology to shift from {100} towards {111} faceting.

Although a number of different chemical vapour deposition (CVD) techniques have been developed to deposit diamond films, the study of the factors controlling the morphology, quality and related properties of the deposited films is far from complete [Yarbrough and Messier 1990, Pickarczyk and Yarbrough 1991]. Among the multitude of diamond CVD processes which have been developed for about 20 years, the microwave plasma enhanced CVD process (MPECVD), together with the hot-filament CVD method (HFCVD), has continued to be one of the most used diamond deposition processes. This chapter compares the impedance properties of films deposited using both MPECVD and HFCVD methods.

6.2 Experimental Details

Free-standing diamond films grown by microwave plasma enhanced CVD and hot-filament CVD were used to investigate the influence of the film quality on the impedance spectrum. Au electrodes (diameter 2mm, thickness 300nm) were evaporated to form an ohmic contact to both the front and the back side of the film to investigate the cross-section electrical conduction. Before Au evaporation, the diamond films were acid bath cleaned to remove any non-diamond phases [Baral et al 1996]. The electroded samples were dried in air at 400°C for 2 minutes to ensure thermal stability of the electrodes.

The film quality was evaluated using Raman spectroscopy with the 514 nm line of an argon ion laser. The residual stresses in the diamond films could be estimated from the shifting of the typical diamond peak. The surface morphology of the films was investigated using an environmental scanning electron microscopy (in which no conductive layer is needed to reduce the charging effect before observations were carried out) attached to an energy dispersive X-ray spectroscopy. The impedance of the films was determined using a Solartron 1260A impedance spectroscopy (IS) system in the frequency range from 0.1 Hz to 10 MHz up to 300°C. The set up parameters are: 0.05 Volt of Ac amplitude, 1 second integration time, and no delay time.

6.3 Experimental Results

6.3.1 Characterization of Film Quality

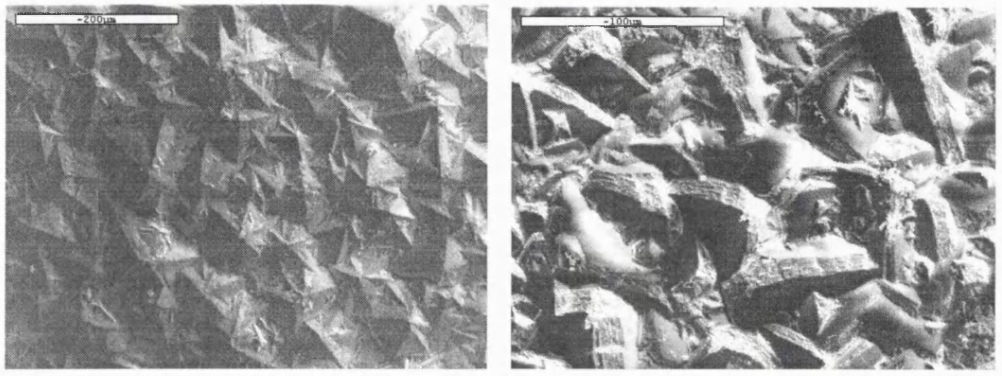

(a) MPECVD diamond (b) HFCVD diamond

Figure 6.1 SEM photographs of MPECVD diamond film and HFCVD diamond film.

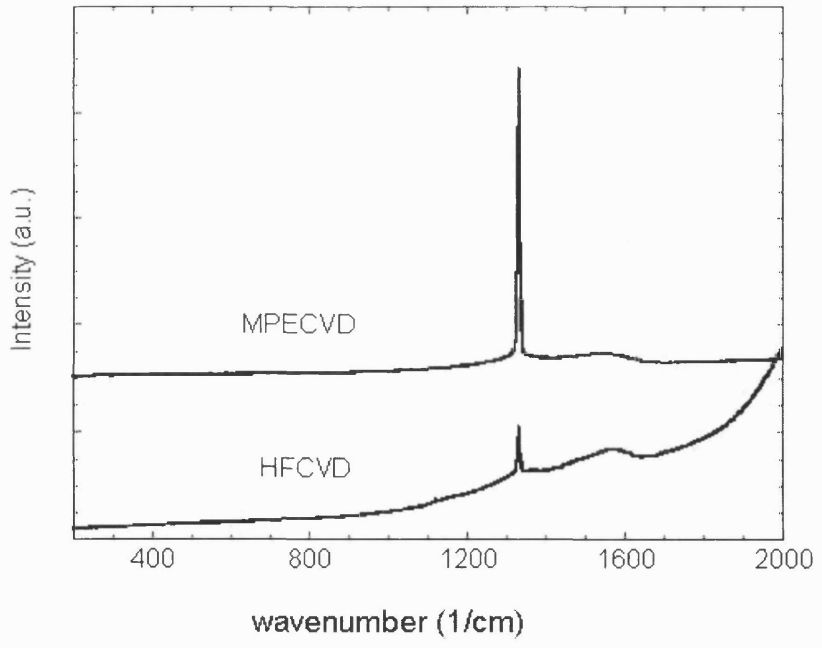

Figure 6.2 Raman spectroscopy of MPECVD and HFCVD diamond films.

SEM photographs of investigated films are shown in figure 6.1. MPECVD diamond film shows a well-faceted and polycrystalline morphology with (111) triangle crystal orientation dominating. However, HFCVD diamond shows a rather rougher surface than MPECVD with the merging surface of different crystal orientations. Rounded and layered morphology were also observed for HFCVD diamond. The corresponding Raman spectra are shown in figure 6.2. MPECVD diamond has a sharp peak at 1331 cm^{-1}, which is characteristic of high purity diamond and a tiny shoulder at around 1580 cm^{-1}, which is the signal of graphite phases embedded in this sample. The HFCVD film shows a typical diamond peak at 1331 cm^{-1} as well, but the intensity of this peak is much lower in the HFCVD diamond than in the MPECVD diamond. Additionally, there is a broader shoulder at 1580 cm^{-1} which indicates the HFCVD diamond has more graphite and non-diamond phases formed during the CVD process.

6.3.2 Characterization of Electrical Behaviour

The Cole-Cole plots for MPECVD diamond films from 25 to 400°C are shown in figure 6.3. The Cole-Cole plot at room temperature shows the presence of a single semicircular response, with some scatters in the data of the low frequency range. Similar data are shown for the other temperature ranges. The diameters of the semicircle response reduce dramatically with the temperature increase. At 400°C, the semicircular response is accompanied by a linear tail extended to low frequency. It is found that each Cole-Cole plot shows only one depressed semicircle. The single semicircle indicates that only one primary mechanism exists for the electrical conduction within the diamond film at temperatures below 300°C. The depressed semicircles make their centres on a line below the real axis, which indicates the departure from the ideal Debye behaviour [Macdonald 1987]. The diameter of each semicircle indicates the electrical resistance of diamond films. With increasing temperature, the diameter decreases indicating the reduction of the resistance from 62 MΩ at room temperature to 4 KΩ at 300°C. The Cole-Cole Plot at 400°C

shows a small semicircle and a long linear tail at low frequency. Such phenomena have been observed in other systems and have been attributed to the AC polarization of diamond/electrode interface at this high temperature [Ramesham 1998].

The Cole-Cole plots for HFCVD diamond films from 25 to 300°C are shown in figure 6.5. The Cole-Cole plot at room temperature shows the presence of an arc, instead of a complete semicircle, with a linear trend at the low frequency impedance range. Similar data are shown at other temperatures. The diameters of these arcs reduce dramatically with the temperature increase. It is difficult to derive the thermal activation energy for HFCVD diamond because there are no clear semicircles in their Cole-Cole plots. However, through the simulation of the each arc, it was found that the capacitance value for each arc is maintained at 0.7pF, which indicates the impedance spectrum is from the grain interior.

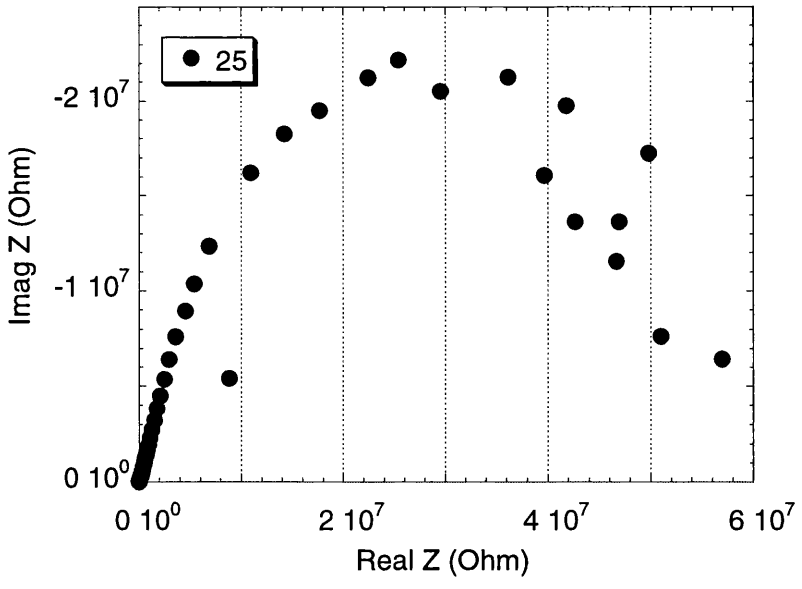

(a) 25°C

(continued on next page)

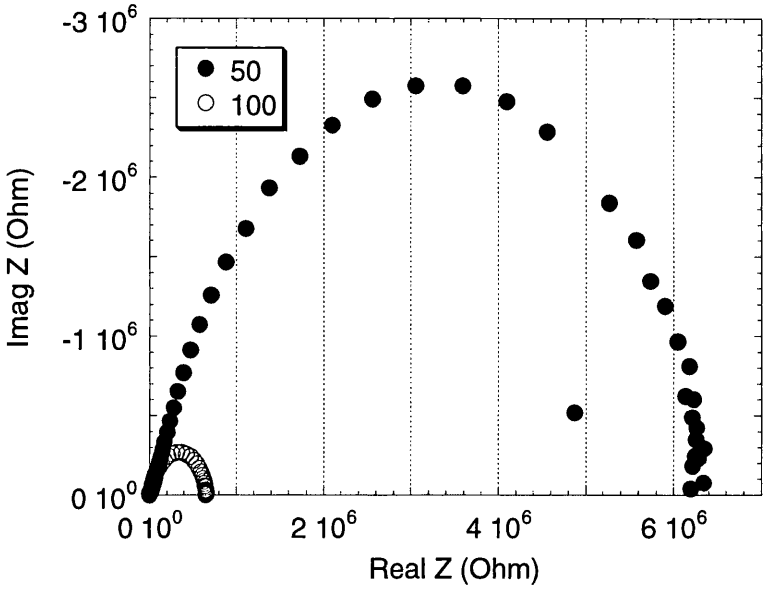

(b) 50°C and 100°C

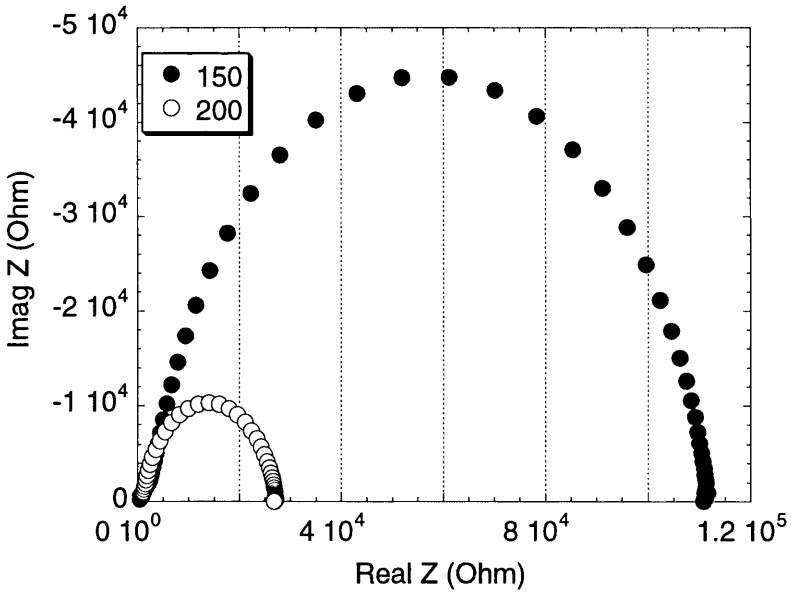

(c) 150°C and 200°C

(continued on next page)

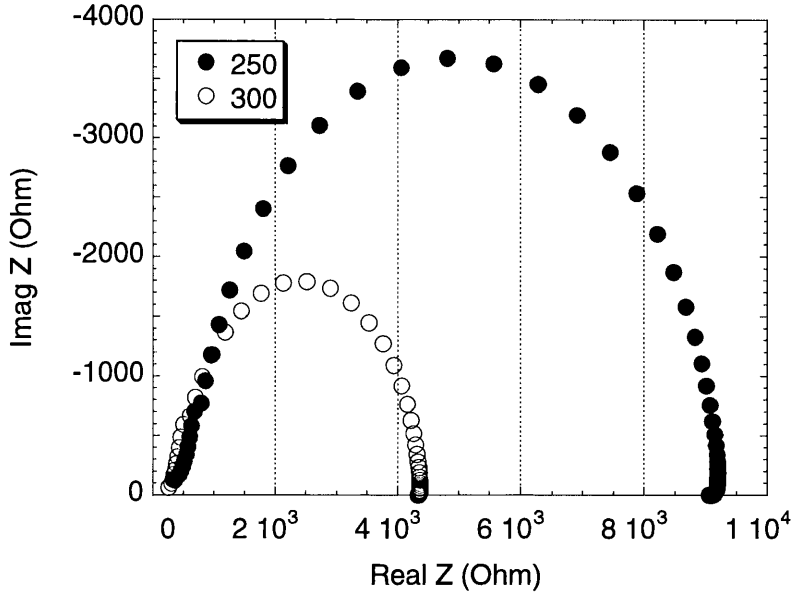

(d) 250°C and 300°C

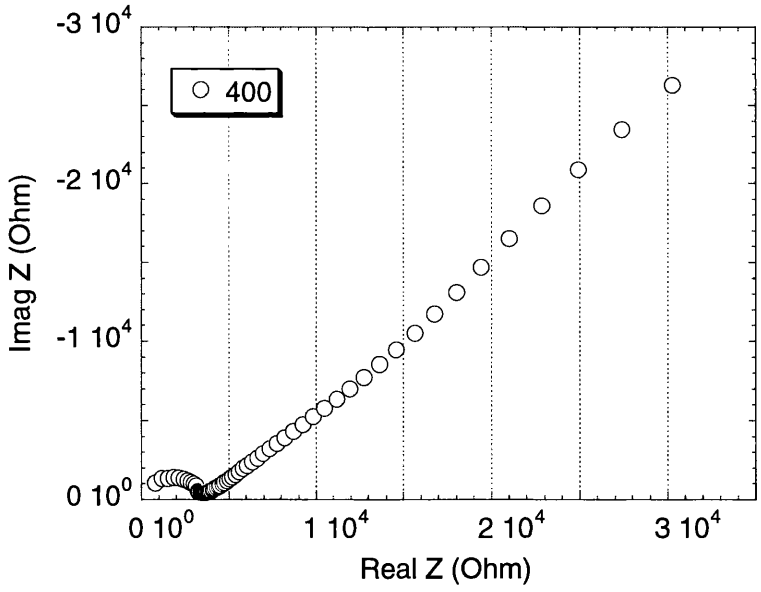

(e) 400°C

Figure 6.3 Cole-Cole Plots of MPECVD diamond films at different temperatures: (a) 25 °C, (b) 50 and 100°C, (c) 150 and 200°C, (d) 250 and 300°C, and (e) 400°C.

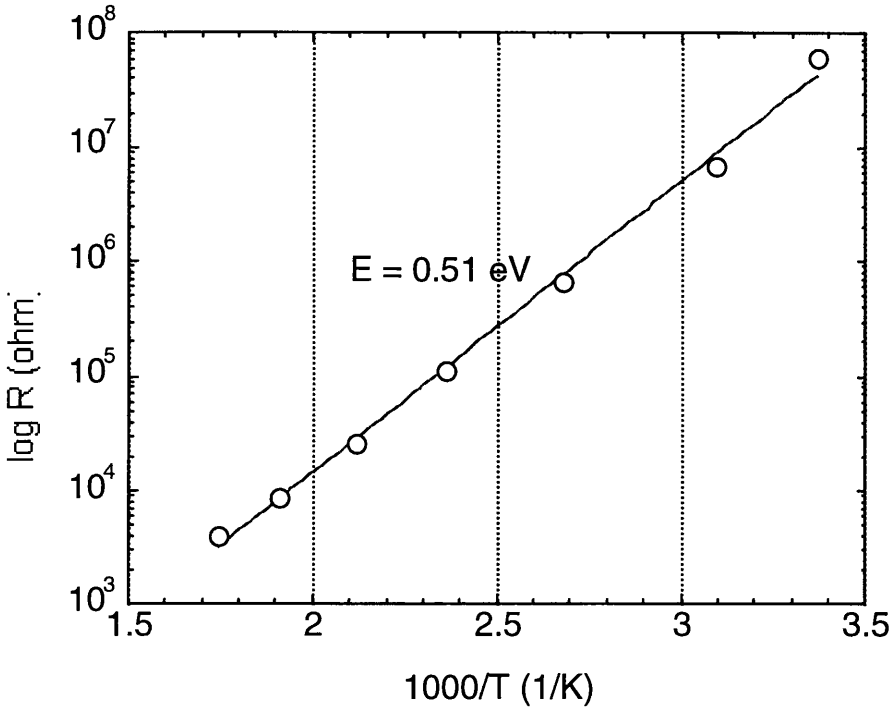

Figure 6.4 Temerature dependence of electrical resistance on MPECVD diamond films.

T (°C)	R (Ω)	C (nF)
25	62000000	0.250
50	6800000	0.210
100	666000	0.203
150	110000	0.201
200	26300	0.232
250	8662	0.230
300	4020	0.225

Table 6.1. Impedance parameters of MPECVD diamond films

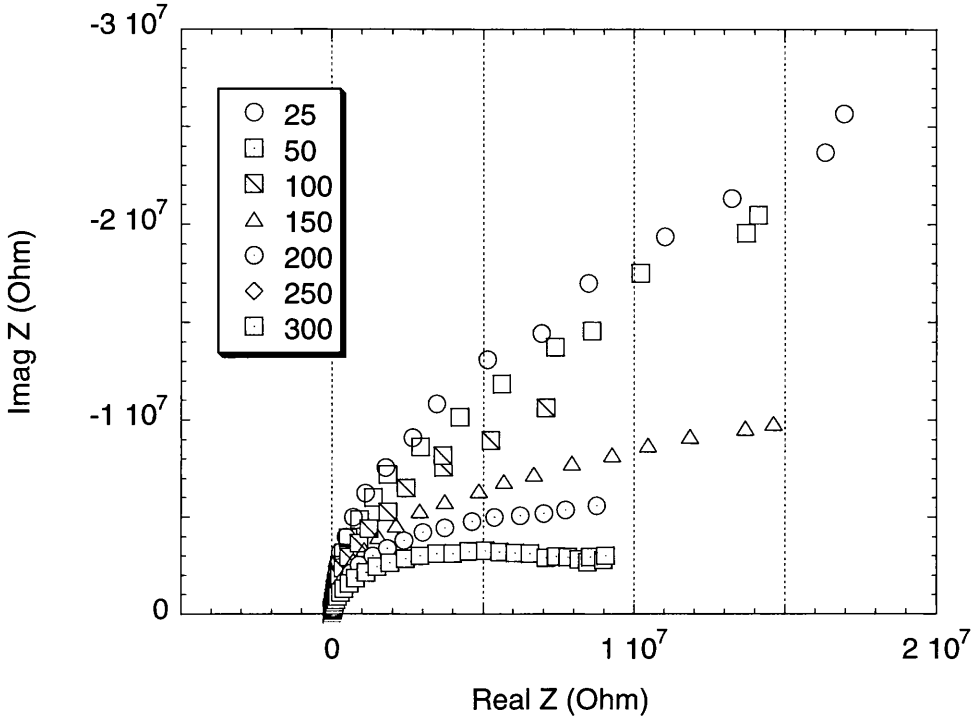

Figure 6.5 Cole-Cole Plots of HFCVD diamond films at different temperatures.

6.4 Discussion

A central issue to be addressed is which portion of the equivalent circuit in figure 3.2, corresponds to the observed single semicircular response. This interpretation is centred to determine the dominance of conduction from grain interiors or grain boundaries or otherwise injection from the electrodes. For ionic conductors, electrode porosity and polarisation must be considered for the general impedance analysis [Bauerle 1969]. Whilst for diamond, different electrode configuration effects have been investigated [Ye and Jackman 2004] and the results show no significant variation in impedance spectroscopy due to its large resistance difference between diamond and electrode. Therefore, the impedance contribution from the electrodes could be ignored in diamond-based materials which are less conductive.

Critical to the identification of the grain boundary and grain interior contribution is the simulated capacitance value for each semicircle. Experimentally [as discussed in section 3.3 of chapter 3], the low frequency dispersion corresponds to the grain boundaries and the higher frequency dispersion corresponds to the grain bulk interior if two semicircles appear, which normally have capacitance values in a nF and pF range, respectively [Ye et al 2001]. The resistance and capacitance values for each semicircle (in figure 6.3) have been simulated using Zview software supplied by Solartron Inc. The detailed values are shown in table 6.1. It is apparent that all the capacitance values are in the range of 0.2 nF. This indicates that these single semicircular responses for MPECVD diamond films are attributed to grain boundaries. In figure 6.4, the calculated resistance for the MPECVD diamond within the Cole-Cole plot, which persists over the whole temperature range investigated here, is presented in a logarithmic plot against reciprocal of temperature. A straight line is apparent, enabling a single electrical activation energy to be estimated from the slope of the curves. The activation energy is found to be around 0.51 eV, which is consistent with the results on deep-level transient spectroscopy (DLTS) [Troupis 2004].

HFCVD diamond is also called thermal management grade diamond or low electronic grade diamond. It contains more defects and non-diamond phases incorporated during the process of CVD. The growth speed for HFCVD diamond is ten times faster than MPECVD, and the quality within both grains and grain boundaries deteriorates [Williams et al 2002]. In the HFCVD diamond both grains and grain boundaries are thought to have contributions to the impedance value. Since the contribution from grains is much stronger than that from grain boundaries, the effect from grain boundaries are negligible. In the MPECVD diamond, the grain boundary conduction is dominating because the high resistance associated with the high-purity diamond grain interiors prevents the current from flowing through the grains. In MPECVD diamond, the only possible way for the current to flow is through the grain boundaries, where graphite and non-diamond phases are embedded.

It can be seen that MPECVD and HFCVD diamond films have different dominating conduction paths within the material itself. This is due to the specific chemical reactions of different CVD processes. The HFCVD technique is the simplest commonly used CVD method for diamond synthesis. It was firstly described by Matsumoto et al [1987]. The thermal energy required for dissociation of molecular hydrogen into atomic hydrogen is supplied by a refractory metal filament (Ta and W) usually heated to about 1900-2000°C; at these temperatures a dissociation efficiency of approximately 10% can achieved [Setaka, 1989]. However, the filaments have a limited lifetime due to carburisation of filament, and physical degradation of the filament usually contaminates the diamond film with metallic impurities. MPECVD technique is also the most commonly used method for activation of the hydrogen, which was first reported by the National Institute for Research in Inorganic Materials in Japan [Kamo et al 1983]. Microwaves are introduced into a deposition chamber which is designed such that a standing wave is created producing a plasma ball just above the substrate; microwaves at 2.45 GHz are usually used. MPECVD produces some of the best quality CVD diamond, with slower growth rates and larger area than HFCVD method. These two different growth techniques have resulted in the deposition of CVD diamond films with different quality as witnessed by SEM, Raman, and Impedance Spectroscopy.

6.5 Conclusions

The work reported in this chapter is the comprehensive comparison of film quality deposited by HFCVD and MPECVD techniques in terms of morphology, structure and impedance properties. It shows that MPECVD diamond films have a dominant electrical conduction path from grain boundaries. However, in HFCVD diamond films, both grain and grain boundaries are thought to have contributions to the overall electrical conduction. Both materials have led to widespread interest in the field of electronic device and electronic packaging application as potentially revolutionary materials.

6.6 References

Baral B, Chan SSM and Jackman RB, J. Vac. Sci. and Technol. **A14** (1996) 2303.

Bauerle JE, Journal of Phys. Chem. Solids **30** (1969) 3657.

Fiegl B, Kuhnert R, Ben-Chorin M and Koch F, Appl. Phys. Lett. **65** (1994) 371.

Field JE, The Properties of Diamond, Academic Press, London, 1979.

Hirose N and West AR, J. Am. Ceram. Soc. **79** (1996) 1633.

Huanosta A and West AR, J. Appl. Phys. **61** (1987) 5386.

Kamo M, Sato Y, Matsumoto S and Setaka N, Journal of Crystal Growth **62** (1983) 642.

Larson JM and Girshick SL, Diamond and Related Materials **12** (2003) 1584.

Lee BJ, Ahn BT, Lee JK and Baik YJ, Diamond and Related Materials **10** (2001) 2174.

Macdonald J.R., Impedance Spectroscopy,(Wiley, New York, 1987), Chap. 4.

Malta DM, von Windheim JA, Wynands HA, and Fox BA, J. Appl. Phys. **77** (1995) 1536.

Matsumoto S, Hino M and Kobayashi T, Appl. Phys. Lett. **51** (1987) 737.

Pickarczyk W and Yarbrough WA, Journal of Crystal Growth **108** (1991) 583.

Ramesham R, Thin Solid Films **315** (1998) 222.

Setaka N, Journal of Materials Research **4** (1989) 664.

Sinclair DC and West AR, Phys. Rev. **B 39** (1989) 13486.

Tang CJ, Neves AJ and Fernandes AJS, Diamond Related Materials **12** (2003) 1488.

Troupis D, PhD Thesis, University of London 2004

Williams OA, Jackman RB and Nebel CE, Phys. Stat. Sol. (a) **193** (2002) 572.

Yarbrough WA and Messier R, Science **247** (1990) 688.

Ye HT, Jackman RB and Hing P, J. Appl. Phys. **94** (2003) 7878.

Ye HT and Jackman RB, J. Appl. Phys. (2004) submitted.

Ye HT, MEng Thesis, Nanyang Technological University (2000).

Ye HT, Sun C, Huang H, Hing P, Appl. Phys. Lett. **78** (2001) 1826.

Ye HT, Sun C, Huang H and Hing P, Thin Solid Films **381** (2001) 52.

Zhu W, Badzian AR and Messier R, in: Feldman A, Holly S (Eds.), Proc. SPIE Diamond Optics III, **1325** (1990) 187.

Zhu W, Stoner BR, Williams BE and Glass J, Proc. IEEE **79** (1991) 5.

Chapter 7

Grain Size Effect

7.1 Introduction

Diamond films are of interest within the field of electronic device packaging, where they could serve as a dielectric layer and heat spreader to a copper heat sink [Drory 1996]. This requires the enhancing of the thermal performance and the lowering of the static dielectric constant in addition to the thermal stability and adequate adhesion between diamond film and substrate. It was generally believed that the smaller the grain size, the smoother the surface morphology and the better adhesion to the substrate for thin film materials. Additionally, although diamond films have a good corrosion-resistive property to some liquids such as boiling KOH, they can permeate the films and attack the underlying material. To prevent this, the individual diamond grain size should be less than 30 nm [Robert 1993]. Understanding the size effect on its electrical properties, therefore, becomes necessary for tailoring this interesting material for a variety of applications.

Noble gases such as He and Ar have salient effects on the crystalline structure and morphology of diamond films [Shih et al 1992]. There are some publications on the tuning of grain size with the addition of Ar in the methane and hydrogen gas system [Zhou et al 1998]. Gu et al [2000] reported the correlations of grain size, growth rate, surface roughness, and process parameters in continuous H^+ ion bombardment during diamond growth. They found that decreasing the grain size will degrade the quality of diamond film synthesized by introducing sp^2 bonded carbon and consequently causing a very high compressive stress in the sample. However, so far, there are few reports on the size effect on the dielectric constant and related propeties. This chapter reports grain size effect on the dielectric constant of MPCVD diamond films, which correlated with XRD, Raman and SEM.

7.2 Experimental Details

Diamond films were deposited on silicon substrates using a microwave plasma enhanced CVD reactor as described previously [Ye et al 2000]. In order to correlate the dielectric constant with the grain size of diamond films, four typical samples with very different grain size were selected for this purpose. The deposition conditions were reported elsewhere through the orthogonal optimization design [Ye et al 2000]. The surface morphology and grain size of the selected films were investigated by a JOEL 5410 scanning electron microscope (SEM) equipped with energy dispersive X-ray spectrometry. The coating crystal structure was obtained by grazing incidence X-ray diffraction (XRD) with Cu K_α 40 kV/30mA. The phase purity of diamond films was evaluated using Raman spectroscopy with the 514 nm line of an argon ion laser.

The dielectric constant of diamond films was measured with a FLUKE PM-6306 RCL Meter using two-point probe method across the film. Because silicon substrates have high conductivity, which is higher by several orders of magnitude compared with synthesized CVD diamond films [Unagami 1980, Beale et al 1985, Lehmann et al 1995], i.e., the resistivity of the silicon substrates is much lower than that of the diamond films, the effects of conducting current through the silicon substrates on the resistance and dielectric properties measured were estimated to be less than 0.1% and thus the effects of silicon could be ignored [Miyata and Dreifus 1994, Ye et al 2001]. Silver paste was used for a metal contact to the silicon substrate and diamond film, respectively. The samples were then dried at 80 °C for 1 hr to make the experimental data reproducible.

7.3. Experimental Results

SEM images of synthetic diamond films with different grain size are shown in figure 7.1. Statistical trend analysis in orthogonal optimization design reveals that the grain size decreases from 10 to 0.5 μm with an increase in Ar/H_2 ratio from 10 to 75%. Besides, at low Ar concentration, well-faceted diamond crystals have been synthesized as shown in figures 7.1 (a)-7.1 (c). With increasing Ar ratio, cauliflower and nanocrystalline diamond films are obtained. Argon is a noble gas, which is quite difficult to react with other elements. However, Ar plasma was found to have a profound effect on plasma chemistry, including additional ionization and dissociation. Upon adding argon, the emission intensity of various species changes and the growth rate of the diamond is enhanced [Zhu et al 1990]. Sumil [1991] reported that the bombardment of the depositing species with Ar^+ ions present in the plasma lead to the removal of hydrogen from the surface and a preferential re-sputtering of weakly bonded graphite precursors from the film surface giving rise to diamond-like properties of the films. Weide and Nemanich found the film surface after the argon plasma exhibits a positive electron affinity of 10 eV while after hydrogen plasma exhibits a negative electron affinity, indicating the removal of hydrogen from the surface [Weide and Nemanich 1993].

Here the effect of Ar on diamond growth could be concluded and separated into four different parts: (1) initiating the plasma and heating the silicon substrate; (2) etching and cleaning of substrate surface before nucleation occurs; (3) decreasing the mean free path of reactive gas, and hence increasing the deposition rate; (4) increasing the concentration of C_2 dimer in the plasma discharge; (5) minimizing grain size of diamond films and resulting in the formation of nanostructured diamond. It is still not clear about the reactive nature of the argon ions during plasma processing so far.

XRD pattern for diamond films are shown in figure 7.2. Figures 7.2 (a)-7.2 (d) correspond to the samples (a)-(d) as shown in figure 7.1. It is found that the full width at half-maximum (FWHM) of diamond (111) diffraction peak broadens with the decrease of grain size.

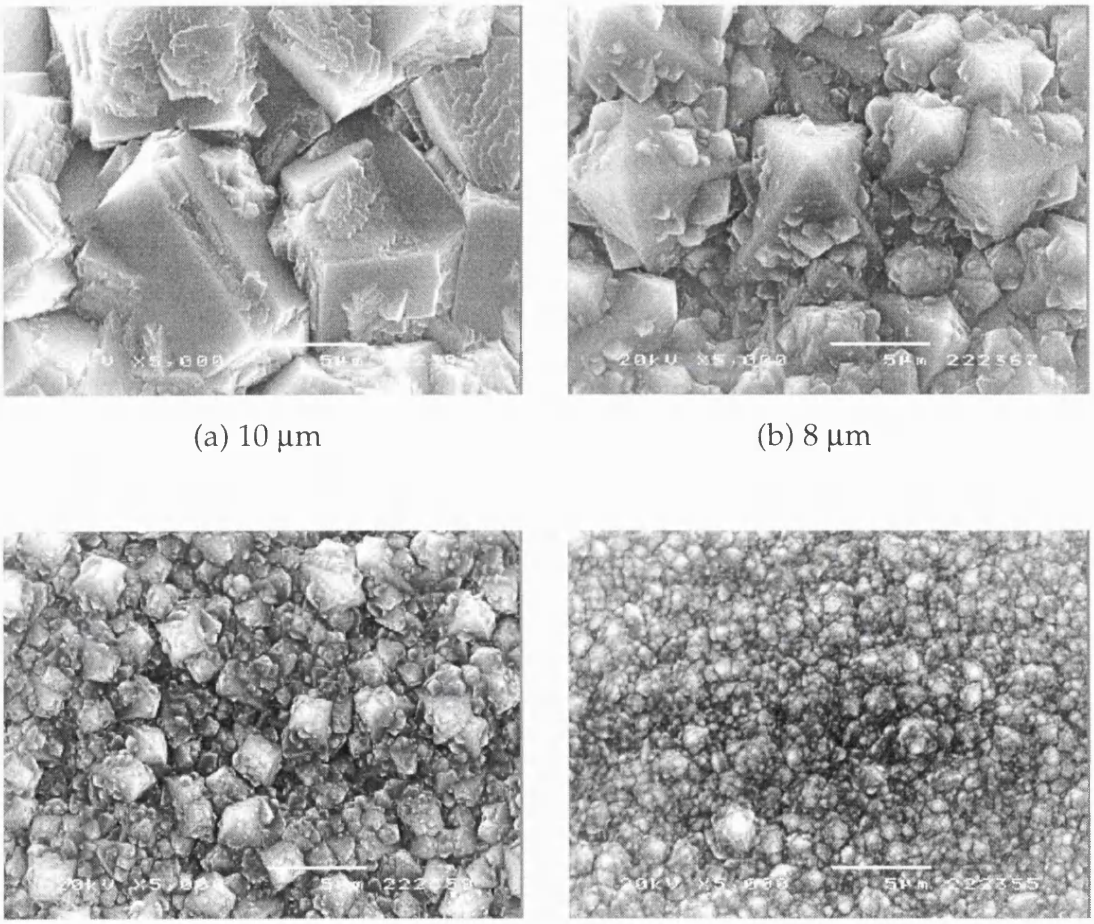

(a) 10 μm (b) 8 μm

(c) 1.5 μm (d) 0.5 μm

Figure 7. 1 SEM photography of diamond films on silicon (100) with different grain size.

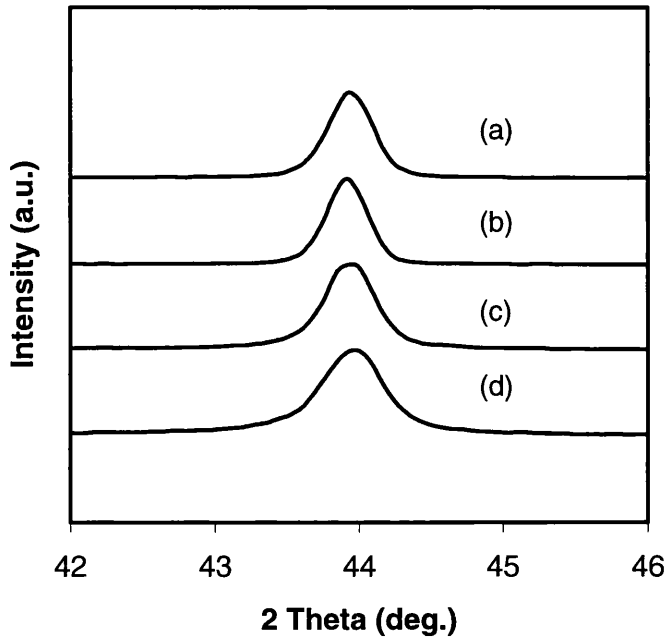

Figure 7.2 XRD pattern for diamond films show the broadening of FWHM of diamond (111) with the decrease of grain size.

The dielectric constant for each sample was calculated from the original value of capacitance measured through:

$$\varepsilon_r = \frac{Cd}{\varepsilon_0 A} \tag{7.1}$$

where ε_r and ε_0 are dielectric constant of diamond film and vacuum, respectively. C is the capacitance measured. d is the thickness of the diamond films (1~2 μm). A is the area of silver electrodes ($0.25^2\ \pi$ cm^2). The grain size dependence of dielectric constant and the FWHM of the diamond (111) peak in XRD are shown in figure 7.3. Relative X-ray diffraction peak intensities from crystalline planes (111) and (220) are summarized in table 7.1. It was found that with the grain size increase from 0.5 to 10 μm, the dielectric constant increases from 0.95 to 8.13, and the FWHM decreases from 0.471° to 0.282°. It reveals that the dielectric constant can be reduced effectively by reducing the grain size from micrometer scale to nanometer scale. It implies that nanostructure diamond film has high potential to serve as a dielectric layer in electronic

packaging, if a suitable thermal performance and adequate adhesion are achieved, combined with the excellent self-lubrication and friction properties of nanostructure itself.

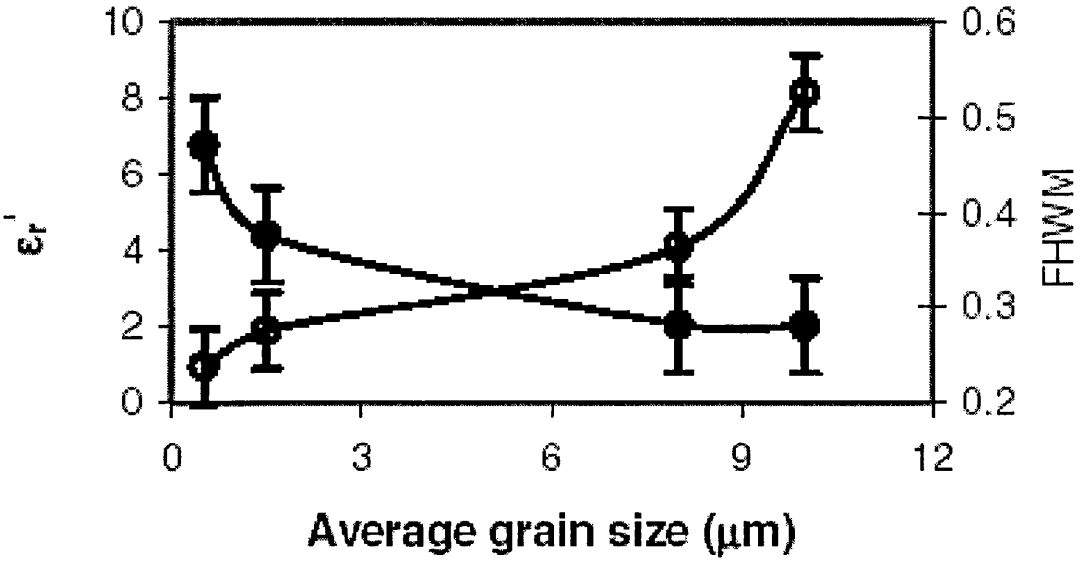

Figure 7.3 Grain size dependence of dielectric constant (o) and FWHM of the diamond (111) peak in XRD (•).

Grain size (μm)	Face	Peak (deg.)	FWHM (cm^{-1})	d-value (Å)	Intensity	I/Imax
10	(111)	43.92	0.282	2.0598	7698	100
	(220)	75.36	0.471	1.2602	2961	38
8	(111)	43.92	0.282	2.0598	18412	100
	(220)	75.28	0.376	1.2613	2602	14
1.5	(111)	43.92	0.376	2.0598	2457	100
	(220)	75.36	0.376	1.2602	885	36
0.5	(111)	44.00	0.471	2.0562	5801	100
	(220)	75.36	0.471	1.2602	819	16

Table 7.1 Relative XRD diffraction peak intensities from crystalline planes (111) and (220) of diamond films with different grain size.

7.4 Discussion

The dramatic changes with grain size with in dielectric constant of diamond films as a result of argon addition into the reactant gases may be largely dominated by the following three factors: (1) Phase purity, (2) Films thickness, and (3) Grain boundaries.

Numerous studies have investigated the grain size effect on morphology transitions of polycrystalline diamond films by controlling and tuning the growth parameters in literature. A series of transitions in morphology and textures of diamond films upon the nitrogen addition were reported by Ayres et al [2001]. Locher et al [1994]concluded that the film quality degraded when the upper end concentration of nitrogen was beyond 400 parts per million (ppm). Ahmed et al [2000] believe that the growth rate, resistance and the degree of sp^3 content optimize at 200 ppm of nitrogen and degrade considerably with increasing nitrogen concentration. Abbott et al [2001] reported the effect of grain size on the work function of diamond films. They proposed that the work function increases from 3.6 eV to 5.2 eV with decreasing grain size from 9.6 μm to 0.3 μm, which is due to the graphitic/amorphous grain boundaries begin to dominate. Birrell et al [2002] reported that the grain size will increase with the addition of nitrogen, but the overall bonding structure remains unchanged. Through graded growth of diamond films, Einaga et al [2001] presents that decreasing the growth temperature will decrease the grain size, however the quality of the films seems to be independent on the grain size. Controversially, Gruen's group [1999] report a continuous transition from microcrystalline to nanocrystalline diamond films by argon addition into reactants. The corresponding quality evaluated by Raman spectroscopy is strongly dependent on the grain size.

In order to understand the change of film quality of samples with grain size in my results, Raman spectroscopy was used to characterize these films, which is shown in figure 7.4. All the samples with differing grain size show a sharp Raman band at 1332 cm^{-1}, which is the characteristic of diamond. Little Raman scattering is observed in the range of 1400-1600cm^{-1}, which is caused by sp^2 bonded carbon. As Raman scattering is about 50 times more sensitive to amorphous carbon and graphite than to diamond, the results from the set of samples indicate that the deposited diamond films are of high quality, which is independent of grain size. The bond structure and phase purity are kept unchanged for all the four samples. Since phase purity has been proved not to contribute to the change of dielectric constant and the films were grown about 2μm thick for all the four samples, the only possible assignment which is responsible for the change of the dielectric properties is from the grain boundaries.

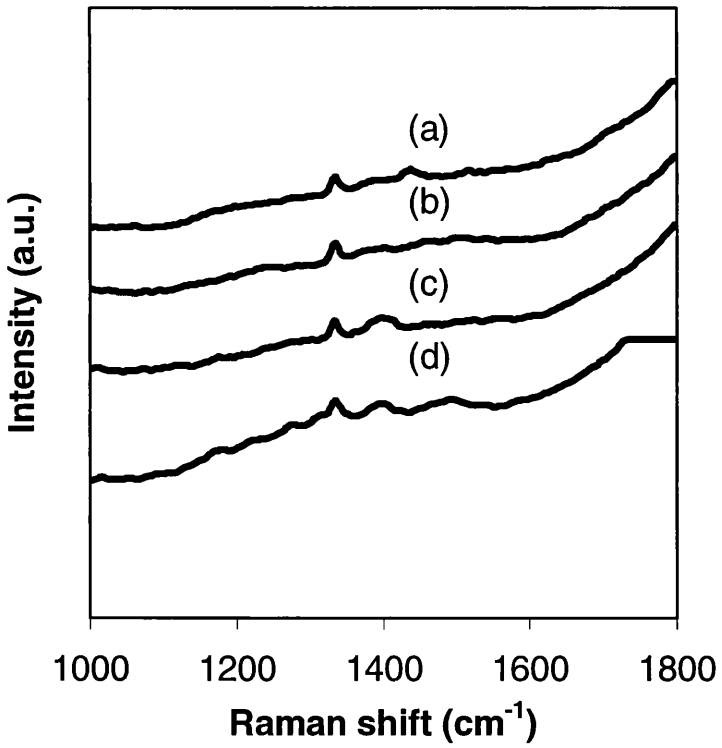

Figure 7.4 Grain size dependence of Raman spectroscopy: (a) 10 μm, (b) 8μm, (c) 1.5μm, and (d) 0.5μm.

The physical mechanism responsible for the observed phenomena can be explained as the change of the crystal field caused by surface bond contraction at grain boundaries. Generally it is considered that the difference of grain boundaries influence the sp^2 carbon component, surface termination, or reconstruction [Einaga et al 2001]. Previous work has proven that nanostructure material has an enhanced crystal field due to its surface bond contraction and the rise in surface-area-to-volume ratio. Decreasing the particle size increases the crystal field and subsequently decreases the dielectric constant.

The complex dielectric constant of a material is given as:

$$\varepsilon_r(\omega) = \varepsilon_r'(0) + i\,\varepsilon_r''(\omega) \tag{7.2}$$

$$\varepsilon_r'(0) = \chi + 1 = n^2 \tag{7.3}$$

The real part is the static ε_r describing the polarization of electrons, which is independent of the frequency of incident waves. n is the refractive index, and χ is the electron polarization coefficient. The imaginary part describes the electromagnetic wave absorption, being responsible for the energy loss of the incident waves [Hench and West 1989].

The static dielectric constant variation with the band gap is derived as [Tsu and Babic 1994]:

$$\frac{\Delta\chi}{\chi} = -2\left(\frac{\Delta E_g}{E_g}\right) \tag{7.4}$$

where E_g is the band gap. It can be seen that electron polarization coefficient (χ) depends on the band gap expansion ($\Delta E_g/E_g$).

The particle size determined band gap is expressed as [Sun et al 1999]:

$$\frac{\Delta E_g}{E_g} = \sum_{i \leq 3} \gamma_i \left(c_i^{-m} - 1 \right) + \delta \qquad (7.5)$$

where γ is the ith surface-to-volume ratio of a particle [Sun 1999]. i counts from the outermost layer of the particle. c_i is the coefficient of bond contraction due to the reduction of coordination number of surface atoms [Goldschmidt 1927]. m is an adjustable parameter that depend on the type of atomic potential. δ describes the contribution of cluster interaction to the band gap enlargement. As δ is assumed very small and could be ignored. The band gap expansion results from the surface bond contraction (c_i) and the rise in surface-to-volume ratio that depends on the shape and size of the particles as well as the type of atomic interaction. Consequently the band gap expansion results in the decrease of dielectric constant with the decrease of grain size.

7.5 Conclusions

The grain size effect on the dielectric constant of diamond films was investigated. It is found that increasing Ar gas ratio reduces the grain size of diamond films, consequenctly reducing the dielectric constant of diamond. The grain size effect on the dielectric constant could be explained as the change of crystal field caused by surface bond contraction of the nanoscaled particles at grain boundares.

7.6 References

Abbott P, Sosa ED and Golden DE, Appl. Phys. Lett. **79** (2001) 2835.

Ahmed W, Rego CA, Cherry R, Afzal A, Ali N and Hassan IU, Vacuum **56** (2000) 153.

Ayres VM, Farhan M, Spach D, Bobbitt J, Majeed J, Wright BF, Wright BL, Asmussen J, Kanatzidis MG and Bieler TR, J. Appl. Phys. **89** (2001) 6062.

Beale MIJ, Benjamin JD, Uren MJ, Chew NG and Gullis AG, Journal of Crystal Growth **73** (1985) 622.

Birrell J, Carlisle J, Auciello O, Gruen DM and Gibson J, Appl. Phys. Lett. **81** (2002) 2235.

Drory MD, *AIP Conf. Proc.* **361** (1996) 921.

Einaga Y, Kim G, Ohnishi K, Park S and Fujishima A, Materials Science and Engineering **B83** (2001) 19.

Goldschmidt VM, Ber. Deut. Chem. Ges. **60** (1927) 1270.

Gruen DM, Annual Review of Materials Science **29** (1999) 211.

Gu C and Jiang X, J. Appl. Phys. **88** (2000) 1788.

Hench LL and West JK, *Principles of Electronic Ceramics* (Wiley, New York, 1989).

Lehmann V, Hofmann F, Moller F and Gruning U, Thin Solid Films **255** (1995) 20.

Locher R, Wild C, Herres N, Dehr D and Koidl P, Appl. Phys. Lett. **65** (1994) 34.

Miyata K and Dreifus DL, Japanese J. of Appl. Phys. **33** (1994) 4526.

Robert FD, *Diamond Films and Coatings, Development, Properties and Applications*, NOYES PUBLICATIONS, (1993) p14.

Shih HC, Sung CP and Fan WL, Surface Coatings Technol. **54/55** (1992) 380.

Sumil K., Appl. Phys. Lett. **58** (1991) 1836.

Sun C., Gong H. Q., Hing P. and Ye HT., Surface Review Lett. **6** (1999) L171.

Sun C, J of Phys.: Condense Matters **11** (1999) 4801.

Tsu R and Babic D, Appl. Phys. Lett. **64** (1994) 1806.

Unagami T, J. Electrochem. Soc. **127** (1980) 476.

Weide J. van der and Nemanich RJ, Appl. Phys. Lett. **62** (1993) 1878.

Ye HT, Sun C and Hing P, J. Phys. D: Appl. Phys. **33** (2000) L148.

Ye HT, Sun C and Hing P, Thin Solid Films **381** (2001) 52.

Ye HT, Sun C, Hing P, Xie H, Zhang S and Wei J, Surface Coatings Technol. **123** (2000) 129.

Zhou D, Gruen DM, Qin LC, McCauley TG and Krauss AR, J. Appl. Phys. **84** (1998) 1981.

Zhu W, Inspektor A, Badzian AR, Mckenna T and Messier R, J. Appl. Phys. **68** (1990) 1489.

Chapter 8

Nanocrystalline Diamond

8.1 Introduction

The emergence of chemical vapor deposition (CVD) technique for the growth of thin film diamond has led to widespread interest in the use of this material for electronic applications. The focus of most growth studies to date has been in the production of high quality, large grain polycrystalline diamond, with the realization of single crystalline material remaining a key aim of the diamond research community. Early reports on fine grain nanocrystalline diamond received less attention since they did not appear to fit with these aims [Beckman et al 1994, Jackman et al 1995]. However, this position has recently changed with the properties of nanocrystalline films themselves being recognized as potentially useful for many applications in fields as diverse as electrochemical electrodes, tribology, cold cathodes, corrosion resistance, and conformal coatings on MEMs devices [Hayward 1991, Chandrasekar and Bhushan 1992, Swain et al 1998, Rotter 1998, Zhou et al 1998, Krauss et al 2001, Jiao et al 2001].

A variety of deposition techniques and conditions have been employed to grow the nanocrystalline diamond films. Among these are remote microwave plasma [Erz et al 1993], microwave plasma [Lee et al 1996], DC arc [Nistor et al 1997], Hot filament CVD [Khomich et al 1996], glow discharge-RF [Fedoseev et al 1996], carbon sputtering [Kundu et al 1997], and electron-cyclotron resonance [Zarrabian et al 1997]. Erz et al [1993] grew 800 nm thick films with 10% CH_4 in H_2, which were characterized by XRD, Raman and visible infrared spectroscopy. Konov et al [1995] and Nistor et al [1997] produced 0.2-1 μm thick films from $CH_4/H_2/Ar$ mixtures that were characterized chiefly with XRD, Raman, and high-resolution transmission electron microscopy (TEM). The Ar ratio in the mixtures was kept at 50%. Grain sizes were found to be in the range 30-50 nm. TEM did not reveal amorphous carbon in significant quantities, but disordered sp^3- and sp^2-bonded amorphous carbon was detected, presumably located at grain boundaries. The diamond crystallites are highly defected with many twins and other planar defects. Khomich et al [1996] deposited 100-200 nm crystallites with the

appearance of polycrystalline conglomerates. Lee et al [1996] prepared nanocrystalline films from CH_4/H_2 mixtures and concluded real-time spectroscopic ellipsometry to measure activation energies. Microhardness, electrical conductivity and the effect of methane pressure on film growth rate was studied by Fedoseev et al [1996]. Films produced by Zarrabian et al [1997] from an ECR plasma were studied by TEM and EELS and found to consist of 4-30 nm crystallites embedded in DLC. Magnetron sputtering of vitreous carbon produced films in which the nanocrystallites were embedded in an amorphous carbon matrix [Kundu et al 1997]. By adjusting the ration of noble gas to hydrogen in the gas mixture, Gruen's group has achieved a continuous transition from microcrystalline to nanocrystalline [Gruen 1999].

Impedance Spectroscopy is a technique that allows the identification of electrical conduction paths within a polycrystalline material as attributable to grain interiors, grain boundaries, or electrode injection phenomena. Details of the technique can be found in chapter 3. However, in essence the technique allows an equivalent circuit representation of the material system under study to be proposed, and the experimental data determined to be compared to simulated data based on manipulation of the circuit parameters within the equivalent circuit. This chapter shows evidence for both grain boundaries and grain interior conduction within the silicon-supported nanocrystalline diamond films used here.

8.2 Experimental Details

All films studied here were produced using a commercial supplied 2.45 GHz resonant standing wave cavity microwave plasma enhanced CVD system. It has been already demonstrated that good quality, microcrystalline diamond films can be really produced on suitably treated Si substrates using $CH_4/H_2/O_2$ gas mixtures [Spitzl et al 1994, Jin and Moustakas 1993, Fedoseev et al 1993, Zhu et al 1994]. The introduction of Ar in place of the oxygen has been shown to

lead to nanocrystalline film production [Jiao et al 2001, Zhou et al 1998]; this approach has been used here, with typical growth conditions being shown in table 8.1.

The crystal structure of the coatings was investigated using x-ray diffraction utilizing Cu $K\alpha$ radiation at incident angle of 1° to the sample surface, produced using 40kV/30mA electrons. The precise lattice parameters were determined by the least-squares method using more than ten reflection peaks that appeared in the scan range of 30-80°, with a step of 0.08° and a scan speed of 4°/min. The surface morphology of the deposited coating was investigated using a scanning electron microscope (SEM; JSM-5410LV, JEOL) attached to an energy dispersive x-ray spectrometer. The impedance properties of the diamond films were determined using a Fluke PM6306 RCL meter covering the frequency range from 50 Hz and 1 MHz, over a temperature range of 25-500°C.

Parameter	**Value**
Microwave power (kW)	2.0
Gas mixture: $Ar/H_2/CH_4$ (sccm)	50/146/4
Gas pressure (Torr)	50
Deposition time (hr)	12
Substrate temperature (°C)	700

Table 8.1 Deposition conditions for nanocrystalline diamond films on Si substrates. Commercial single crystal silicon (001) wafers mechanically roughened with a 1μm diamond paste were used as substrates throughout.

Silver paste was used to form metal contacts to both the diamond film and silicon substrate, as the type of metal contact has no significant effects on impedance results. The diameter of the electrode is 4 mm. The effect of current conduction through the silicon substrate on the measured resistance was estimated to be less than 0.1% over the frequency range used and thus can be ignored; a similar assumption has been used previously by others [Miyata and Dreifus 1994].

Measurements of the impedance data for polycrystalline materials using RCL meter is well suited to providing information related to the electrical conduction of both the grain interiors and to the grain boundary regions. This is illustrated in figure 8.1, which contains the equivalent circuit in panel (a) for the electrical response of polycrystalline materials. The circuit has a direct relationship to the complex Cole-Colt plots (b) in which Z'', the imaginary part of the complex impedance, is plotted against Z', the real part, for a wide range of frequencies (typically 10^{-3}-10^{8} Hz) [Hench and West, 1989]. The resistance R_{gi}, R_{gb} and R_e corresponding to the grain interior, grain boundary and electrode, respectively, can be obtained from the diameter of each semicircle in this plot. Dielectric relaxations contributed from grain interiors, grain boundaries, and electrodes are located in the high frequency, middle frequency, and low frequency, respectively as shown in figure 8.1 (b). Due to the large difference in the resistance of the diamond and Au contacts, the impedance contribution from the electrode itself will be negligible during these experiments.

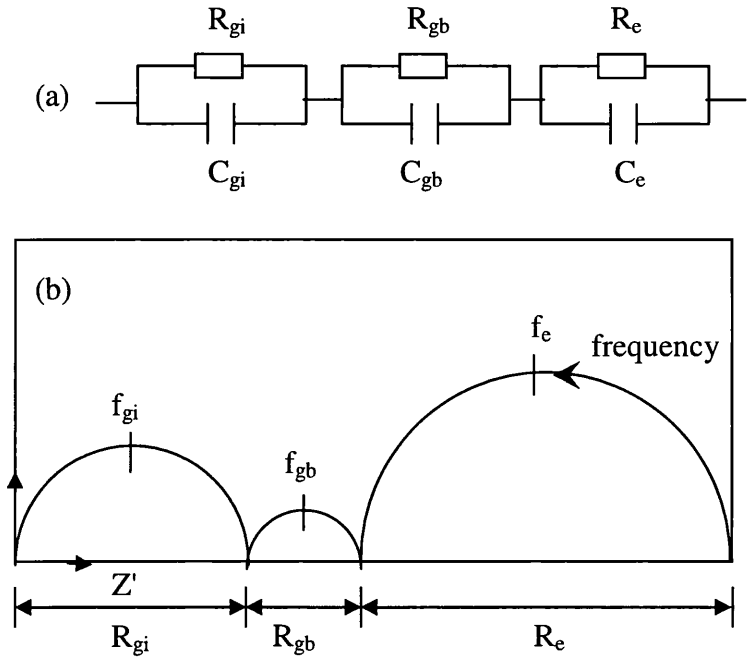

Figure 8.1 Equivalent circuit for the electrical response of a polycrystalline sample showing contributions from the grain interiors (gi), grain boundaries (gb) and electrolyte/electrode interface (e). Complex impedance plot in panel (b) corresponds to the circuit in panel (a).

8.3 Experimental Results

8.3.1 Characterization of Film Quality

Diamond films deposited from $Ar/H_2/CH_4$ gas mixtures appears uniform across silicon substrate as shown in figure 8.2 (a). The films synthesized comprise randomly oriented fine grains 50-100 nm in size. Grazing incidence X-ray diffraction analysis of the diamond films using a Rigaku diffractometer are shown in figure 8.2 (b). The XRD pattern confirms the appearance of diamond (111) and (220) crystal peaks at 2 theta of 43.92° and 75.36°, respectively. The index of the peaks are denoted in figure 8.2(b), which are consistent with the Powder Diffraction Standard (PDS) card of natural diamond (No. 6-0675). The full width at half-maximum (FWHM) of the diamond (111) peak (0.471°) is larger than that has been previously reported

(0.282°) [Ye et al 2001], which probably arises through the decrease of the grain size from micrometer scale down to the nanometer scale. The XRD peak located at 57.13° originates from the (311) orientation of the silicon substrates.

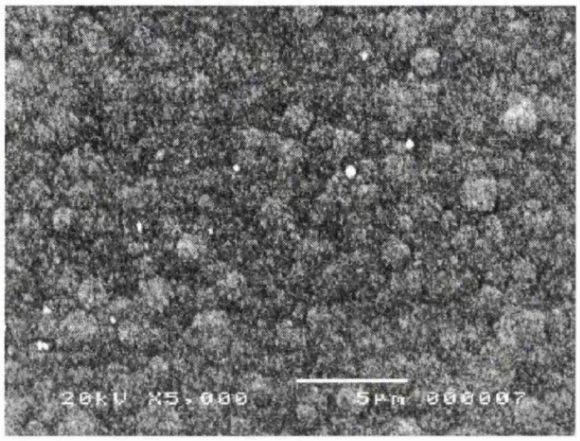

(a)

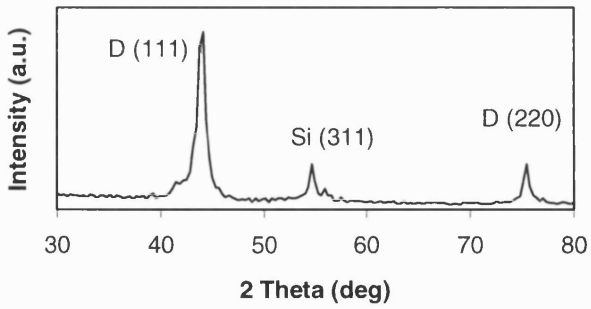

(b)

Figure 8.2 SEM image (a) and XRD profile (b) of nanocrystalline diamond film.

8.3.2 *Characterization of Electrical Behaviour*

Prior to the impedance measurement, both surfaces of the sample were coated with silver paste to form the necessary electrodes, followed by annealing in air at 500°C for 2 minutes to ensure the electrode stability. A schematic diagram of the actual electrical measurement arrangement for diamond films supported on silicon substrates is shown in figure 8.3.

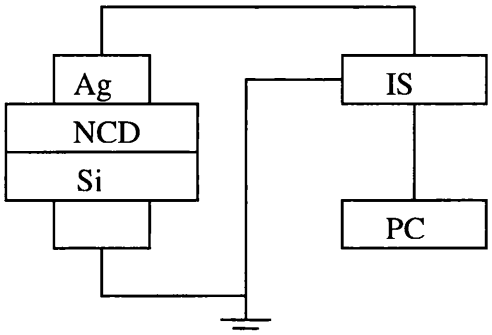

Figure 8.3 Schematic diagram of the electrical measurement across the film thickness.

The temperature dependence of the characteristic Cole-Cole plots measured for these diamond films is shown in figures 8.4 (a)-8.4 (e). Figure 8.4 (a) presents the data measured at 25°C and 100°C, respectively, showing the presence of a single semicircular response, with some scatter in the data in the low frequency impedance range. Similar data are shown in figure 8.4 (b) for the temperatures of 150°C and 200°C. The diameter of the semicircular response is reduced dramatically with the increase of the temperature. Beyond 250°C, shown in figure 8.4 (c) - 8.4 (e), the semicircular response is accompanied by an additional semicircle (or an arc) which extends to low frequencies.

In figure 8.5, the calculated resistance for the higher frequency semicircular response within the Cole-Cole plot, which persists over the whole temperature range investigated here, is presented in a logarithmic plot against

reciprocal temperature. A straight line is apparent, enabling a single electrical activation energy to be estimated from the slope of the curves. Attention should be paid to the steep transition of the activation energy from 0.13 eV to 0.67 eV at 250°C, coincident with the emergence of the second semicircular response.

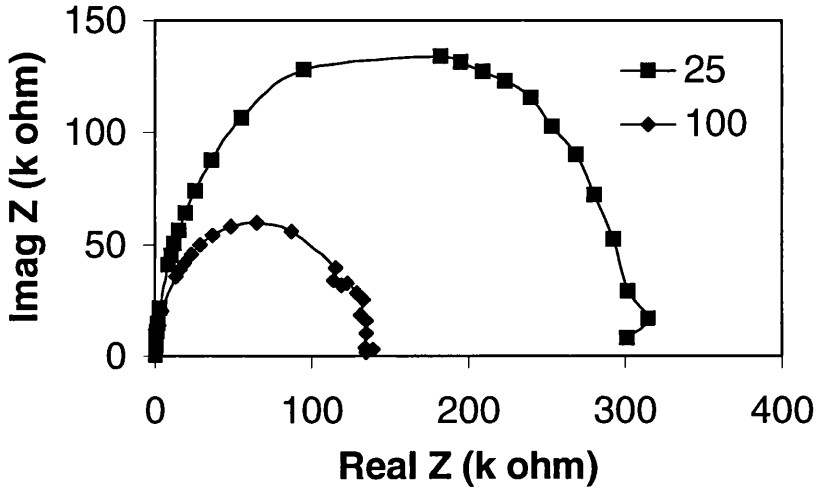

(a) 25°C and 100°C

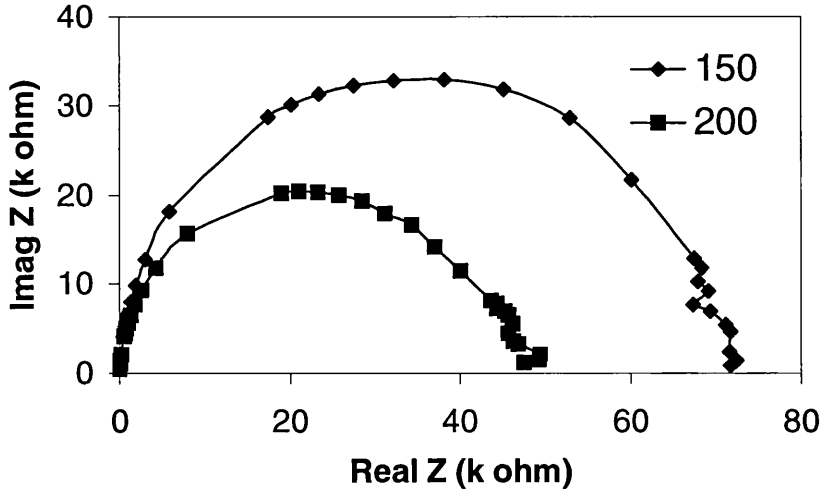

(b) 150°C and 200°C

(continued on next page)

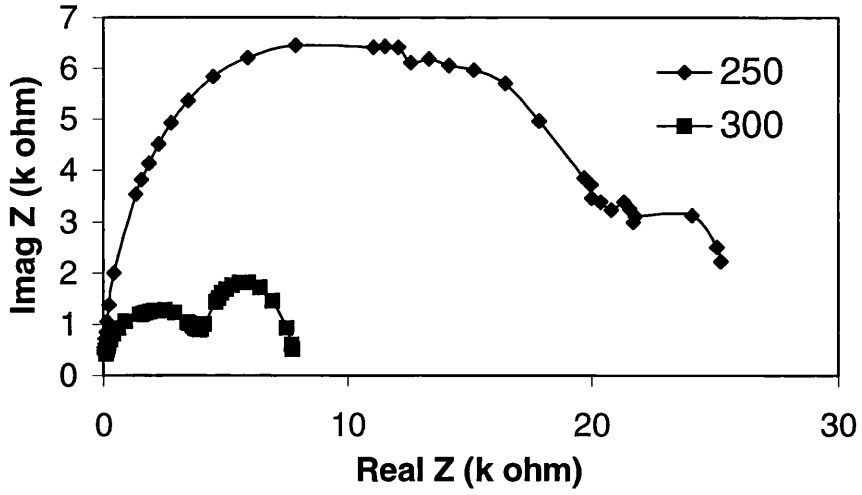

(c) 250°C and 300°C

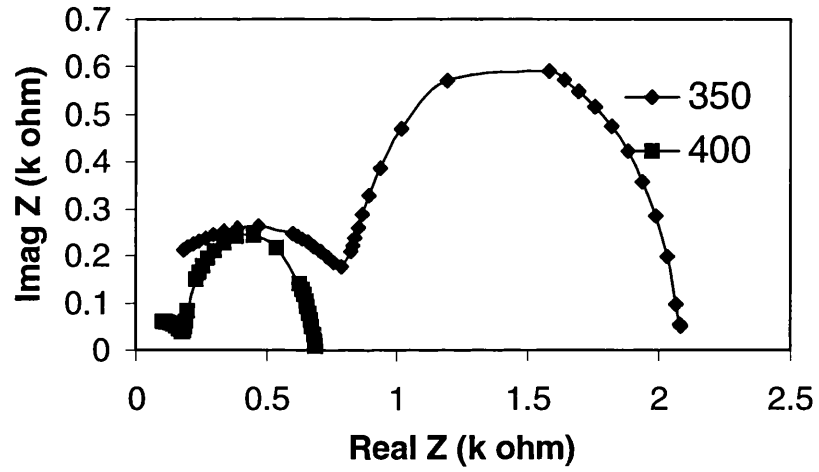

(d) 350°C and 400°C

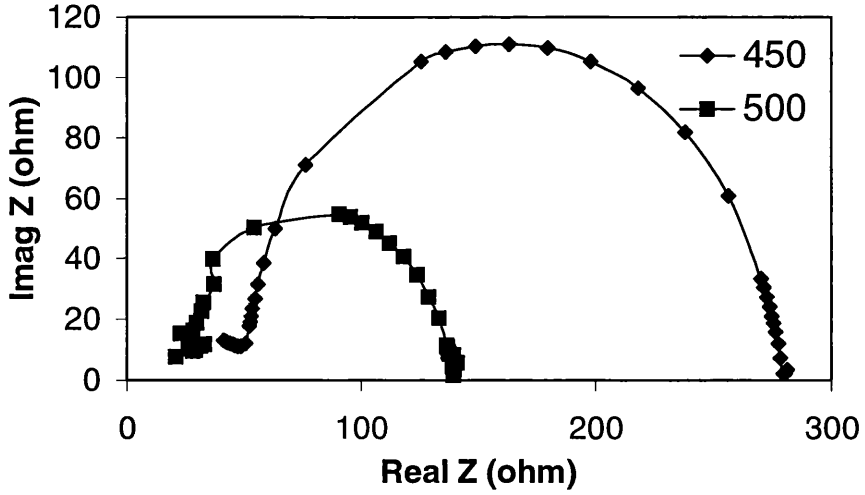

(e) 450°C and 500°C

Figure 8.4 Temperature dependence of the Cole-Cole plots of the diamond films: (a) 25°C and 100°C, (b) 150°C and 200°C, (c) 250°C and 300°C, (d) 350°C and 400°C, and (e) 450°C and 500°C.

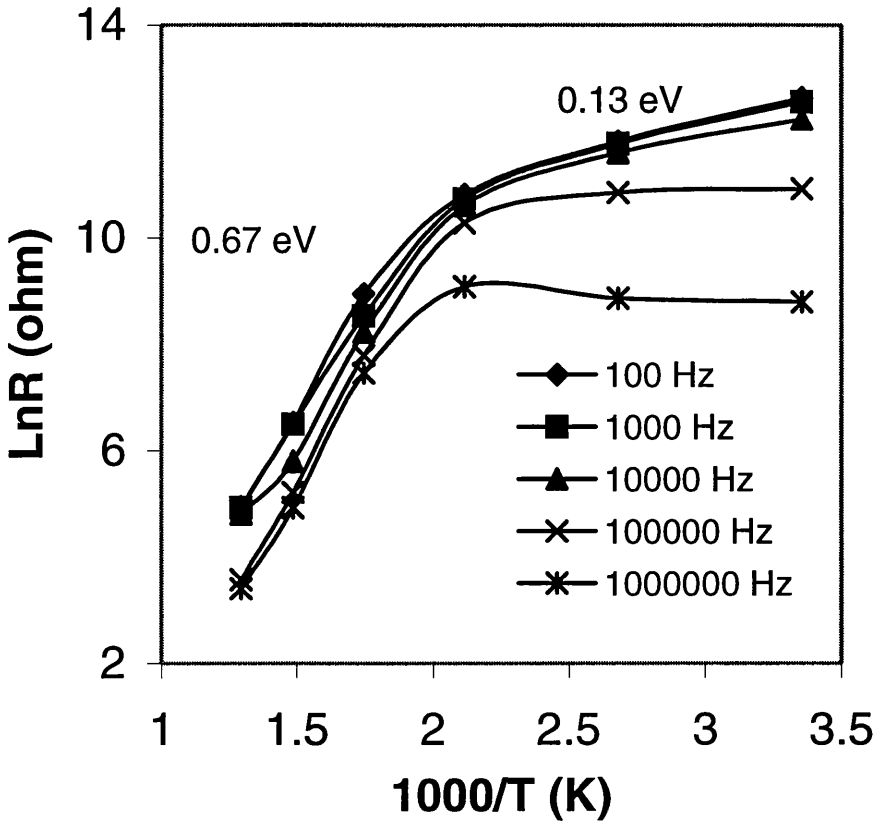

Figure 8.5 Temperature and frequency dependence of the bulk grain interior resistance obtained by fitting the impedance spectra. The activation energy is estimated from the slope as 0.13 eV below 250°C and 0.67 eV above 250°C, respectively.

8.4 Discussion

8.4.1 Experimental Interpretation

It has been found that each Cole-Cole plot below 250°C shows only one depressed semicircle, as indicated in figures 8.4(a) and 8.4(b). The single semicircle indicates that one primary mechanism exists for the polarization within the diamond film at these temperatures. The presence of the single semicircle in this frequency range corresponds to the electrical conduction from bulk grain interior. The diameter of each semicircle corresponds to the

resistance for the particular contribution from the diamond grain interior at each temperature. As the temperature increases, the diameter of the semicircle decreases, indicating a reduction of the grain interior resistance. There appears to be no secondary semicircular response over the frequency range measured here for temperatures below 250°C; it can therefore be summarized that the electrical conduction within these diamond films is being dominated by the diamond grain interiors.

When the temperature is raised above 250°C, the dominant electrical conduction mechanism changes. It is found that a secondary semicircular response occurs in the low frequency range. In this case, two distinct semicircular relaxations were observed in figures (c)-(e), although the high frequency response is incomplete at higher temperatures and is replaced by an arc. It is now possible to identify the contributions from the grain interior and grain boundary resistances from the visible arcs or semicircles of the Cole-Cole plots [Macdonald, 1989]. The arc on the left (high frequency) is assigned to the electrical behaviour within the grain interior, as discussed above, while the feature on the right (low frequency) is assigned to the grain boundaries. The high frequency semicircular response (left) changes from a perfect semicircle into an imperfect arc and begins to disappear with increasing temperature. This is due to the frequency limitation of the equipment used here [Ye et al 2001], which can measure only up to 1 MHz. The low frequency semicircular response (right) becomes more complete and begins to dominate the spectra with increasing temperature. Comparing the diameters of the semicircles in each Cole-Cole plot, it is apparent that the ratio of the low frequency to the high frequency semicircle diameter increases with increase of the temperature. This indicates that impedance from grain boundaries becomes more significant at higher temperatures, i.e., electrical conduction through grain boundaries dominates at temperatures above 250°C.

Theoretically, a double *R-C* parallel circuit model in series [Macdonald 1987] could be used to simulate the electrical conduction of diamond films contributed from both grain interiors and grain boundaries. Each parallel *R-C* equivalent circuit model accurately fits each Cole-Cole semicircle. The fitting procedure used here is the same as the one described by Kleitz and Kennedy [1979] and allows the determination of resistance and relaxation frequencies with a good precision. Here the resistor *R* represents ionic or electronic conduction mechanisms, while the capacitor *C* represents the polarizability of the diamond. The symbols R_{gi}, R_{gb}, C_{gi}, and C_{gb} are defined as before. The complex impedance Z* measured by the RCL meter can be expressed as the following function of the R_{gi}, R_{gb}, C_{gi} and C_{gb} of the specimen:

$$Z^* = Z' - j\,Z'' \tag{8.1}$$

$$Z' = \frac{R_{gi}}{1+\omega^2 R_{gi}^{\ 2} C_{gi}^{\ 2}} + \frac{R_{gb}}{1+\omega^2 R_{gb}^{\ 2} C_{gb}^{\ 2}} \tag{8.2}$$

$$Z'' = \frac{\omega R_{gi}^{\ 2} C_{gi}}{1+\omega^2 R_{gi}^{\ 2} C_{gi}^{\ 2}} + \frac{\omega R_{gb}^{\ 2} C_{gb}}{1+\omega^2 R_{gb}^{\ 2} C_{gb}^{\ 2}} \tag{8.3}$$

where Z' and Z'' represent the real and imaginary portions of the impedance and ω is the angular frequency. When plotted in a complex plane, Z'' versus Z' takes the form of two semicircles. In this representation, the grain interior and grain boundary contributions are easily identified, and the electrical conduction paths of the bulk material can be studied separately from grain boundary interference; this task has been performed above.

As previously mentioned, the diameter of each semicircle indicates the resistance (*R*) contributed either from grain interiors or from grain boundaries. In order to understand the different semicircular response quantitatively, the resistance for the contribution from both grain interiors and grain boundaries was estimated and extracted as shown in table 8.2. R_{gi}, R_{gb}, and R_{gi}/R_{gb} are the

resistance from the grain interior, the resistance from grain boundaries, and the ratio between them. The first observation is that the resistance either from grain interiors or from grain boundaries decreases with increasing temperature. Particular attention should be paid to the strong decrease of diamond grain interior resistance (from 300 to 0.02 kΩ) with increasing of temperature (from 25 to 500°C). The resistance contributed from the grain boundaries is not measurable below 250°C, implying that it is relatively small. Comparison of the relative variation of both resistances shows that the resistance from grain boundaries made more dominant contribution with increasing temperature.

Recent studies of the temperature-dependent resistance of polycrystalline CVD diamond films have shown that the thermal activation energy can cover a wide range between 0.09 eV and 1.5 eV [Jin et al 1994, Nath and Wilson 1996, Hunn et al 1993, Bade et al 1993, Ran et al 1993, Sugino et al 1993, Miyata and Dreifus 1994]. However, the grain interior and grain boundary resistances have not previously been identified and separated. In the field of CVD diamond, it is often difficult to make direct comparisons with a body of published work since films grown in different laboratories can display significantly different properties. Jin et al [1994] have reported activation energy changes from 0.4 to 0.9 eV with increasing temperature. They suggested that the weakly temperature-dependent resistivity at lower temperature was due to leakage along the grain boundaries; however, no directly evidence was presented. The resistance they reported became nearly independent of frequency at the high temperature end, which is consistent with similar observations by Nath and Wilson [1996].

Table 8.2 Temperature dependence of grain boundary resistance (R_{gb}), grain interior resistance (R_{gi}), and the relative resistance (R_{gb}/R_{gi}) between them.

T (°C)	R_{gi} (kΩ)	R_{gb} (kΩ)	R_{gb} / R_{gi}
25	300.00	_	_
100	133.00	_	_
150	71.00	_	_
200	50.00	_	_
250	28.00	_	_
275	14.00	5.20	0.37
300	5.60	3.68	0.66
350	1.00	1.32	1.32
375	0.50	0.80	1.60
400	0.22	0.54	2.45
425	0.11	0.35	3.18
450	0.05*	0.24	4.80*
500	0.02*	0.12	6.00*

8.4.2 Physical Mechanism

A few reports exist that discuss different mechanisms to explain the electrical conduction properties of microcrystalline diamond films, rather than the nanocrystalline diamond films studied here. Landstrass and Ravi [1989] proposed that the conduction transition they observed with temperature was caused by the movement of hydrogen and other defects from electrically active deep levels to nonactive sites during annealing. Mori et al [1992] suggested the existence of a surface conductive layer combined with chemical absorption and oxidation. Werner et al [1993] and Huang et al [1991] have presented space charge limited currents and the Poole-Frenkel mechanism as origin for the non-linear increase of the conduction with temperature. Frequency-independent and frequency-dependent band conduction and hopping conduction

mechanisms have also been discussed [Extance et al 1985]. Some studies have shown that a number of different defects are present within the grain boundaries which influence the conduction and the mobility of the charge carriers [Malta et al 1995 and Fiegl et al 1994].

It is worth noting that nanocrystalline material containing a high density of grain boundaries has a high surface-area-to-volume ratio [Chen et al 1999]. With external heating, the grain boundaries may undergo the deformation and distortion caused by the thermal expansion, thermal stress, and even oxidation. The total area of grain boundaries, where defects and non-diamond carbon phases are believed to be most densely accumulated, can increases enormously [Nistor et al 1997, Hirai et al 1997]. These impurities are not as thermally stable as diamond grains. Diamond crystals begin to oxidize in air at about 500°C and begin to graphitize under vacuum at around 800°C [Sun et al 2000], while impurities at grain boundaries are thermally activated at lower temperatures (250°C), as observed. Therefore, oxidation, diffusion, and space charge transportation can easily take place. An alternative explanation involves the interfaces between the diamond and the electrode, and/or between the diamond and the silicon substrate. If the accumulation and trapping of charges at structural interface reaches a certain value, interfacial or boundary polarization will happen with increasing temperature and will subsequently cause a responding secondary relaxation in the impedance data.

As indicated above, the effect of current conduction through the silicon substrate is assumed to be absent. However, it is interesting to note that the change in activation energy found in the grain interior resistance to a value of 0.67 eV above 250 °C is exactly the same as the activation energy found for the radio frequency losses due to thermal activation of intrinsic charge carriers in silicon (over the band gap) [Heidinger and Kumlin 1991]. Therefore, another possible explanation would be that the contribution of silicon becomes significant over 250 °C.

8.5 Conclusions

Diamond films were synthesized by a microwave plasma enhanced CVD method and characterized using SEM, XRD, and a Fluke RCL meter. The impedance measurement yields the real and imaginary parts in the form of a Cole-Cole plot. In this representation, grain interior and grain boundary contributions are identified and the electrical behaviour of the diamond grains was studied separately from grain boundary interference. A single semicircular response of the electrical conduction was observed at temperatures below 250°C. A secondary semicircular response appears at low frequencies above 250°C. Temperature-dependent resistance measurements show that the activation energy changes from 0.13 to 0.67 eV with increasing temperature. Further investigations will look into the *in situ* observation of grain boundaries using high-resolution TEM with temperature control to provide more direct proof of the physical mechanisms suggested in this paper.

8.6 References

Bade JP, Sahaida SR, Stoner BR, Windheim JA von, Glass JT, Miyata K, Nishimura K and Kobashi K, Diamond Relat. Mater. **2** (1993) 816.

Beckman J, Jackman RB, Foord JS, Diamond Relat. Mater. **3** (1994) 602.

Chandrasekar S and Bhushan B, Wear **153** (1992) 79.

Chen J, Deng SZ, Chen J, Yu ZX and Xu NS, Appl. Phys. Lett. **74** (1999) 3651.

Erz R, Dotter W, Jung D and Ehrhardt H, Diamond Rel. Mater. **2** (1993) 449.

Extance P, Elliott SR and Davis EA, Phys. Rev. **B32** (1985) 8184.

Fedoseev DV, Bukhovets VL, Tolmachev YN, Varshavskaya IG and Kvaskov VB, Diamond Relat. Mater. **2** (1993) 1327.

Fedoseev DV, Bukhovets VL, Varshavskaya IG and Tolmachev YN. Russ. J. Phys. Chem. **70** (1996) 1594.

Fiegl B, Kuhnert R, Ben-Chorin M and Koch F, Appl. Phys. Lett. **65** (1994) 371.

Gruen DM, Annu. Rev. Mater. Sci. **29** (1999) 211

Hayward IP, Surf. Coat. Technol. **49** (1991) 554.

Heidinger R, Kumlin A, Dig. 16th Int. Conf. On Infrared and Millimeter Waves, Lausanne (CH), 26-30 Aug.1991, SPIE Vol.1576, p450.

Hench LL and West JK, Principles of Electronic Ceramics, Wiley, New-York NY, 1989.

Hirai H, Kondo K, Kim M, Koinuma H, Kurashima K and Bando Y, Appl. Phys. Lett. **71** (1997) 3016.

Huang Bohr-ran and Reinhard DK, Appl. Phys. Lett. **59** (1991) 1494.

Hunn JD, Parikh NR, Swanson ML and Zuhr RA, Diamond Relat. Mater. **2** (1993) 847.

Jackman RB, Beckman J and Foord JS, Appl. Phys. Lett. **66** (1995) 1018.

Jiao S, Sumant A, Kirk MA, Gruen DM, Kraus AR and Auciello O, J. Appl. Phys. **90** (2001) 118.

Jin S and Moustakas TD, Diamond Relat. Mater. **2** (1993) 1355.

Jin S, Fanciulli M, Moustakas. TD, Robins LH, Diamond Relat. Mater. **3** (1994) 878.

Khomich AV, Polyakov VI, Perov PI, Varnin VP, Teremetskaya IG, et al. Mater. Res. Soc. Symp. Proc. **423** (1996) 723.

Kleitz M and Kennedy JH, Fast Ion Transport in Solids, Elsevier, North Holland, 1979.

Konov VI, Smolin AA, Ralchenko VG, Pimenov SM, Obraztsova ED, et al. Diamond Rel. Mater. **4** (1995) 1073.

Krauss AR, Auciello O, Ding MQ, Gruen DM, Huang Y, Zhirnov VV, Givargizov EI, Breskin A, Chen R, Shefer E, Konov V, Pimenov S, Karabutov A,

Rakhimov A and Suetin N, J. Appl. Phys. **89** (2001) 2958.

Kundu SN, Basu M, Maity AB, Chaudhuri S and Pal AK. Mater. Lett. **31** (1997) 303.

Landstrass MI and Ravi KV, Appl. Phys. Lett. **55** (1989) 1391.

Lee J, Hong B, Messier R and Collins RW, Appl. Phys. Lett. **69** (1996) 1716.

Macdonald JR, Impedance Spectroscopy, Wiley, New-York NY, 1987.

Malta DM, Windheim JA von, Wynands HA and Fox BA, J. Appl. Phys. **77** (1995) 1536.

Miyata K and Dreifus DL, Jpn. J. Appl. Phys. **33** (1994) 4526.

Mori Y, Eimori N, Hatta A, Ito T and Hiraki A, Jpn. J. Appl. Phys. **31** (1992) L1718.

Nath S and Wilson JIB, Diamond Relat. Mater. **5** (1996) 65.

Nistor LC, Landuyt JV, Ralchenko VG, Obraztsova ED and Smolin AA, Diamond Relat. Mater. **6** (1997) 159.

Nistor LC, Van Landuyt J, Ralchenko VG, Obratzova ED, Korotushenko KG and Smolin AA, Mater. Sci. Forum **239-241** (1997) 115.

Ran JG, Zheng CQ, Ren J and Hong SM, Diamond Relat. Mater. **2** (1993) 793.

Rotter S. Isr. J. Chem. **38** (1998) 135.

Spitzl R, Raiko V and Engemann J, Diamond Relat. Mater. **3** (1994) 1256.

Sugino T, Muto Y, Karasutani K, Shirafuji J and Kobashi K, Diamond Relat. Mater. **2** (1993) 803.

Sun C, Xie H, Zhang W, Ye HT and Hing P, J. Phys. D **33** (2000) 2196.

Swain GM, Anderson AB and Angus J, *MRS Bull.* **99** (1998) 5616.

Werner M, Dorsch O, Hinze A, Obermeier E, Harper RE, Johnston C, Chalker PR and Buckley-Golder IM, Diamond Relat. Mater. **2** (1993) 825.

Ye HT, Sun C, Huang H and Hing P, Appl. Phys. Lett. **78** (2001) 1826.

Ye HT, Sun C, Huang H and Hing P, Thin Solid Films **381** (2001) 52.

Zarrabian M, Fourches-Coulon N, Turban G, Marhic C and Lancin M, Appl. Phys. Lett. **70** (1997) 2535.

Zhou D, Gruen DM, Qin LC, McCauley TG and Krauss AR, J. Appl. Phys. **84** (1998) 1981.

Zhou D, McCauley TG, Qin LC, Krauss AR and Gruen DM, J. Appl. Phys. **83** (1998) 540.

Zhu W, McCune RC, deVries JE, Tamor MA and Ng KYS, Diamond Relat. Mater. **3** (1994) 1270.

Chapter 9

Ultrananocrystalline Diamond

9.1 Introduction

Nanocrystalline diamond films have emerged as potentially revolutionary materials for various applications as discussed in chapter 8. For the past few years, Argonne National Laboratory (ANL) has reported the growth and characterization of ultrananocrystalline diamond (UNCD) films using microwave plasma enhanced chemical vapor deposition [Zhou et al 1997, Gruen 1999, Krauss et al 2001]. UNCD films arise from the self-assembly of C_2 dimers on appropriate substrates. The C_2 growth species are created using hydrogen poor plasmas using either C_{60} or CH_4 as the carbon source [Gruen 1993, Gruen et al 1994]. UNCD films consist of 2–5 nm diamond grains and 0.5 nm-wide high-energy grain boundaries and exhibit interesting properties including enhanced filed emission, electrochemical, mechanical, tribological, and conformal coating properties, which are the result of their unique nanoscale morphology and electronic structure [Qin et al 1998]. UNCD films were deposited by microwave plasma enhanced chemical vapor deposition method using a $CH_4/Ar/N_2$ gas mixture. It has been reported that the electrical conductivity of the nitrogen doped UNCD films increases by five orders of magnitude with increasing nitrogen content [Bhattacharyya et al 2001]. Conductivity and Hall measurements made as a function of temperature down to 4.2K indicate that these films have the highest n-type conductivity and carrier concentration demonstrated for phase-pure diamond films. It is proposed that grain boundary conduction be responsible for the remarkable transport properties of these films [Bhattacharyya et al 2001]. However, no direct experimental evidence is available to support such a proposal. Impedance spectroscopy is a technique that allows the identification of electrical conduction paths within polycrystalline materials and their attribution to grain interiors, grain boundaries, and electrodes. Details have been illustrated in previous chapters. This chapter presents new results on how grain boundaries and/or grain interiors conduction dominate within UNCD films using impedance spectroscopy. It provides a better understanding of the insights of the conduction mechanism within UNCD films.

9.2 Experimental Details

The UNCD samples studied here were produced using a microwave plasma enhanced CVD system by Gruen's group at ANL. The nominal gas composition for MPECVD system was 1% CH_4 and 99% Ar. As nitrogen was added to the gas mixture, the relative partial pressure of Ar was reduced, so that when 20% N_2 is added, the exact gas composition is 1% CH_4, 79% Ar, and 20% N_2. A set of samples (I, II, III and IV) were used in this chapter. The details of the gas reactants are shown in table 9.1. Other growth parameters have been illustrated in details elsewhere [Bhattacharyya et al 2001].

Sample	Reactant gas content		
	N_2	CH_4	Ar
(I)	0%	1%	99%
(II)	5%	1%	94%
(III)	10%	1%	89%
(IV)	20%	1%	79%

Table 9.1 Reactant gas composition in the plasma for UNCD samples (I), (II), (III) and (IV).

The films were grown on Ib (100) highly insulating HPHT diamond in ANL, which had been rigorously cleaned in an acid solution [Birrell et al 2002]. Prior to the impedance measurements, growth surfaces of the samples were coated with silver paste to form the electrodes, following by annealing in air at 350°C for 2 minutes to ensure electrode stability [Ye et al 2002]. All the samples have the same geometric shape with a size of 2X2X1mm^3. The effect of current flow through the Ib diamond substrate on the measured resistance was ignored due to the perfect insulating properties of this type of diamond. The impedance properties of the UNCD films were determined in the frequency range between 0.1 Hz and 10 MHz over a temperature range of 25-350°C in a vacuum of 10^{-2}

Torr. The set-up parameters are 0.05 volt of AC amplitude, 1 second integration time, and no delay time.

High-resolution transmission electron microscopy (HRTEM) and electron energy-loss spectroscopy (EELS) were used to investigate the variation of morphology and bonding in the grains and grain boundaries of UNCN films grown with different amounts of nitrogen added into the gas reactants in ANL. HRTEM samples were prepared via mechanical polishing followed by ion milling at grazing incidence angles. HRTEM was performed using a JEOL 4000EX microscope at 400 kV. EELS was performed using a JEOL 2010F scanning transmission electron microscope with a Gatan 666 parallel EELS detector operated at 200 kV. HRTEM was chosen to assay the changes in nanoscale morphology in these films because conventional dark-field techniques have some difficulties with grain overlap when measuring grains as small as those of UNCD (2-16nm).

9.3 Experimental Results

9.3.1 Characterization of Film Quality

Representative examples of high-resolution images are shown in figure 9.1. The average grain size was determined by measuring the extent of the lattice fringes seen in the HRTEM images. This was done for UNCD samples (I) to (IV). The HRTEM micrographs shown in figure 9.1 (a)-(d) indicate that nitrogen mixture within the reactants has a profound effect on the nanostructure of UNCD. Note that each of these images in figure 9.1 has the same scale, and also the clear presence of lattice fringes in each image on the right. Insets in figure 9.1 are the electron diffraction patterns. Clearly, all the UNCD films shown here consist of both grains and grain boundaries morphology, with both the grain size and grain boundary width increasing with nitrogen concentration. The size of the grains gradually increases from about 4 to 16 nm, as the nitrogen content in the plasma is changed from 0% to

20%. The grain-boundary width increases as well, from about 0.5 to 2.2 nm [Birrell et al 2002].

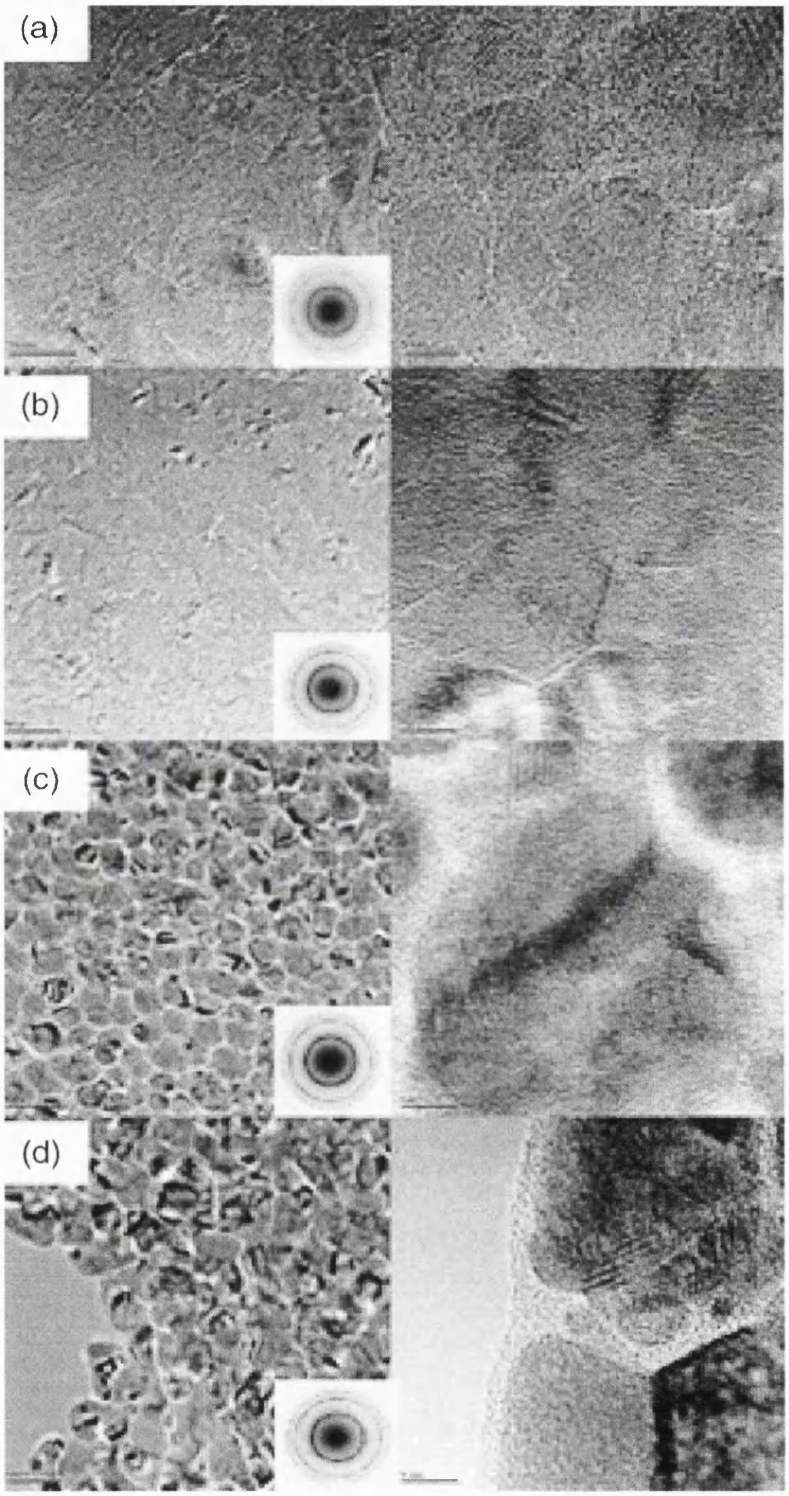

Figure 9.1. Low- and high-resolution TEM micrographs of UNCD: (a) sample I, (b) sample II, (c) sample III and (d) sample IV. Low-resolution micrographs are on the left, high resolution on the right. Figures are scaled so that the low-resolution micrographs are 350 nm by 350 nm and the high-resolution ones are 35 nm by 35 nm. (Reprinted from Birrell et al 2002).

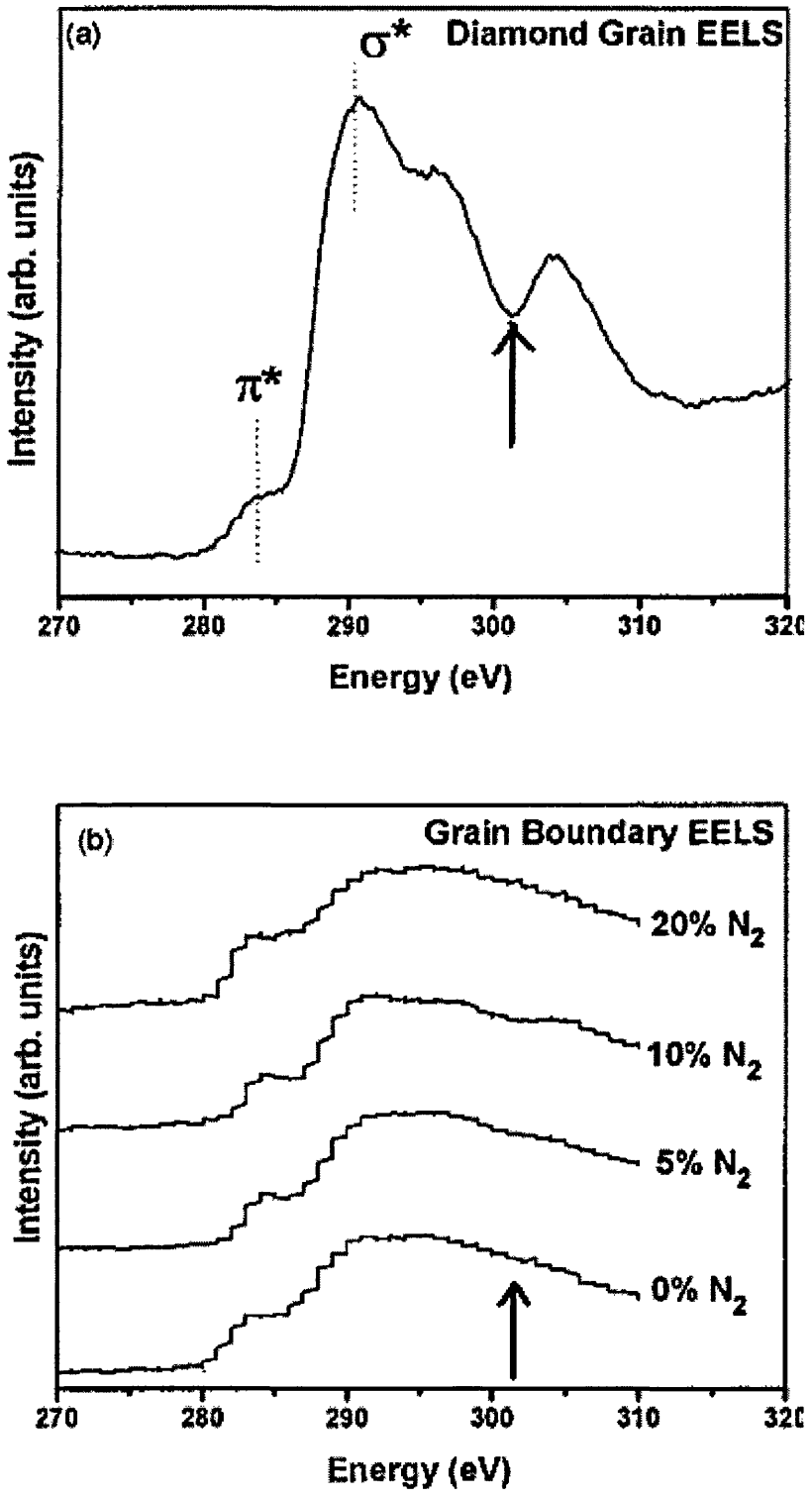

Figure 9.2. EELS spectra using an electron nanoprobe of (a) an individual representative UNCD grain, and (b) from a series of nitrogen-doped UNCD thin films. The energy of the $\pi^*(\sigma^*)$ conduction-band states for sp^2 (sp^3)-bonded carbon are shown by the dashed lines. The arrow marks the energy position of the second band gap in diamond, which is clearly present in the grains and absent in the grain boundaries. (Reprinted from Birrell et al 2002).

To assess the atomic origins of the *sp*2 bonding in these films, small-spot EELS measurements were used to compare the bonding structure in the diamond grains and the grain boundaries in a series of films grown with an increasing amount of nitrogen in the plasma. Figure 9.2 (a) shows a typical EELS spectrum with the electron beam positioned on one UNCD grain, indicating that it is phase pure diamond for all nitrogen doping levels, as evidenced by the near-edge electronic structure of the peak. The well-defined absorption edge at 289.5 eV and the presence of the second band-gap feature clearly shows that the diamond grains are sp^3-bonded carbon atoms with a high degree of short-range ordering [Coffman et al 1996]. This does not change as nitrogen is added to the plasma, showing that there is no change in the electronic structure within the grains. The grain boundary spectra in figure 9.2 (b) show a very slight variation as nitrogen is incorporated into the plasma. Specifically, the π^* peak at 285 eV increases slightly when nitrogen is incorporated into the UNCD film. The σ^* feature that peaks at ~289 eV, which is associated with sp^3 bonding [Gruen et al 1996], is unchanged. The relative intensities of the sp^2 versus sp^3 peaks in the spectra of figure 9.2 (b) indicate that the amount of sp^2 bonding increases only slightly within the grain boundaries when nitrogen is added to the plasma. This indicates that the level of sp^2 bonding within the grain boundaries remains relatively unchanged as nitrogen is incorporated into UNCD. It is therefore concluded that the increase in sp^2 content in the film as a whole is derived from a slight increase in grain-boundary area in the film, and not a change in the local bonding structure within the grains or grain boundaries [Birrell et al 2002].

9.3.2 *Characterization of Electrical Behaviour*

Impedance spectroscopy is a powerful technique for investigating the electrical properties of polycrystalline materials, being capable of isolating processes within the grains and grain boundary regions [Macdonald 1987]. In the preceding chapters, this technique was used to investigate the conduction

mechanisms for single crystalline, microcrystalline, and nanocrystalline diamond films. In this chapter, the first data for UNCD are presented.

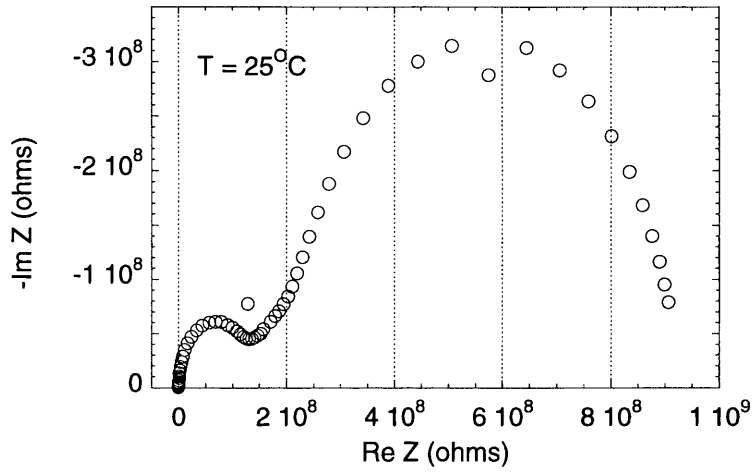

(a) UNCD sample (I) at 25°C

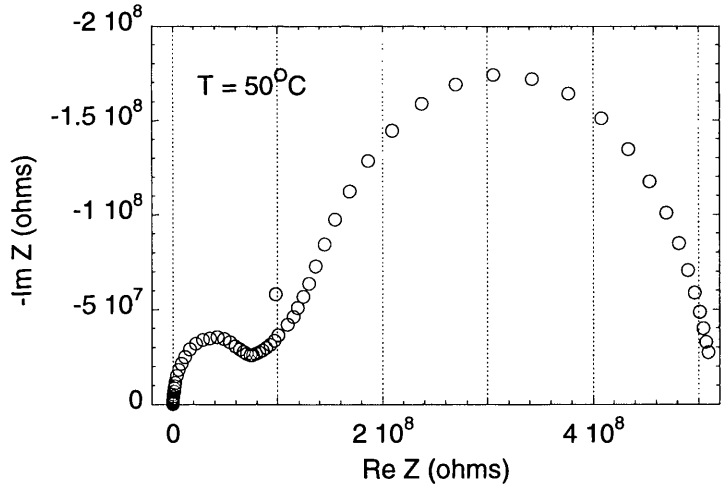

(b) UNCD sample (I) at 50°C

Figure 9.3 Impedance spectroscopy of UNCD sample (I) without nitrogen in the plasma: (a) 25°C, (b) 50°C, (c) 100°C, (d) 150°C, (e) 200°C, (f) 250°C, (g) 300°C and (h) 350°C. (continued on next page)

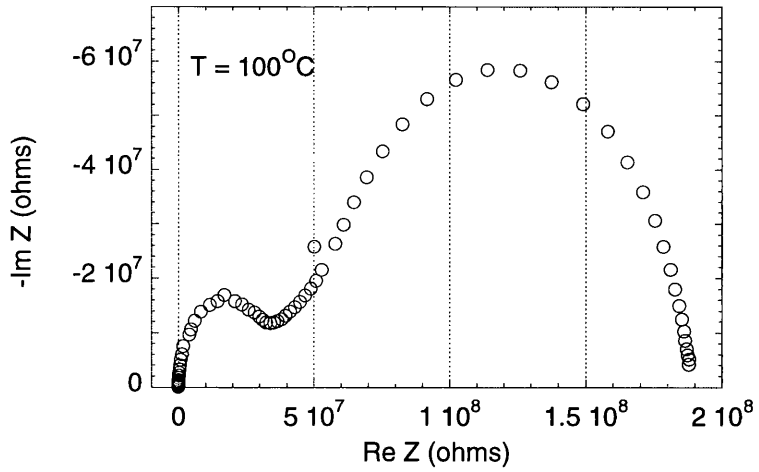

(c) UNCD sample (I) at 100°C

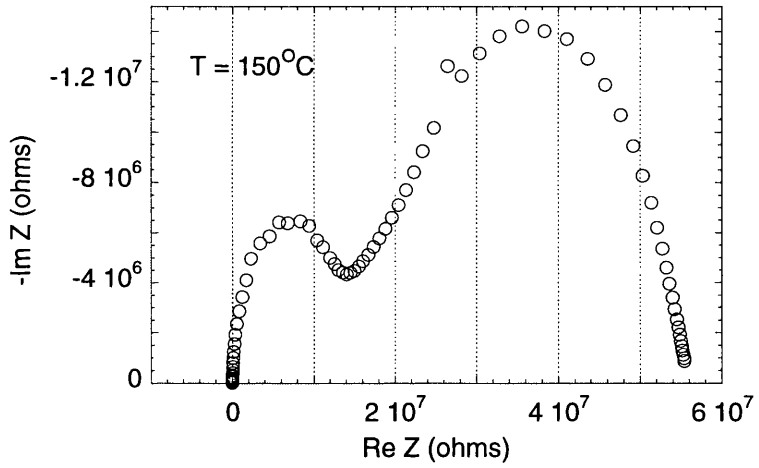

(d) UNCD sample (I) at 150°C

Figure 9.3 Impedance spectroscopy of UNCD sample (I) without nitrogen in the plasma: (a) 25°C, (b) 50°C, (c) 100°C, (d) 150°C, (e) 200°C, (f) 250°C, (g) 300°C and (h) 350°C. (continued on next page)

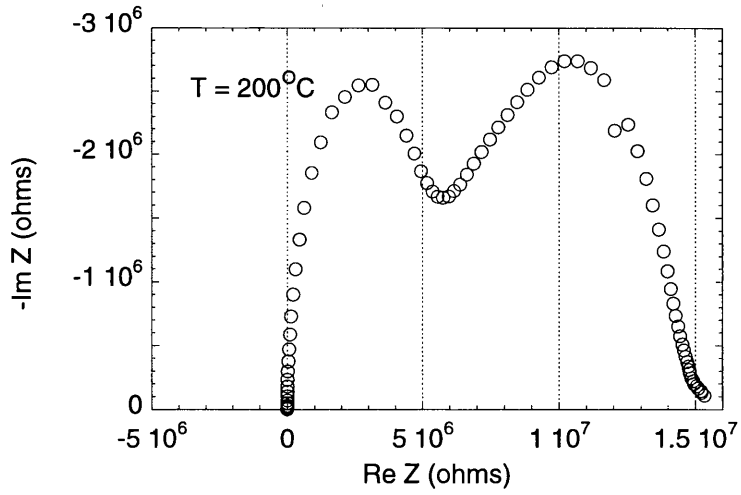

(e) UNCD sample (I) at 200°C

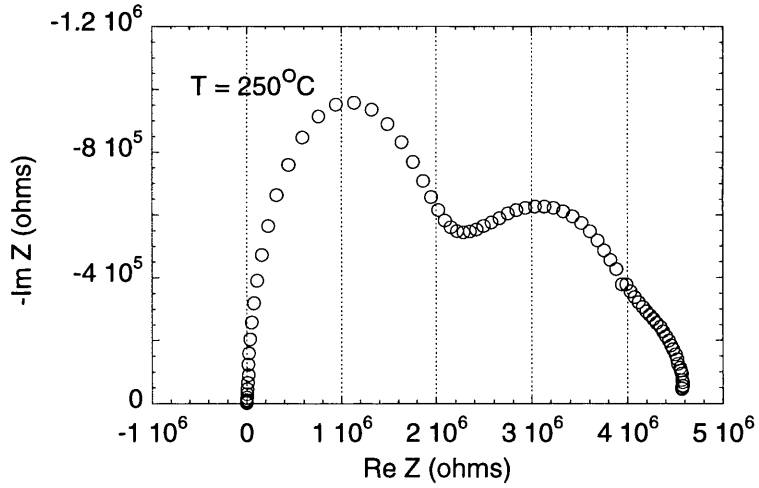

(f) UNCD sample (I) at 250°C

Figure 9.3 Impedance spectroscopy of UNCD sample (I) without nitrogen in the plasma: (a) 25°C, (b) 50°C, (c) 100°C, (d) 150°C, (e) 200°C, (f) 250°C, (g) 300°C and (h) 350°C. (continued on next page)

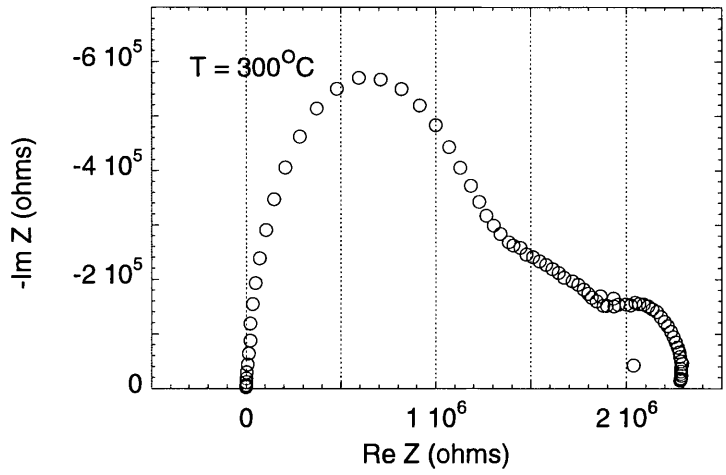

(g) UNCD sample (I) at 300°C

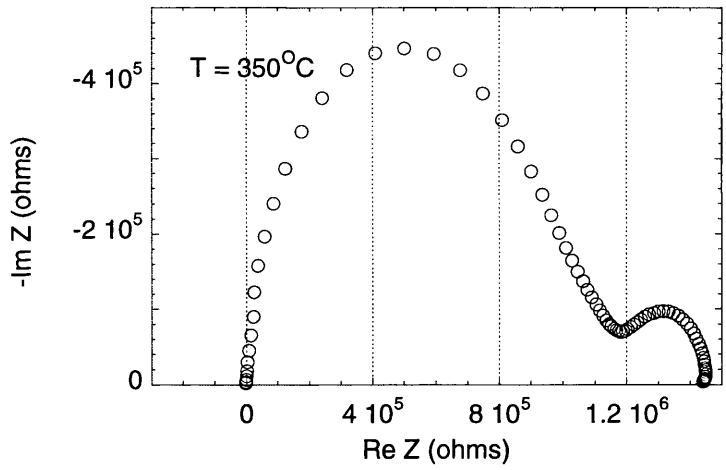

(h) UNCD sample (I) at 350°C

Figure 9.3 Impedance spectroscopy of UNCD sample (I) without nitrogen in the plasma: (a) 25°C, (b) 50°C, (c) 100°C, (d) 150°C, (e) 200°C, (f) 250°C, (g) 300°C and (h) 350°C.

The temperature dependence of the characteristic Cole-Cole plots measured for UNCD sample (I) without nitrogen addition into the plasma is shown in figure 9.3. At 25°C, the Cole-Cole plot has two semicircular responses as shown in figure 3(a). The resistance and capacitance value for each semicircle can be obtained by fitting each curve or arc based on a single R-C

parallel equivalent circuit. The fitting details have been illustrated in chapter 3. The fitted resistance and capacitance values are shown in table 9.2. It is found that at 25°C, the left small semicircle has a resistance of 138 MΩ and a capacitance of 0.92 pF. The right large semicircle has a resistance of 743 MΩ and a capacitance of 0.2 nF. The semicircle on the left (high frequency and capacitance value in the pF range) is assigned to the electrical behaviour within the grain interior, whilst the other on the right (low frequency and capacitance value in the nF range) is assigned to the contribution of the grain boundary. Thus at 25°C, sample (I) has an overall resistance (R_{GI}+R_{GB}) of around 900 MΩ, to which around 138MΩ is contributed from the grain interiors and around 743 MΩ is from grain boundaries. The relative resistance ratio (R_{GI}/R_{GB}) between grain interiors and grain boundaries is 0.186.

By repeating these measurements for increasing temperature up to 350°C, similar Cole-Cole plots for the same sample were obtained as shown in figure 9.3 (b)-(h). Two distinct semicircles can be observed at all temperatures. With increasing temperature, the magnitude order of the X-axis decreases significantly from 10^9Ω at 25°C to 10^6 Ω at 350°C. All the fitted resistance and capacitance values in the measured temperature range are listed in table 9.2. It is found that at 350°C, the left semicircle appears to be larger than the right. The left semicircle corresponding to the contribution from grain interiors has a resistance of 967 kΩ and a capacitance of 0.82 pF. In contrast, the right semicircle corresponding to the contribution from grain boundaries has become smaller. It has a resistance of 271 kΩ and a capacitance of 0.2 nF. The relative resistance ratio between grain interiors and grain boundaries at 350°C is 3.568, i.e., 20 times more than that at 25°C. Therefore, the dominating conduction path has now changed to grain boundaries.

Qualitatively, the general transition and trend of the Cole-Cole plots versus temperature can be summarized as follows: (1) with increasing temperature, both the grain interior and grain boundary resistance decrease,

hence the overall resistance decreases; (2) the relative resistance ratio between grain interiors and grain boundaries increases with increasing the temperature. This indicates that at low temperatures the conduction process is dominated by the grain interiors. However, at high temperatures, it is dominated by the grain boundaries, which means that most of the current is flowing through the grain boundaries regions. Thus the dominant conduction path gradually transits from grain interiors to grain boundaries while heating up.

A behaviour which is similar to the one discussed above for sample (I) is observed for sample (II) with 5% nitrogen content in the gas reactants. Two distinct semicircles or one semicircle and one arc can be observed at all temperatures for sample (II). For the sake of simplicity and convenience, only impedance data at low temperature (25°C) and high temperature (350°C) are shown here in figure 9.4. At 25°C, the left small semicircle has a resistance of 51 kΩ and a capacitance of 1.21 pF. The right large semicircle has a resistance of 315 kΩ and a capacitance of 0.15 nF. The relative resistance ratio between grain interiors and grain boundaries is 0.162. Thus at 25°C, sample (II) has an overall resistance of around 366 kΩ, to which around 51 kΩ is contributed from the grain interiors and around 315 kΩ from grain boundaries. At 350°C, interesting data are observed in the high frequency range. The left semicircle transits from a semicircle to an arc. This is due to the limitation of the equipment, which can only measure frequencies from 50-10MHz [Miyata and Dreifus 1994]. The left arc has a resistance of 6486 Ω and a capacitance of 3.39 pF. The right semicircle has a resistance of 5589 Ω and a capacitance of 0.07 nF. The relative resistance ratio between the grain interiors and grain boundaries at 350°C is 1.16, i.e., 7 times more than that at 25°C.

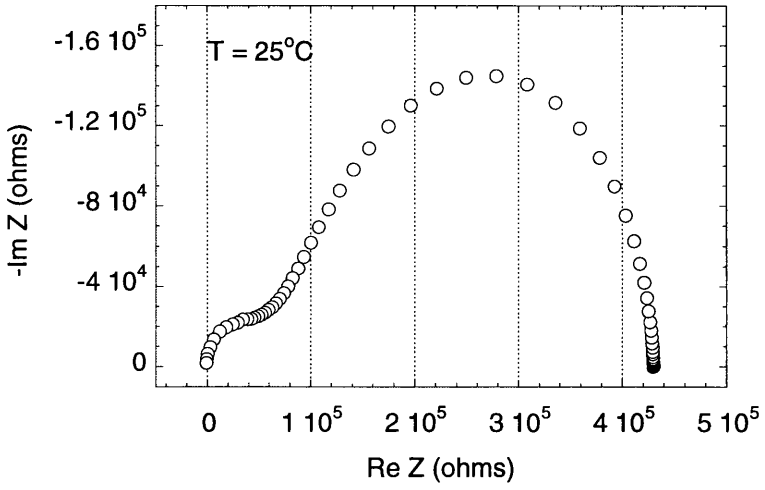

(a) UNCD sample (II) at 25°C

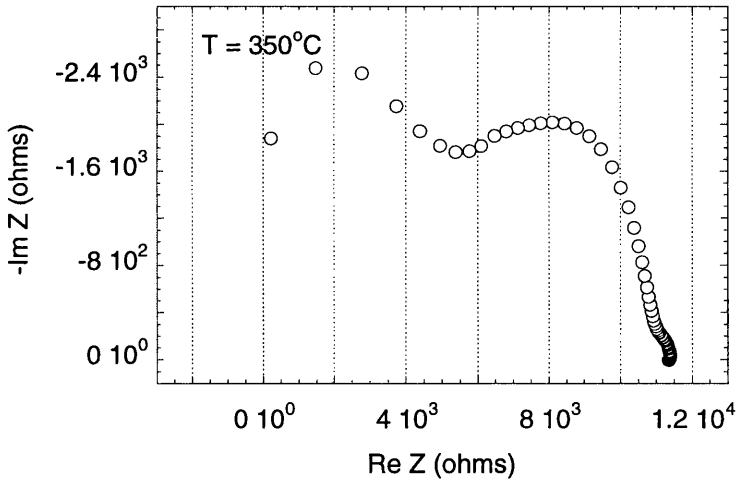

(b) UNCD sample (II) at 350°C

Figure 9.4 Impedance spectroscopy of UNCD sample (II) with 5% nitrogen content in the plasma: (a) 25 °C and (b) 350°C.

For sample (III), the left semicircle almost disappears as shown in figure 9.5. This indicates that the resistance values associated with the grain interiors are approaching zero. However, the contributions from the grain boundaries are shown on the right semicircles. The fitted resistance and capacitance values for the grain boundary contribution are listed in table 9.2. The resistance value

decreases from 6486 Ω at 25°C to 1916 Ω at 320 °C. The capacitance value is maintained in the nF range, which suggests grain boundaries dominate the conduction process as the signal from grain interior is too small to be measured.

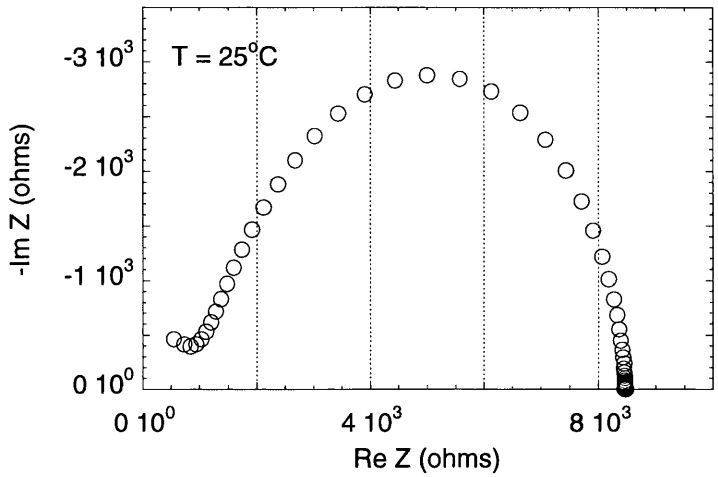

(a) UNCD sample (III) at 25°C

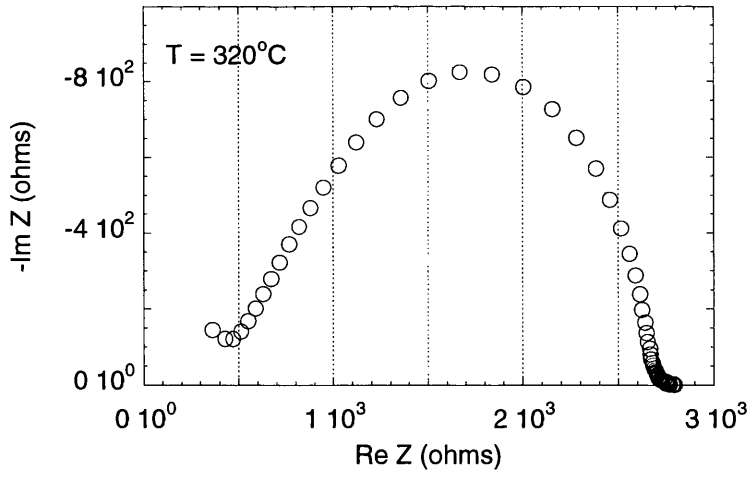

(b) UNCD sample (III) at 320°C

Figure 9.5 Impedance spectroscopy of UNCD sample (III) with 10% nitrogen content in the plasma: (a) 25 °C and (b) 320°C.

Impedance data for sample (IV) are not available. This is because sample (IV) with 20% nitrogen in the reactants behaves like a metallic conductor. The measurement of impedance for a conductive material has gone beyond the limitation of the equipment itself.

Sample	T (°C)	R_{GI} (Ω)	C_{GI} (pF)	R_{GB} (Ω)	C_{GB} (nF)	R_{GI}/R_{GB}
(I)	25	138000000	0.92	743000000	0.20	0.186
	50	79300000	0.89	401000000	0.21	0.198
	100	35000000	0.94	140000000	0.20	0.25
	150	13400000	0.93	38700000	0.21	0.346
	200	5660000	0.95	9070000	0.13	0.624
	250	2020000	0.95	2780000	0.10	0.727
	300	1270000	0.99	370000	0.32	3.432
	350	967000	0.82	271000	0.20	3.568
(II)	25	50881	1.21	315000	0.15	0.162
	50	42066	1.50	235000	0.15	0.179
	100	28481	1.71	118000	0.17	0.241
	150	18640	2.11	54430	0.17	0.342
	200	12558	2.51	29441	0.12	0.427
	250	9448	3.32	13652	0.17	0.692
	300	7620	3.23	7776	0.16	0.98
	350	6486	3.39	5589	0.07	1.16
(III)	25	0	-	6486	0.27	-
	50	0	-	5309	0.29	-
	100	0	-	5704	0.47	-
	150	0	-	10307	0.58	-
	200	0	-	10416	0.58	-
	250	0	-	5834	0.59	-
	300	0	-	2706	0.58	-
	320	0	-	1916	0.55	-
(IV)	Metallic					

Table 9.2 Temperature dependence of grain interior and grain boundary resistance and capacitance values of UNCD samples (I), (II), (III) and (IV).

9.4 Discussion

The fitted resistance and capacitance values for samples (I)-(IV) at all temperatures are summarised in table 9.2. Here the resistor R represents ionic or electronic conduction mechanisms, while the capacitor C represents the polarizability of UNCD films. The symbols R_{GI}, R_{GB}, C_{GI}, and C_{GB} within the

equivalent double *R*-*C* parallel circuit are defined as the resistance and capacitance values from grain interiors and grain boundaries of UNCD films. The measured complex impedance Z^* can be expressed as the following function of the R_{GI}, R_{GB}, C_{GI} and C_{GB} of the specimen:

$$Z^* = Z' - j\,Z'' \tag{9.1}$$

$$Z' = \frac{R_{GI}}{1+\omega^2 R_{GI}^{\ 2} C_{GI}^{\ 2}} + \frac{R_{GB}}{1+\omega^2 R_{GB}^{\ 2} C_{GB}^{\ 2}} \tag{9.2}$$

$$Z'' = \frac{\omega R_{GI}^{\ 2} C_{GI}}{1+\omega^2 R_{GI}^{\ 2} C_{GI}^{\ 2}} + \frac{\omega R_{GB}^{\ 2} C_{GB}}{1+\omega^2 R_{GB}^{\ 2} C_{GB}^{\ 2}} \tag{9.3}$$

where Z' and Z'' represent the real and imaginary parts of the impedance and ω is the angular frequency. When plotted in a complex plane, Z'' via Z' takes the form of two semicircles. In this representation, grain interior and grain boundary contributions are easily identified and the electrical conduction paths of the bulk material can be studied separately from grain boundary interference.

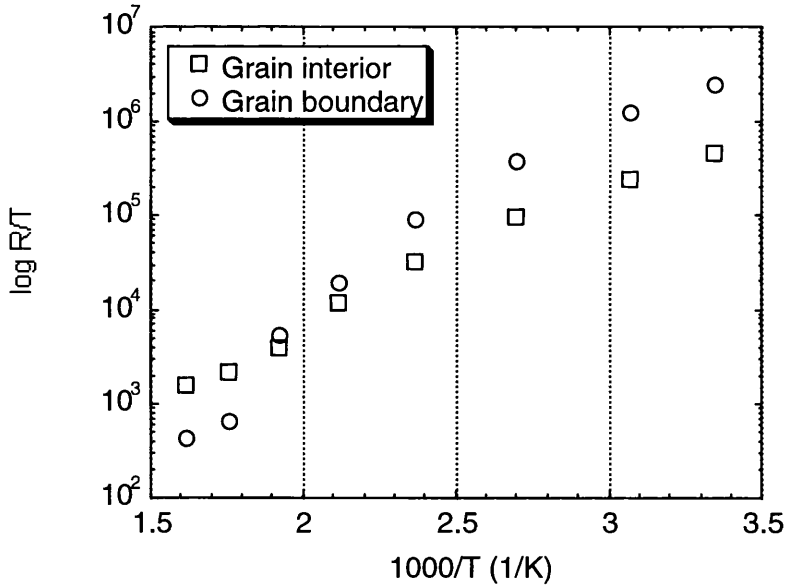

(a) Arrhenius plot for UNCD sample (I)

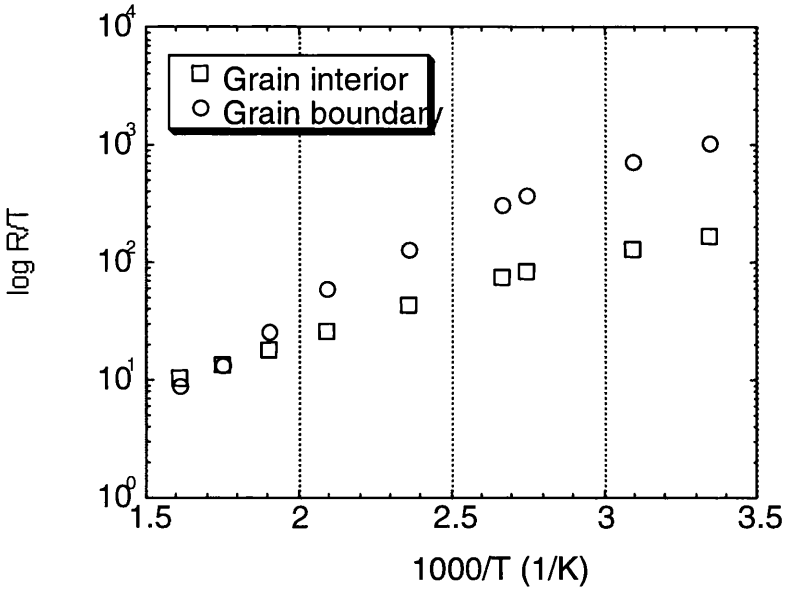

(b) Arrhenius plot for UNCD sample (II)

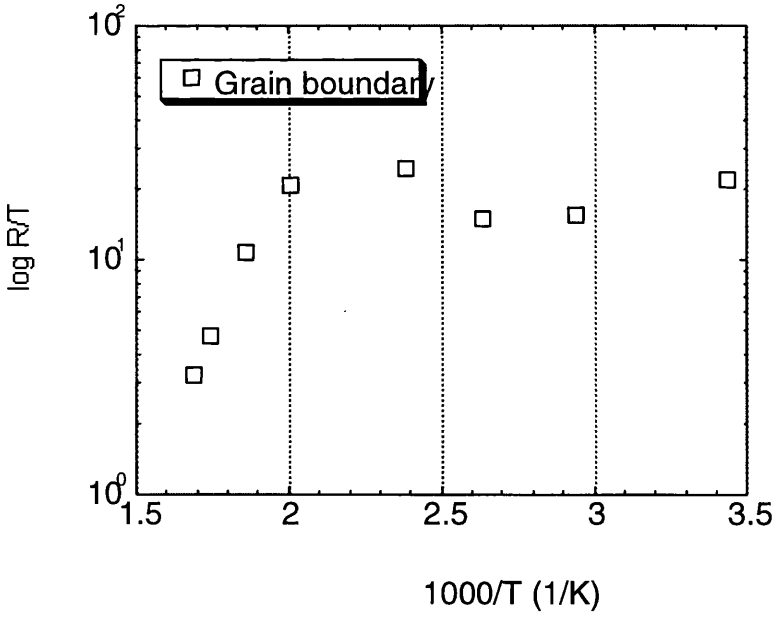

(c) Arrhenius plot for UNCD sample (III)

Figure 9.6 Arrhenius plots of samples (I), (II) and (III). Unit for Y-axis is Ω/K.

In order to gain insight into the impedance results of the UNCD films, Arrhenius plots based on table 9.2 for all the measured samples are shown in figure 9.6. For samples (I) and (II), linear fittings for both grain interior and grain boundary contributions are obtained as shown in figure 9.6 (a)-(b). Their corresponding activation energy can be deduced from such curve fittings as shown in table 9.3. Sample (I) has an activation energy of 0.615eV for grain boundaries and an activation energy of 0.292eV for grain interiors. Sample (II) has an activation energy of 0.316eV for grain boundaries and an activation energy of 0.134eV for grain interiors. Impedance data for sample (III) suggests that the contribution from grain interior could be ignored and grain boundary become dominant in determining the electrical behaviour of the sample. This can be explained using the brick-layer model (see chapter 3) as depicted below. For sample (III), the diamond grains become conductive bricks. The grain boundaries closely surround the grains. Thus the width and connectivity of grain boundaries may play a dominant role in the electrical conduction. From section 9.3.1, it is already known that grain boundary width increases with the increase of the nitrogen concentration in the reactants. Once the grain boundary area forms a continuous network, where all the metallic grains embedded, the grain boundaries are the only electronic barriers. Thus the overall electrical performance will be determined by grain boundary itself. The activation energy for the grain interiors calculated from the Hall measurement is around 0.01eV [Williams et al 2004]. This indicates the weakly temperature dependent resistance due to the nearly metallic characteristics. Also, the Arrhenius plot for grain boundaries of sample (III) is clearly not a simple straight line, which is indicative of multiple thermally activated conduction mechanisms. These data can be modelled and an approximate activation energy for the grain boundaries is around 0.21eV.

It can be summarised by comparing the data in table 9.2 as follows. With increasing temperature, both the grain interior and grain boundary resistance values decrease, hence the overall resistance decreases, but the associated capacitance in both regions remains mostly unchanged. It is worth noting that nanocrystalline material containing many fine grain boundaries has a high surface-area-to-volume ratio [Chen et al, 1999]. With external heating, the grain boundaries undergo the reversible thermal processes such as distortion and deformation or non-reversible processes such as oxidation, and relaxation caused by dislocation formation and migration. The total area of grain boundaries, where defects and non-diamond carbon phases are believed to be accumulated, increases enormously [Nistor et al (1997), Hirai et al (1997)]. These impurities located at grain boundaries such as amorphous carbon, dislocation, point defects et al, are not as thermally stable as diamond grains. They are expected to release some free carriers, upon heating due to thermally activated processes.

Furthermore, the activation energy for the resistance of UNCD samples (I)-(IV) within the temperature range from 25°C to 350°C is calculated and shown in table 9.3. It is found that the activation energy from grain boundaries is always higher than that from grain interiors within the same material. This can be explained by the grain boundary induced double Schottky barrier as shown figure 9.7. UNCD films contain many fine diamond grains. These grains make contact with each other through the grain boundary areas if the connectivity of the grain boundaries is sufficient. Such double barriers arise from the flow of electrons from n-type diamond grains into grain boundary defective areas, setting up a double-layer barrier with the grain positive [Bube 1960]. In this case, the presence of the barrier prevents the free flow of carriers. Thus it causes the activation energy from grain boundaries to be always higher than that from grain interiors.

Sample	E_{GB} (meV)	E_{GI} (meV)
(I)	615	292
(II)	316	134
(III)	210 (a)	10 (b)
(IV)	Metallic	metallic

Table 9.3 Activation energy for the resistance of UNCD samples between room temperature and 350°C. (a) Estimated data, (b) Obtained from Hall Measurements.

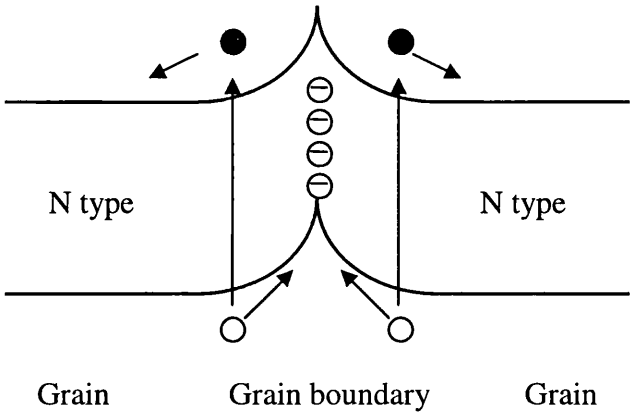

Figure 9.7 Energy-level representation of grain boundary induced double Schottky barrier. Showing the barriers arise from the flow of electrons from n-type diamond grains into grain boundary defective area, setting up a double-layer barrier with the grain positive [Bube 1960].

The data presented in table 9.3 also implies the impurity band conduction process within the UNCD samples for the grain interiors. This has been studied in doped single crystalline and polycrystalline diamond [Okano et al 1996]. In a lightly doped semiconductor with shallow impurities, the donors are essentially isolated and the system is simply a collection of non-interacting impurities with localised states below the conduction band. As the donor density increases, the average separation between donors increases, and interactions between them begin to play a role. If in addition the material is

compensated, the disorder that arises is of two kinds: one caused by completely random positioning of the donors and the other from the ionised acceptors acting as Coulomb centres, there will be some donors that are much closer than the average and the effect of the second is an increase in the spread of the energies, i.e., bandwidth [Mavroidis 2003]. One of the major effects of impurity interactions is that the individual wavefunction of an electron occupying an impurity level, starts to overlap with the wavefunctions of nearby impurities. This in turn leads to the phenomenon of impurity band conduction. Impurity conduction can only occur if the material has a certain number of compensating acceptors that will remove electrons from the impurity band, creating empty states therefore allowing the tunnelling of electrons from occupied to empty donor states.

The activation energy values for UNCD samples (I)-(III) are 0.292eV, 0.134eV and 0.01eV. Sample (IV) becomes metallic. This impurity band starting from 0.292eV expands with increasing nitrogen content until it begins to merge with the conduction band. It will result in the impurity energy decreases with the increasing impurity concentration. Although the impurity concentration is not measured, it is generally believed that the value should be proportional to the nitrogen component in the gas reactants. Therefore impurity band conduction might be responsible for the dramatic decrease of the activation energy with increasing nitrogen content until the grain interior becomes metallic. Edwards and Sienko [1978] assembled a large set of experimental data and present an equation to predict the critical impurity concentration at which impurity band conduction occurs:

$$N_{cr}^{1/3}\alpha_H = 0.3 \qquad (9.4)$$

where N_{cr} is the critical impurity concentration, α_H is the effective Bohr radius in a hydrogen-like impurity. Using the electron effective mass of diamond, m^*

=0.2 m_o and the static dielectric constant, ε_s = 5.7 [Sze 1981], we can obtain the effective Bohr radius as follows:

$$\alpha_H = \frac{4\pi\varepsilon_s\varepsilon_o\eta^2}{q^2 m^*} = 0.529\frac{\varepsilon_s}{m^*}\ (\text{Å}) \qquad (9.5)$$

which yields, $\alpha_H \approx 15$ Å, and by using equation (9.4), a critical concentration of $N_{cr} = 0.8\times10^{19}$ cm^{-3} is obtained. This impurity concentration based on the impurity band conduction mechanism is consistent with the value reported from Hall Measurements [Bhattacharyya et al 2001].

9.5 Conclusions

Impedance spectroscopy has been used to characterize the UNCD films with different nitrogen content in the gas reactants from 25°C to 350°C for the first time. With increasing temperature, both the grain interior and grain boundary resistance decrease, hence the overall resistance decreases. Relative resistance ratio between grain interiors and grain boundaries increases with increasing the temperature. This indicates that the conduction is dominated by the grain interiors at low temperatures and by the grain boundaries at high temperatures. The activation energy for grain boundaries is always higher than that for grain interiors, which might be assigned to the grain boundary induced double Schottky barrier. Impurity band conduction might be responsible for the transition of UNCD films from insulator to conductor with increasing nitrogen concentration. The critical impurity concentration is calculated to be 0.8×10^{19} cm^{-3}, which has a good agreement with literature.

9.6 References

Baral B, Chan SSM and Jackman RB, J. Vac. Sci. Techonol. **A 14** (1996) 2303.

Bhattacharyya S, Auciello O, Birrel J, Carlisle JA, Curtiss LA, Goyette AN, Gruen DM, Krauss AR, Schlueter J, Sumant A and Zapol P, Appl. Phys. Lett. **79** (2001) 1441.

Birrell J, Carlise JA, Auciello O, Gruen DM and Gibson JM, Appl. Phys. Lett. **81** (2002) 2235.

Birrell J, Gerbi JE, Auciello O, Gibson JM, Gruen DM and Carlise JA, J. Appl. Phys. **93** (2003) 5606.

Bube RH, Photoconductivity of Solids, John Wiley &Sons, Inc. (1960) New York.

Chen J, Deng SZ, Chen J, Yu ZX and Xu NS, Appl. Phys. Lett. **74** (1999) 3651.

Coffman FL, Cao R, Pianetta PA, Kapoor S, Kelly M and Terminello L, Appl. Phys. Lett. **69** (1996) 568.

Edwards PP and Sienko MJ, Phys. Rev. B **17** (1978) 2575.

Fausett B, Granger MC, Hupert ML, Wang J, Swain GM and Gruen DM, Electranalysis **12** (2000) 7.

Gerbi JE, Auciello O, Birrell J, Gruen DM, Alphenaar BW and Carlise JA, Appl. Phys. Lett. **83** (2003) 2001.

Gruen DM, Krauss AR, Csencsits R, Zuiker CD, Carlisle JA, Jimenez I, Sutherland DGJ, Terminello LJ, Shuh DK, Tong W and Himpsel FJ, Appl. Phys. Lett. **68** (1996) 1640.

Gruen DM, Annu. Rev. Mater. Sci. **29** (1999) 211.

Gruen DM, Liu S, Krauss AR, Luo J and Pan X, Appl. Phys. Letts. **64** (1994) 1502.

Gruen DM, Nucl. Instr. Methods Phys. Res. **B 78** (1993) 118.

Hench LL and West JK, Principles of Electronic Ceramics, Wiley, New-York NY, 1989.

Hirai H, Kondo K, Kim M, Koinuma H, Kurashima K and Bando Y, Appl. Phys. Lett. **71** (1997) 3016.

Kleitz M and Kennedy JH, Fast Ion Transport in Solids, Elsevier, North Holland, 1979.

Krauss AR, Auciello O, Gruen DM, Jayatissa A, Sumant A, Tucek J, Mancini DC, Moldovan N, Erdemir A, Ersoy D, Gardos MN, Busmann HG, Meyer EM and Ding MQ, Diamond Rel. Mater. **10** (2001) 1952.

Macdonald JR, Impedance Spectroscopy, Wiley, New-York NY, 1987.

Mavroidis C, PhD thesis, University of London 2003.

Miyata K and Dreifus DL, Jpn. J. Appl. Phys., Part 1 **33** (1994) 4526.

Nistor LC, Landuyt JV, Ralchenko VG, Obraztsova ED and Smolin AA., Diamond Relat. Mater. **6** (1997) 159.

Okano K, Koizumi S, Silva SR and Amaratunga GAJ, Nature **298** (1996) 140.

Polyakov VI, Rukovishnikov AI, Rossukanyi NM, Pereverzev VG, Pimenov SM, Carlisle JA, Gruen DM and Loubnin EN, Diamond Relat. Mater. **12** (2003) 1776.

Qin LC, Zhou D, Krauss AR and Gruen DM, Nanostruct. Mater. **10** (1998) 649.

Sze SM, Physics of Semiconductor Devices. John Wiley & Sons, Inc (1981) New York.

Williams OA, Curat S, Gerbi JE, Gruen DM and Jackman RB, The 9th International Workshop on Surface and Bulk Defects in CVD Diamond Films, 16-18 February 2004, Hasselt, Belgium. P66.

Ye HT, Williams OA, Jackman RB, Rudkin R and Atkinson A, phys. stat. sol. **(a) 193** (2002) 462.

Zapol P, Sternberg M, Curtiss LA, Frauenheim T and Gruen DM, Phys. Rev. **B65** (2002) 045403.

Zhou D, Gruen DM, Qin LC, McCauley TG and Krauss AR, J. Appl. Phys. **84** (1998) 1981a.

Zhou D, Gruen DM, Qin LC, McCauley TG and Krauss AR, J. Appl. Phys. **83** (1998) 540b.

Zhou D, Krauss AR, Qin LC, McCauley TG, Gruen DM, Corrigan TD, Chang RPH and Gnaser H, J. Appl. Phys. **82** (1997) 4546.

Chapter 10

Concluding Remarks

In this thesis, the electrical behavior of the diamond grains has been studied separately from grain boundary for the first time within the diamond research community. The impedance measurement yields the real and imaginary parts in the form of a Cole-Cole plot. In this representation, grain interior and grain boundary contributions are identified.

The work presented in this thesis has shown that ac impedance spectroscopy is a powerful technique for investigating the electrical properties of diamond films. Based on the equivalent resistance and capacitance values derived from the diamond impedance data, the conduction processes can be isolated within diamond grain and grain boundary regions. Boron-doped single crystalline diamond film has an activation energy level of 0.37eV for electrical conduction, which is consistent with the values obtained through other techniques. The equivalent capacitance is maintained at the pF level up to 300°C, suggesting that no grain boundaries are being involved, as expected from a single crystal diamond. The single crystalline diamond acts as the simplest example to validate the applications of impedance spectroscopy on diamond materials

Polycrystalline MPECVD diamond films have a better quality than HFCVD diamond on the basis of systematic characterization of their morphological, structural and impedance properties. MPECVD diamond films have a lower growth rate and are more expensive, but with larger area and better repeatability than HFCVD. There is only one semicircular response in the Cole-Cole plot for both MPECVD and HFCVD films. From the simulated capacitance value, it is suggested that grain boundary conduction dominates in

MPECVD diamond films, whilst grain interior conduction dominates in HFCVD samples.

The effect of grain size on the dielectric constant of diamond films was investigated. It is found that increasing Ar gas ratio within the reactants reduces the grain size of diamond films, consequenctly reducing the dielectric constant of diamond. The grain size effect on the dielectric constant could be explained as the change of crystal field caused by surface bond contraction of the nanoscaled particles at grain boundaries.

For nanocrystalline diamond films, a single semicircular response of the electrical conduction is observed at temperatures below 250°C. The secondary semicircular response appears at low frequencies above 250°C. The temperature-dependent resistance measurements show that the activation energy changes from 0.13 eV to 0.67 eV with increasing temperature. Nanocrystalline diamond films containing many fine grain boundaries have a high surface-area-to-volume ratio. With external heating, the grain boundaries undergo the deformation and distortion caused by the thermal expansion or thermal stress, and even oxidation. The total area of grain boundaries, where defects and non-diamond carbon phases are believed to be accumulated, increases enormously. These defective areas are not as thermally stable as diamond grains. Diamond crystals begin to oxidize in air at about 500°C and begin to graphitize under vacuum at around 800°C. Impurities at grain boundaries can be thermally activated at lower temperatures (250°C), as observed. Therefore, oxidation, diffusion, and space charge transportation can easily take place.

Two semicircular responses have been observed for ultrananocrystalline diamond (UNCD), with one dominating at lower temperatures, and the other at higher temperatures. In contrast to nanocrystalline diamond films, UNCD can be made n-type in character through the addition of nitrogen to the growth gas mixture. With increasing temperature, both the grain interior and grain

boundary resistances decrease, hence the overall resistance decreases. The relative resistance ratio between grain interiors and grain boundaries increases with increasing the temperature. This indicates that the conduction is dominated by the grain interiors at lower temperatures and by the grain boundaries at higher temperatures. The activation energy for grain boundaries is always higher than that for grain interior, which might be assigned to the grain boundary induced double Schottky barrier. The UNCD film has an impurity band starting around 0.292eV, but this impurity band is expected to expand with increasing nitrogen content until it begins to merge with the conduction band. This is believed to be responsible for the fact that 20% nitrogen UNCD films being metallic. Based on this model, a critical impurity concentration is predicted to be 0.8×10^{19} cm^{-3}, which is consistent with literature.

This thesis builds up a better understanding of electrical conduction within different types of diamond films and proves impedance spectroscopy is a feasible and useful tool for characterizing the electrical and dielectric properties of diamond films. Further investigations based on the *in-situ* observation of grain boundaries using high-resolution transmission electron microscope with temperature controller could be used as a complementary technique to this work.

The thermal, mechanical, and electrical properties of diamond films offer many opportunities for applications in areas such as electro-emitting cold cathodes, microelectromechanical systems, surface acoustic devices, and electrochemical electrodes. More recently, diamond has opened up a new space towards bio-electronic applications, in which electrodes and electrolytes play a dominant role in the fabrication of devices and sensors. Thus impedance characterization of diamond films for electrochemical applications in electrolyte solutions, electrode interfaces and junctions including space charge polarization should be studied in detail.